MAPPING PHOTOAUTOTROPHIC METABOLISM OF CYANOBACTERIAL AND PLANT SYSTEMS WITH ISOTOPICALLY NONSTATIONARY ^{13}C METABOLIC FLUX ANALYSIS

By

Lara Jeline Jazmin

Dissertation

Submitted to the Faculty of the

Graduate School of Vanderbilt University

in partial fulfillment of the requirements

for the degree of

DOCTOR OF PHILOSOPHY

in

Chemical Engineering

December, 2015

Nashville, TN

Approved:

Jamey D. Young, Ph.D.

Peter T. Cummings, Ph.D.

G. Kane Jennings, Ph.D.

Carl H. Johnson, Ph.D.

To my family, for their constant love and support.

ACKNOWLEDGEMENTS

These past five years at Vanderbilt have been an exciting time in my life and I owe my success to the support of many people. First, I would like to thank my academic advisor, Jamey Young, for his guidance and mentorship in my growth, both scientifically and personally. I am grateful for his patience and encouragement in giving me the confidence to believe in myself as a scientist and entrepreneur. I am excited to continue working with him in the next stage of my professional life as we pursue the formation and growth of MetaMap Bioworks. I would also like thank my undergraduate mentors, Lisa Bullard at NC State and Nick Hutson at the EPA, in encouraging me to continue my scientific pursuits through graduate school. I am also thankful for the guidance of my dissertation committee members: Carl Johnson, Kane Jennings, and Peter Cummings. They have provided invaluable scientific insight and discussion during my graduate tenure.

I am also extremely grateful for the help, support, and contributions of my many collaborators: Yao Xu and Peijun Ma from the Johnson lab, Doug Allen and Fangfang Ma from the Danforth Plant Science Center, and Dick Sayre from Los Alamos National Laboratory. They have taught me about all things cyanobacteria and *Arabidopsis* and have continually challenged me to keep pushing on in my research projects. Many thanks for the support of Ping Ge and the DOE Office of Science Graduate Fellowship Program (DE-AC05-06OR23100), as well as the encouragement from the friends and research peers I made through that program. I would also like to attribute the DOE SC for the

opportunity to attend the Lindau Nobel Laureate Meeting, which was an incredible once in a lifetime experience, as well as the opportunity to attend many other scientific meetings and conferences. My work has also been financially made possible by the following funding sources: GAANN (P200A090323), DOE (DE-SC0008118), and NSF (EF-1105249). I would also like to thank the NSF I-Corps program (IIP-1542695) for giving me the necessary tools and knowledge in reaching a go decision to pursue the commercial application of flux analysis with my advisor.

My time at Vanderbilt would not have been the same without the incredible support and friendship of the members of the Young Lab, both past and present. I am very thankful for Taylor Murphy, Neil Templeton, Rob Egnatchik, and Irina Trenary for helping me with my start in the lab in learning how to use various instruments and discussing all things flux analysis. I truly appreciate the conversations I have had with Lina Aboulmouna, Jessi Campos, Young Mi Whang, Casey Duckwall, Clint Hasenour, and Ian Cheah. Thanks to my cyanobacteria project partner in crime, Adeola Adebiyi, for all her work and effort for that project, as well as Martha Wall for her invaluable MATLAB expertise. And finally, special thanks goes to Ali McAtee and Alex Leamy for always lending an ear and always being there to commiserate or celebrate the ups and downs of lab life with me.

Next, I am incredibly grateful to the many friends that have lived life with me these past five years. I am thankful for the support of all my Raleigh friends that have shown me

what true life-long friendships looks like – many thanks to Caroline and Mat King, SJ Hightower, Tommy and Dani Loveless, and Stephen Colby. I am also especially thankful for the community of friends I have made here in Nashville and have helped make this city truly feel like home as well. My sincerest thanks go to Laura Hover, Amanda Groh, Matt Karolak, Jeremy Chan, Sonia Brady, Holly Zarick, Anne Talley, and many other friends in the ChBE Department and Vanderbilt community, for their friendship and companionship. I am also incredibly grateful for the friends I have at Trinity Church of Nashville who have done life with me, continually pointed me to Christ, and have helped me continue to grow in my faith immensely.

Finally, and most of all, I would like to thank my family. Thanks to my brother Edric, for always having my back and being one of my best friends in life. And thanks to my parents, Jun and Laida, for their constant support and unwavering love – maraming marami, salamat po. They gave me my love for math and science at an early age, as I wanted to follow in their footsteps in becoming an engineer. My family has always believed in me and has urged me to continue pursuing every single goal I have had. And because of all this, I am incredibly thankful.

TABLE OF CONTENTS

Page

LIST OF TABLES

Page

LIST OF FIGURES

Page

LIST OF ABBREVIATIONS

2PG	2-phosphoglycolate
3PGA	3-phosphoglycerate
T_3PGA	3PGA transporter
ACA	acetyl-CoA
ACO	aconitase
ADPG	ADP-glucose
AGP	ADP-glucose phosphorylase
ALA	Alanine
ALT	alanine Transaminase
ALD	aldolase
AKG	α-ketoglutarate
ASN	asparagine
AS	asparagine synthase
ASP	aspartate
ASPT	aspartate Transaminase
CBB	Calvin-Benson-Bassham cycle
CO2	carbon dioxide
Vc	carboyxlation flux
CIT	citrate
CS	citrate synthase
E4P	erythrose-4-phosphate
FBP	fructose-1,6-bisphosphatase
F6P	fructose-6-phosphate
FBA	fructose-bisphosphate aldolase
FUM	fumarate
GC-MS	gas chromatography-mass spectrometry
G1P	glucose-1-phosphate
G6P	glucose-6-phosphate
G6PDH	glucose-6-phosphate dehydrogenase
GLN	glutamine
GS	glutamine synthetase
GAPDH	glyceraldehyde-3-phosphate dehydrogenase
GA	glycerate
GK	glycerate kinase
GLY	glycine
GDC	glycine decarboxylase
ICI	isocitrate
IDH	isocitrate dehydrogenase
INST-MFA	isotopically nonstationary metabolic flux analysis

LC-MS/MS	liquid chromatograph-tandem mass spectrometry
MAL	malate
MDH	malate dehydrogenase
ME	malic enzyme
MRM	multiple reaction monitoring
netA	net CO_2 assimilation
OAA	oxaloacetate
OPPP	Oxidative Pentose Phosphate Pathway
Vo	oxygenation flux
PEP	phosphoenolpyruvate
PPC	phosphoenolypyruvate carboxylase
PFP	phosphofructokinase pyrophosphate
PGM	phosphoglucomutase
PGI	phosphoglucose isomerase
PGAM.c	phosphoglycerate mutase
PGP	phosphoglycolate phosphatase
PPE	phosphopentose epimerase
PPI	phosphopentose isomerase
PRK	phosphoribulokinase
Vpr	photorespiratory CO_2 release
PRO	proline
PCR	pyrroline-5-carboxylate reductase
PYR	pyruvate
PDH	pyruvate dehydrogenase
PK.c	pyruvate kinase
R5P	ribose-5-phosphate
RUBP	ribulose-1,5-bisophosphate
RUBISCO_O2	ribulose-1,5-bisphosphate (carboxylase) oxygenase
RUBISCO_CO2	ribulose-1,5-bisphosphate carboxylase (oxygenase)
RU5P	ribulose-5-phosphate
S7P	sedoeheptulose-7-phosphate
SBP	sedoheptulose-1,7-bisophosphate
SBPase	sedoheptulose-1,7-bisphosphatase
SER	serine
SGA1	serine:glyoxylate aminotransferase
SS	starch synthase
SUC	succinate
SCA	succinyl-CoA
S6P	sucrose-6-phosphate
SPS	sucrose-phosphate synthase
SSR	sum-of-squared residuals
THR	threonine
TS	threonine synthase

T_TP	TP transporter
TK1	transketolase
EC2	transketolase-bound-2-carbon-fragment
TP	triose phosphate
UDPG	UDP-glucose
GPU	UDP-glucose pyrophosphorylase
X5P	xyulose-5-phosphate

1. INTRODUCTION

1.1 OVERVIEW

The overarching theme of this dissertation is the application of isotopically nonstationary ^{13}C metabolic flux analysis (INST-MFA) to photosynthetic organisms: cyanobacteria and plants. The food, energy, and environmental problems we are currently facing are driving the development of strategies to enhance the efficiency of photosynthetic systems. Cyanobacteria in particular have recently garnered attention as a renewable source for production of fuels and chemicals directly from CO_2 [1]. Efforts to improve plant productivity are also continually increasing, as this leads to more food for a growing world population and can serve as a sustainable source of renewable feedstocks to supplant petroleum. Additionally, there is growing interest in the study of plants as host factories for the production of compounds with significant commercial value, such as pharmaceuticals, nutraceuticals, dyes, fragrances, flavors, and pesticides [2]. Therefore, there is a critical need to assess metabolic capabilities of these photosynthetic systems so that strains optimized for the production of fuels, chemicals, and/or biomass can be developed.

Metabolic flux analysis (MFA) is a well-established method used to quantify intracellular metabolic fluxes. These metabolic fluxes constitute the physiological phenotype of biological systems [3]. As such, the *in vivo* measurement of intracellular fluxes provides invaluable information for understanding cellular regulation in response to genetic

interventions or changed environmental conditions [4]. Metabolic engineers have employed flux analysis to identify knockout, overexpression, and/or media optimization targets, thereby increasing product formation and enhancing metabolic efficiency of host cell factories. However, only INST-MFA can be applied to estimate carbon fluxes in autotrophic systems, which consume only single-carbon substrates (e.g., CO_2) [5,6]. This task is impossible with stationary ^{13}C MFA due to the fact that all carbon atoms in the system are derived from the same source and therefore will become uniformly labeled at steady state regardless of the flux distribution. As a result, prior ^{13}C MFA studies of plants and cyanobacteria have been limited to heterotrophic or mixotrophic growth conditions, typically with sugar as the major carbon source [7,8]. Currently, only a few comprehensive INST-MFA experiments have been reported, and the majority of these studies have been applied to hosts other than cyanobacteria and plants. This dissertation discusses the results of research advancing the application of INST-MFA to photoautotrophic cyanobacterial and plant systems in the following chapters:

- **Chapter 2** provides an in-depth background into the mathematical principles behind MFA, and more specifically INST-MFA. Also reviewed are recent studies involving the application of flux analysis to photoautotrophs.

- **Chapter 3** applies INST-MFA to two cyanobacterial strains of *Synechococcus elongatus* PC 7942: a wild-type strain and a strain engineered to produce isobutyraldehyde. The resulting flux maps point to a bottleneck at the pyruvate node and a potential pyruvate kinase (PK) bypass pathway, leading to actionable

results in the form of targets for enzyme overexpression. The parental isobutyraldehyde-producing strain was used to generate single-, double-, and triple- overexpression strains involving PK or genes in the PK bypass pathway. Efforts to increase isobutyraldehyde productivity through rationally selected enzyme overexpression targets were successful, making this study a useful demonstration of how INST-MFA can be used to close the 'design-build-test-learn' metabolic engineering cycle.

- **Chapter 4** describes further application of INST-MFA to a more complex photoautotrophic metabolic network in the leaves of the C3 plant *Arabidopsis thaliana*. This was the first application of INST-MFA to a terrestrial plant system *in planta*. Plant leaf metabolism was quantified under two different acclimated photoautotrophic conditions of low light (200 μmol m^{-2} s^{-1}) and high light (500 μmol m^{-2} s^{-1}). The resulting comprehensive flux maps of central carbon metabolism quantitatively describe alterations in carbon partitioning by acclimation and light conditions. This study paves the way for future isotope labeling experiments and flux analysis in plant leaves to examine environmental and genetic perturbations on photosynthetic carbon fluxes.

- **Chapter 5** extends the application of the INST-MFA approach to plant leaves described in Chapter 4 and examines the differences in three transgenic lines of *Arabidopsis thaliana* engineered with a bacterial carbonic anhydrase

overexpression construct to enhance photosynthetic carbon fixation. As a control, we also quantified fluxes in wild-type *Arabidopsis thaliana* acclimated from low to high CO_2 conditions (330 ppm to 800 ppm). The flux analysis revealed that plants grown under high CO_2 conditions showed an overall increase in carboxylation, with a decrease in photorespiration as expected. However, although the transgenic lines also showed increases in carboxylation, there was an unexpected increase in photorespiration. Additionally, simulation studies performed as a result of this unexpected increase in photorespiration led to further scrutiny of the measured mass fragments used for INST-MFA. These simulation studies showed that ratios of individual mass isotopomers of ribulose-1,5-bisphosphate (RUBP) could potentially be used in future studies as a labeling signature to qualitatively describe low and high photorespiratory fluxes prior to applying comprehensive flux analysis. Overall, this study shows that it is crucial to quantify global impacts of genetic perturbations on metabolic pathways *in planta* to guide further rounds of plant metabolic engineering.

- **Chapter 6** concludes the dissertation with a summary of the main findings and presents ideas for future work.

2. BACKGROUND AND LITERATURE REVIEW

Methods in Molecular Biology (2013). 985:367–390.

Methods in Molecular Biology (2014). 1090:181-210.

Current Opinion in Biotechnology (2015). 38:50-56.

2.1 PHOTOAUTOTROPHIC METABOLISM

Photoautotrophic metabolism is the principal process by which photosynthetic organisms, such as algae, cyanobacteria, and plants, use solar energy to incorporate inorganic carbon dioxide into complex organic molecules. These complex molecules represent the main source of all food on earth, as well as raw materials for bio-based production of commodity and specialty chemicals, like fuels and pharmaceuticals, respectively. There have been six different pathways of carbon fixation identified in nature, and the Calvin-Benson-Bassham (CBB) cycle accounts for more than 99% of the global primary biomass production [9,10]. However, less than 1% of available solar energy flux is typically converted into chemical energy by photosynthetic processes. Therefore, developing strategies to enhance the efficiency of photosynthetic carbon fixation is a key step toward solving food, energy and environmental challenges of the future [10].

To meet the demands of biotechnology, metabolic engineering strategies have been employed to develop photosynthetic host organisms that produce valuable products more

efficiently. Metabolic engineering involves the introduction or modification of specific biochemical reactions with the use of recombinant DNA technology [11]. Typically, the manipulations made to the host strains impact the metabolic flux distributions in the system. In order to gain a better understanding of the impact of these manipulations, systems-level metabolic flux characterization approaches have been developed. These include *in silico* approaches, such as kinetic and stoichiometric modeling, which can simulate metabolic network behavior and predict genes that can be engineered to improve host cell performance. However, to fully quantify intracellular metabolic fluxes, experimental approaches such as ^{13}C metabolic flux analysis (MFA), isotopically nonstationary ^{13}C MFA (INST-MFA), and kinetic flux profiling (KFP) [12] have been used with isotope labeling experiments (ILEs). These experimental approaches have all been applied to quantify photoautotrophic metabolism and are discussed in further detail in Section 2.4. Much of the work in this dissertation is spent applying MFA, specifically INST-MFA, to photoautotrophic systems so that we can gain fundamental insights into how these systems respond to genetic or environmental perturbations, which can be used to guide further rounds of metabolic engineering.

2.2 METABOLIC FLUX ANALYSIS

^{13}C metabolic flux analysis (MFA) is a powerful approach for quantifying central carbon metabolism based upon a combination of extracellular flux measurements and intracellular isotope labeling measurements. The ability to quantitatively map intracellular carbon fluxes using isotope labeling experiments (ILEs) and MFA is critical for identifying pathway bottlenecks and elucidating network regulation in biological

systems, especially those that have been engineered to alter their native metabolic capacities [13,14].

MFA experiments involve feeding isotopically labeled substrates to cells, tissues, or whole organisms and subsequently measuring patterns of isotope redistribution in metabolic products. Typically, MFA relies on the assumption of both metabolic and isotopic steady state. Achieving this situation experimentally involves (1) equilibrating the system in a stable metabolic state, (2) introducing an isotopically labeled substrate without perturbing the metabolic steady state, (3) allowing the system to establish a new isotopic steady state that is dictated by the underlying metabolic fluxes, and (4) measuring isotopic labeling in the fully equilibrated system as shown in Figure 2.1.

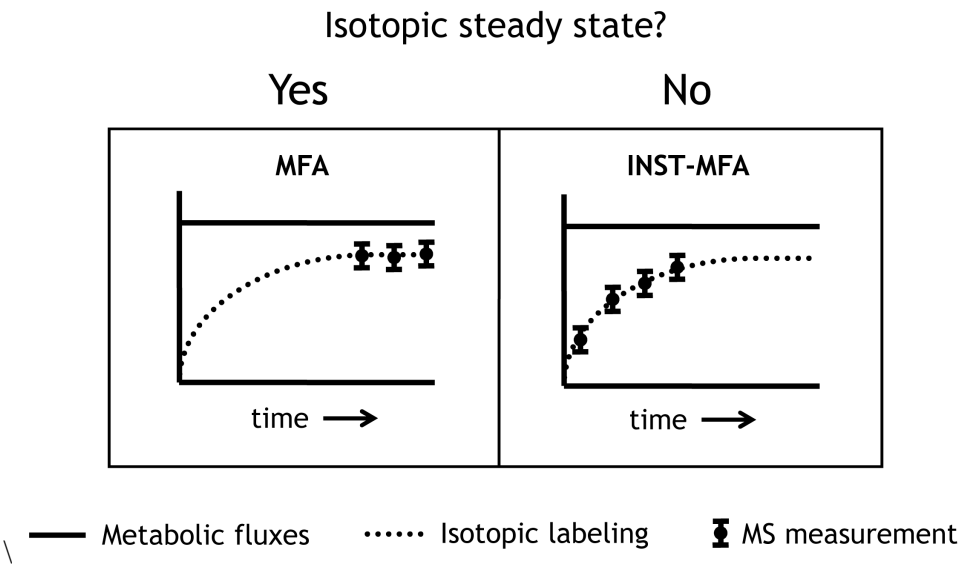

Figure 2.1. Comparison between steady-state and nonstationary MFA methodologies.

The relative speed of metabolic and isotopic dynamics will influence the type of MFA study performed. The left panel shows the conventional MFA approach under both metabolic and isotopic steady state. The right panel shows INST-MFA at metabolic steady state, but not isotopic steady state.

The patterns of isotope incorporation in intracellular and extracellular metabolites are measured using either mass spectrometry (MS) or nuclear magnetic resonance spectrometry (NMR). Although NMR is useful because it provides positional labeling information, these instruments are not as widely available as MS instruments, have a reduced sensitivity, and longer analysis time [15]. MS, on the other hand, provides a highly sensitive and accurate method for quantifying isotope incorporation, and much of the work with MFA in the past decade has shifted to MS techniques. The pathways of interest will dictate the measured metabolites and the types of MS analysis to be performed. Generally, amino acids, organic acids, fatty acids, and sugars can be analyzed

using GC-MS following chemical derivatization. Sugar phosphates and acyl-CoA molecules, on the other hand, are typically analyzed via LC-MS or LC-MS/MS, to avoid thermal degradation of these nonvolatile analytes. MS data provides mass isotopomer distributions (MIDs) of fragment ions associated with target analytes of interest, which can be used with extracellular flux measurements to quantify intracellular metabolism.

2.3 ISOTOPICALLY NONSTATIONARY MFA (INST-MFA)

Although ^{13}C is the preferred isotope tracer for quantifying central carbon metabolism in heterotrophic systems, autotrophic organisms assimilate carbon solely from CO_2 and therefore produce a uniform steady-state ^{13}C-labeling pattern that is insensitive to fluxes (Figure 2.2). This makes conventional steady-state ^{13}C-MFA ineffective for quantifying autotrophic metabolism [5,16]. However, transient measurements of isotope incorporation following a step change from natural CO_2 to $^{13}CO_2$ can be used to determine fluxes by application of INST-MFA. Furthermore, INST-MFA has the ability to quantify metabolite pool sizes based solely on their labeling dynamics [17,18], thus providing a potential framework for integrating metabolomic datasets with MFA [19]. Despite its advantages, however, the increased complexity of INST-MFA introduces additional difficulties at both the computational and experimental levels that must be addressed. First, the solution of large-scale ordinary differential equation (ODE) models poses a substantial challenge to efficiently simulate transient isotope labeling experiments. The application of elementary metabolite unit (EMU) decomposition to INST-MFA has greatly reduced this computational burden and has enabled determination of fluxes and accurate confidence intervals in biologically relevant networks [20,21].

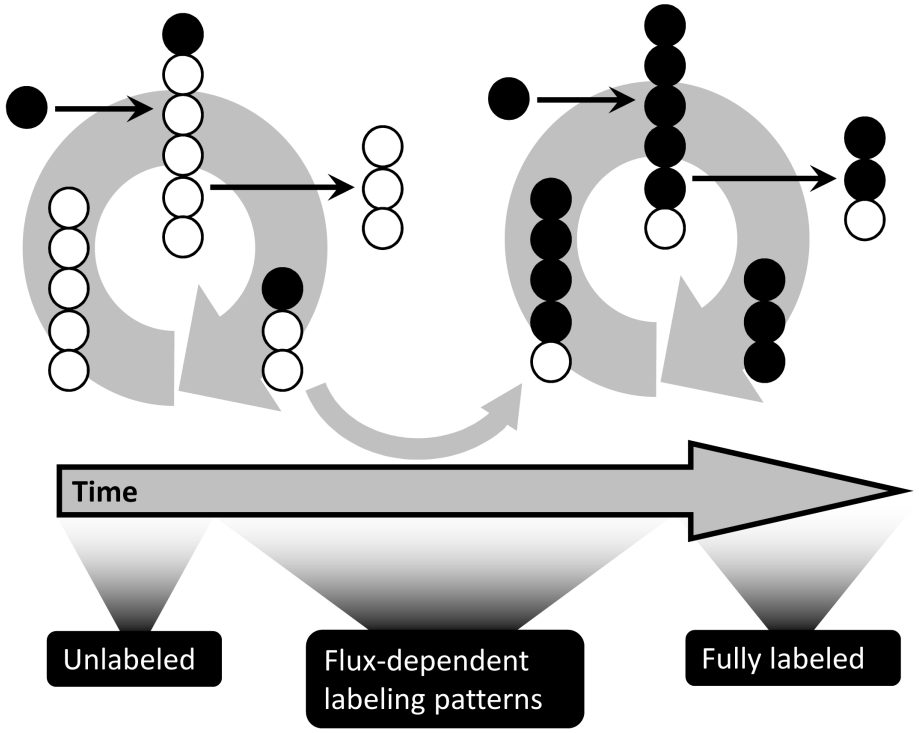

Figure 2.2. Example of carbon labeling in an autotrophic system.

Following the introduction of $^{13}CO_2$ to the Calvin cycle, intracellular metabolites become gradually labeled over time. Once steady-state labeling is achieved, all metabolites are uniformly ^{13}C-labeled irrespective of fluxes and intracellular pool sizes. Labeling patterns observed during the isotopically transient period, however, can be computationally analyzed to determine fluxes.

Second, the requirement for isotopically nonstationary measurements adds further complexity to experimental design, including selection of sampling time points and metabolite concentration measurements. Finally, rapid sampling and metabolite quenching must be applied in order to obtain meaningful isotopomer data from rapidly labeled intracellular metabolites. The field of metabolomics has witnessed considerable

progress in this area, and some of these measurement techniques have already been successfully adapted for isotopomer studies in autotrophs [22].

A flow chart of a typical INST-MFA process is shown in Figure 2.3 [23]. INST-MFA is concerned with solving an "inverse problem" where fluxes and pool sizes are estimated from measured labeling patterns and extracellular rates through the means of an iterative least-squares fitting procedure. At each iteration, a "forward problem" is solved where an isotopomer model is used to simulate labeling measurements for a given metabolic network and a given set of parameter estimates. The discrepancy between the simulated and measured labeling patterns is then assessed, and the parameter estimates are updated to achieve an improving fit. Once convergence to the best-fit solution is obtained, the procedure terminates and the optimal flux and pool size estimates are returned. Our lab utilizes the INCA (Isotopomer Network Compartmental Analysis) software package, which runs through the MATLAB computing environment, to automate the computational workflow of INST-MFA [24].

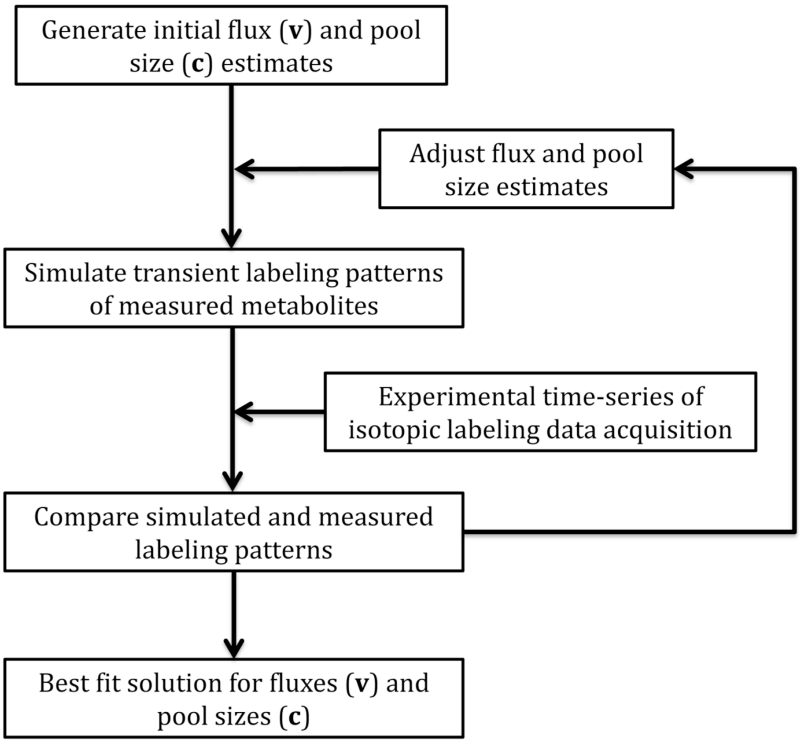

Figure 2.3. Flowchart showing the overall schematic of 13C INST-MFA.

Following the labeling experiment and MS analysis of the measured metabolites, computational analysis of the dynamic changes in isotope labeling patterns can be used to estimate metabolic pathway fluxes and pool sizes. This involves solving an inverse problem whereby the vectors of flux (v) and pool size (c) parameters are iteratively adjusted until the mismatch between simulated and experimentally measured data sets is minimized.

2.3.1 BUILDING ISOTOPOMER MODELS FOR INST-MFA

In order to perform INST-MFA, it is necessary to reconstruct a metabolic network from biochemical literature and the annotated genome of the organism of interest. This network must prescribe both (i) the stoichiometry of all enzymatic reactions under consideration and (ii) atom transitions for each reaction. Reactions must also be classified

as either reversible or irreversible. When constructing a model, it is important to strive for parsimony in describing the available experimental measurements. The model must be sophisticated enough to reconcile all available experimental measurements while simultaneously avoiding the unnecessary complexity and redundancy that leads to overfitting of parameters. Fortunately, there are statistical tests to assess goodness-of-fit and to detect loss of precision due to overfitting (presented in Section 2.3.2). Overly sophisticated models can be reduced by (i) combining linear pathways into a single reaction, (ii) combining isoenzymes or parallel pathways that catalyze identical conversions, and (iii) omitting irrelevant pathways based on biological knowledge, such as repression of pathways under certain conditions [25]. Additionally, if the cells are growing at a significant rate, all fluxes toward biomass production can be lumped into a single biosynthetic reaction that summarizes the withdrawal of all necessary growth precursors. Cofactors that contribute to energy balancing (e.g., ATP) or redox balancing (e.g., NADH or NADPH) are usually omitted from the model to ensure that these difficult-to-quantify balances do not unduly bias the resulting flux estimates [25].

Construction of a stoichiometric model can be further complicated by: (i) compartmentalization of metabolites, (ii) reaction reversibility, and (iii) tracer dilution from unlabeled sources. First, as a result of subcellular compartmentalization in eukaryotes, the same biochemical reactions can occur simultaneously in different organelles, giving rise to multiple distinct metabolic pools that must be treated as separate nodes in the isotopomer model. Transport of metabolites between different compartments also needs to be defined in the model (e.g., exchange of pyruvate between the cytosol and

mitochondria). Because each metabolite measurement obtained by MS analysis represents an aggregation of these different metabolic pools, pseudo-reactions can be introduced into the model to represent the contribution from each compartment. However, this also introduces additional parameters into the model that must be determined from the isotopomer measurements. Second, reaction reversibility is another crucial consideration, since exchange fluxes (defined as the minimum of the forward and reverse reaction rates) affect metabolite labeling patterns in addition to net fluxes (defined as the difference between forward and reverse reaction rates). While all enzymes are reversible to some extent, many can be classified as practically unidirectional as a result of thermodynamic and kinetic considerations (e.g., pyruvate kinase in glycolysis). Third, enrichment of the tracer can also be diluted by unlabeled sources, such as CO_2 present in air, unlabeled carbon sources in complex culture media, or even breakdown of macromolecular biomass components. The inclusion of these unlabeled sources in the model can be critical to obtaining a statistically acceptable description of actual experimental data sets.

2.3.2 MATHEMATICAL PRINCIPLES OF INST-MFA

When constructing the stoichiometric model, fluxes are required to satisfy the constraint

$$S \cdot v = 0 \tag{2.1}$$

where S is the stoichiometric matrix and v is the flux vector. In Equation 2.1, the stoichiometric matrix S is a $k \times j$ matrix, with k metabolites and j fluxes. Reversible

reactions are modeled as separate forward and backward fluxes, so that all fluxes are non-negative. Section 2.6 shows a simple network model example, which illustrates the process of setting up the stoichiometric matrix as well as subsequent steps discussed below.

Once the stoichiometric matrix *S* is constructed, the free fluxes of the network, as well as the null space matrix need to be identified. From a computational standpoint, it is more convenient to work with "free" fluxes, rather than the "true" network fluxes [26,27]. Free fluxes can be obtained from the general solution to Equation (2.1

$$v = N \cdot u \tag{2.2}$$

where *N* is the null space matrix of *S* and *u* is the vector of free fluxes. There are many methods to calculate a valid null space matrix, and generally there is not a unique null space matrix for any given stoichiometric matrix [28]. The size of the null space matrix and the number of independent flux variables are determined by the rank of the stoichiometric matrix. With $r = \text{rank}(S) \leq k$, the null space matrix is a $j \times j - r$ matrix and the number of free fluxes is $j - r$.

In INST-MFA, the isotopomer balances are described by a system of ordinary differential equations, which is significantly more difficult to solve than the algebraic systems that describe steady-state labeling. Due to this additional difficulty, algorithms for solving the forward problem of INST-MFA need to be carefully designed so that computational expense does not become prohibitive. The most efficient approach involves first

decomposing the isotopomer network into EMUs [20,21]. By only solving for the isotopomer distributions of EMUs that contribute to the available measurements, this approach minimizes the number of ODEs that need to be integrated and thereby enables the forward problem to be solved thousands of times faster than previous methods. This, in turn, increases the efficiency of solving the inverse problem of INST-MFA because each iteration of the parameter estimation procedure can be completed in minimal time.

An EMU is defined as a distinct subset of a metabolite's atoms and can exist in a variety of mass states depending on its isotopic composition. In its lowest mass state, an EMU is referred to as M0, while an EMU that contains one additional atomic mass unit (e.g., as a result of a ^{13}C atom in place of ^{12}C atom) is referred to as M1, with higher mass states described accordingly. An MID is a vector that contains the fractional abundance of each mass state of an EMU. To solve the forward problem of simulating metabolite labeling in INST-MFA, the isotopomer network is first systematically searched to enumerate all EMUs that contribute to measurable MS fragment ions [21]. The main advantage of the EMU decomposition is that metabolites are never broken into smaller pieces than is strictly required to describe the labeling state of the measured metabolites (Section 2.6).

The EMU reactions identified from network decomposition form the new basis for generating system equations. In INST-MFA, these EMUs are grouped into mutually dependent blocks using a Dulmage-Mendelsohn decomposition [29,30]. Therefore, by definition, all EMUs within a particular block have the same number of atoms and must

be solved simultaneously and not sequentially. The decoupled blocks can be arranged into a cascaded system of ODEs with the following form

$$\mathbf{C}_n \cdot \frac{\mathrm{d}\mathbf{X}_n}{\mathrm{d}t} = \mathbf{A}_n \cdot \mathbf{X}_n + \mathbf{B}_n \cdot \mathbf{Y}_n \tag{2.3}$$

Level *n* of the cascade represents the network of EMUs within the *n*th block. The rows of the state matrix $\mathbf{X}_n$ correspond to MIDs of EMUs within the *n*th block. The input matrix $\mathbf{Y}_n$ is analogous but with rows that are MIDs of EMUs that are previously calculated inputs to the *n*th block (or MIDs of source EMUs that are unbalanced). The concentration matrix $\mathbf{C}_n$ is a diagonal matrix whose elements are pool sizes corresponding to EMUs represented in $\mathbf{X}_n$. The system matrices $\mathbf{A}_n$ and $\mathbf{B}_n$ describe the network as follows

$$\mathbf{A}_n(i,j) = \begin{cases} -\text{sum of fluxes consuming } i\text{th EMU in } \mathbf{X}_n & i = j \\ \text{flux to } i\text{th EMU in } \mathbf{X}_n \text{ from } j\text{th EMU in } \mathbf{X}_n & i \neq j \end{cases} \tag{2.4}$$

$$\mathbf{B}_n(i,j) = \{\text{flux to } i\text{th EMU in } \mathbf{X}_n \text{ from } j\text{th EMU in } \mathbf{Y}_n \tag{2.5}$$

The system matrices $\mathbf{A}_n$ and $\mathbf{B}_n$ can be evaluated directly once the "true" flux vector (*v*) has been determined from the free fluxes (*u*) and the null space matrix (*N*).

Solving the forward problem enables calculation of isotopomer distributions for each metabolite of interest, based on the initial flux and pool size estimates. The simulated MIDs can be plotted versus time and compared to the measured data. Figure 2.4 shows an example of the labeling dynamics of several metabolites in an autotrophic system using ^{13}C-labeled bicarbonate as the tracer. The relative abundances of unlabeled mass isotopomers (M0) dropped at the start of the labeling period and were replaced by M1, M2, and higher mass isotopomers following the introduction of tracer. Additionally, it is

also informative to plot the average enrichments of various MS fragment ions as shown in Figure 2.5. The average ^{13}C enrichment is calculated using the following expression:

$$\frac{1}{N}\sum_{i=1}^{N} Mi \times i \tag{2.6}$$

where N is the number of carbon atoms in the metabolite and Mi is the fractional abundance of the ith mass isotopomer.

Estimation of both the unknown fluxes and pool sizes using INST-MFA is accomplished by finding a best-fit solution to the inverse problem. Efficient solution of this problem typically relies on optimization algorithms that choose the search direction based on the gradient of the least-squares objective function (Equation (2.8)) with respect to all adjustable parameters. The most accurate and least expensive way to obtain the required gradient information is to integrate a system of sensitivity equations whose solution describes how the calculated MIDs vary in response to changes in the model parameters. Implicit differentiation of Equation (2.3) yields the following sensitivity equation:

$$\frac{\mathrm{d}}{\mathrm{d}t}\frac{\partial \mathbf{X}_n}{\partial \mathbf{p}} = \mathbf{C}_n^{-1} \cdot \mathbf{A}_n \cdot \frac{\partial \mathbf{X}_n}{\partial \mathbf{p}} + \frac{\partial (\mathbf{C}_n^{-1} \cdot \mathbf{A}_n)}{\partial \mathbf{p}} \cdot \mathbf{X}_n + \mathbf{C}_n^{-1} \cdot \mathbf{B}_n \cdot \frac{\partial \mathbf{Y}_n}{\partial \mathbf{p}} + \frac{\partial (\mathbf{C}_n^{-1} \cdot \mathbf{B}_n)}{\partial \mathbf{p}} \cdot \mathbf{Y}_n \tag{2.7}$$

where $\mathbf{p}$ is the vector of adjustable flux and pool size parameters. This system of equations can be solved in tandem with those of Equation (2.3), and the time-dependent sensitivities can be used to evaluate the objective function gradient during each iteration of the INST-MFA inverse problem. Furthermore, if approximate values of the parameters are available prior to performing the labeling experiment, calculation of measurement

sensitivities can provide useful information pertaining to parameter identifiability and experimental design.

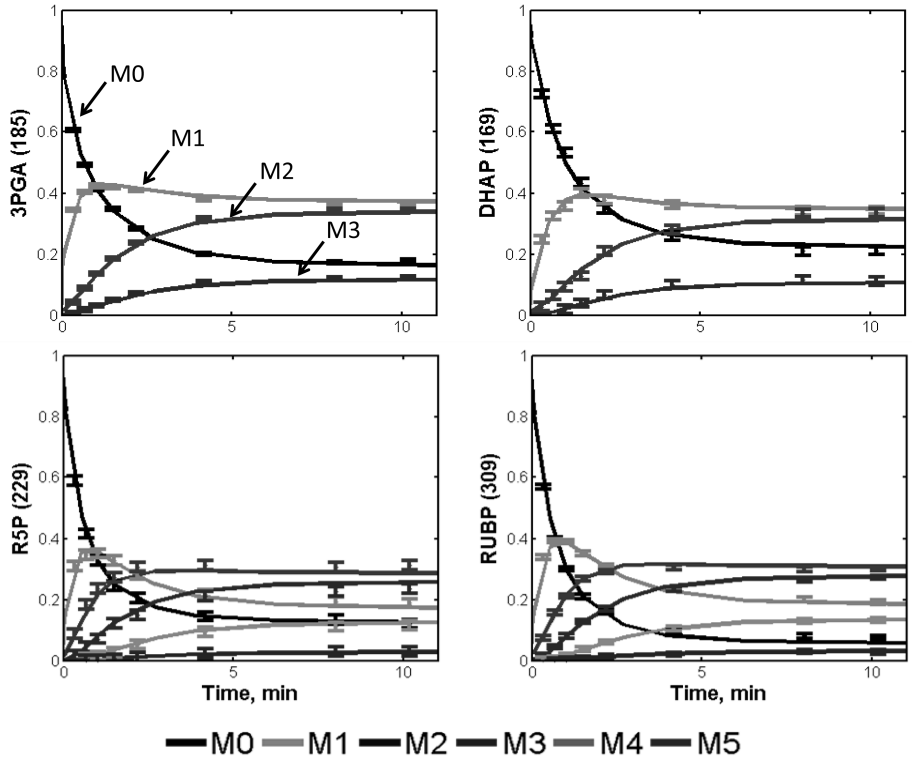

Figure 2.4. Labeling trajectories of central metabolic intermediates.

Experimentally measured labeling trajectories of central metabolic intermediates (data points) and INST-MFA model fits (solid lines) from an autotrophic INST-MFA study. The error bars represent standard measurement errors. Ions shown are for 3-phosphoglycerate (3PGA), dihydroxyacetone phosphate (DHAP), ribose-5-phosphate (R5P), and ribulose-1,5-bisphosphate (RUBP). Nominal masses of M0 mass isotopomers are shown in parentheses. Adapted from Young et al. [6].

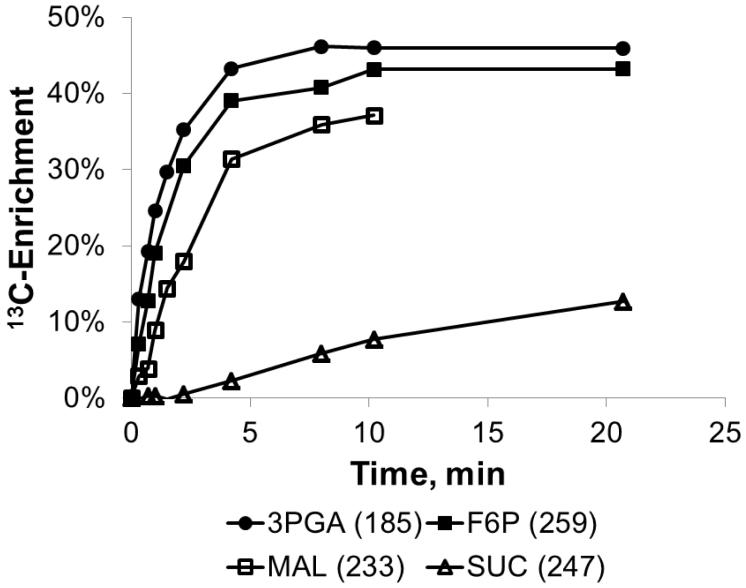

Figure 2.5. Average 13C enrichments of selected ion fragments from an autotrophic INST-MFA study.

The labeling trajectory is shown for 3-phosphoglycerate (3PGA), fructose-6-phosphate (F6P), malate (MAL), and succinate (SUC) over the course of 10 minutes. Adapted from Young et al. [6].

While solving the forward problem is an important step in the determination of fluxes using INST-MFA, it can also inform the experimental design. The precision with which a particular flux or pool size can be estimated, if at all, is solely determined by the sensitivity of the available measurements to the flux in question, which is a function of (i) the isotopic tracer applied, (ii) the structure of the metabolic network, (iii) the intracellular flux distribution, (iv) the timing of the measurements and (v) the metabolites that are measured. Since (ii) and (iii) are not under the control of the experimenters, the key elements of experimental design entail choosing appropriate combinations of (i), (iv) and (v) to identify the fluxes of interest. For the most part, the prevailing philosophy has

been to measure as many metabolites as possible that are relevant to the pathways of interest. Therefore, the focus of experimental design has been on choosing a labeling and sampling strategy that will maximize the precision of flux estimates based on the available isotopic measurements. There is a wide literature on optimal design of ^{13}C labeling experiments, and the extension of these concepts to INST-MFA experiments has been presented by Wiechert and colleagues [17,31].

After the EMU balances have been set up, the labeling distributions can be simulated. Fluxes and pool sizes are estimated by minimizing the difference between measured and simulated data according to the following equation [17,21].

$$\min_{\mathbf{u},\mathbf{c}} \phi = [m(u,c,t) - \hat{m}(t)]^T \cdot \sum_{m}^{-1} \cdot [m(u,c,t) - \hat{m}(t)] \quad \text{s.t.} \; N \cdot u \geq 0, \mathrm{c} \geq 0 \tag{2.8}$$

where ϕ is the objective function to be minimized, u is a vector of free fluxes, $\mathbf{c}$ is a vector of metabolite concentrations, t is time, $m(u,c,t)$ is a vector of simulated measurements, $\hat{m}(t)$ is a vector of observed measurements, $\Sigma_{\mathbf{m}}$ is the measurement covariance matrix, and N is the null space of the stoichiometric matrix. A reduced gradient method can be implemented to handle the linear constraints of this problem within a Levenberg-Marquardt nonlinear least-squares solver [32,33].

Once an optimal solution is found, the overall fit of the flux estimation needs to be assessed. Testing the goodness-of-fit will determine whether the optimal solution is

statistically acceptable based on the minimized sum of squared residuals (SSR). At convergence, the minimized variance-weighted SSR is a stochastic variable drawn from a chi-square distribution with *n-p* degrees of freedom (DOF), where *n* is the number of independent measurements and *p* is the number of estimated parameters. The SSR that is calculated should therefore be in the interval $[\chi^2_{\alpha/2}\ \chi^2_{1-\alpha/2}]$, where α is a chosen threshold value corresponding to the desired confidence level (e.g., 0.05 for 95% confidence or 0.01 for 99% confidence). The model fit is accepted when the SSR falls within the limits of the expected chi-square range [34]. Additionally, the distribution of residuals should be assessed for normality. The standard deviation-weighted residuals should be normally distributed with a mean of zero and standard deviation of one. One approach that can be used to evaluate the hypothesis that the residuals are normally distributed is the Lilliefors test [35]. Various plots can also be constructed to assess normality of the residuals.

In addition to checking the overall distribution of the residuals, it is often informative to plot the simulated and measured MIDs of each MS fragment ion to assess the goodness-of-fit of each measurement. Furthermore, one should check the residuals between any measured extracellular fluxes and the estimates derived from INST-MFA. This provides a visual assessment of which measurements are responsible for the lack of fit. If the flux estimation provides a poor fit, further investigation needs to be performed to identify the source of disagreement between experimental measurements and the isotopomer model. There are three possible causes for this poor fit that should be evaluated: (1) there are errors associated with the measurements, (2) there is an inappropriate weighting of the residuals, or (3) there is an error or omission in the metabolic reaction network. One

should proceed by process of elimination to determine which of these is the root cause of a poor fit and then take corrective steps.

Afterwards, it is important to identify measurements that contribute significantly to the precision of estimated fluxes. The fractional contribution of each measurement to the local variance of each flux can be calculated as described in Antoniewicz *et. al* [34]. The higher the contribution value, the more important the measurement is for determining a particular flux. Fluxes that depend on only one measurement are very sensitive to errors in that one measurement. It is therefore desirable that more than one measurement significantly contributes to the estimation of each flux.

Once an optimal solution has been obtained, nonlinear confidence intervals on the fitted parameters should be computed using robust, global methods instead of relying solely upon local standard errors. The local standard errors can be easily obtained from the parameter covariance matrix at the optimal solution; however, they do not accurately reflect changing sensitivities at points removed from the optimal solution. Furthermore, the calculation of the covariance matrix becomes ill-conditioned when the Hessian of ϕ with respect to the fitted parameters is close to singular. Parameter continuation can be performed to calculate accurate upper and lower bounds on the 95% confidence interval for each flux or pool size parameter [34]. This determines the sensitivity of the minimized SSR to varying a single parameter away from its optimal value, while allowing the remaining parameters to adjust in order to minimize $\Delta\phi$. Large confidence

intervals indicate that the flux cannot be estimated precisely. On the other hand, small confidence intervals indicate that the flux is well determined. Monte Carlo simulation can also be used to calculate the 95% confidence intervals. This method is typically more expensive than the parameter continuation approach, but is expected to yield similar results.

Once an acceptable fit to the experimental measurements has been achieved and confidence intervals have been computed for all parameters, the results are best summarized visually in the form of a flux map. Several software tools have been recently developed for flux visualization in the context of metabolic networks, such as FluxMap [36], FluxViz [37], fa-BINA [38], Omix [39], BioCyc Omics Viewer [40], Reactome Skypainter [41], Pathway Projector [42], MetaFluxNet [43], OptFlux [44], and Escher [45].

Overall, INST-MFA holds great potential for future applications. INST-MFA experiments are already performed in a fraction of the time required for stationary MFA. If downstream sample processing and data analysis can be streamlined and automated, INST-MFA could soon become the basis for high-throughput MFA approaches [46,47]. It is also likely that INST-MFA will become the preferred approach for studies of plants, algae, and animal cell cultures, where labeling is slow and lack of long-term phenotypic stability can restrict the maximum duration of isotope tracer experiments.

2.4 APPLICATION OF FLUX ANALYSIS TO ENABLE RATIONAL ENGINEERING IN PHOTOAUTOTROPHS

Mammalian, plant, yeast, and bacterial cells are currently being used as industrial hosts for the production of commodity chemicals, specialty chemicals, small-molecule drugs, therapeutic proteins, and other biomolecules of commercial interest [48]. Of particular interest to this dissertation is the use of photoautotrophs, specifically cyanobacteria and plants, as industrial cell factories. Because these processes rely on living cells as biocatalysts, they are often hindered by toxic byproduct formation, low product yield, and slow production rates. Genome-scale modeling, cell-wide 'omics' platforms, and high-throughput screening approaches have been developed to overcome these challenges by identifying genes that can be engineered to improve host cell performance. However, isotope labeling experiments (ILEs) and metabolic flux analysis (MFA), as described in the previous sections, have received limited attention in the biotech and biopharma industries to date, despite the fact that these approaches can provide direct readouts on *in vivo* metabolic pathway activities. This may be partly due to the fact that many companies lack the combined experimental and computational expertise needed to effectively analyze ILEs, but perhaps even more important is the perception that these studies are intrinsically difficult and there have not been enough success stories to justify the requisite effort [49]. The purpose of this section is to present examples where ILEs and MFA have been successfully applied in photoautotrophs to (1) characterize these non-model host organisms, (2) identify wasteful pathways that limit product yield, and (3) identify metabolic bottlenecks that restrict production.

2.4.1 APPLICATIONS OF FLUX ANALYSIS TO CYANOBACTERIA

There has been increased interest in the use of photosynthetic organisms as production hosts because of their advantageous ability to use CO_2 as their sole carbon source [50]. Cyanobacteria have been thoroughly probed and characterized through the application of isotope labeling experiments under heterotrophic, mixotrophic, and autotrophic conditions [22,51,52]. ^{13}C MFA was first applied to *Synechocystis* sp. PCC 6803 by Yang et al. to investigate central carbon metabolism under heterotrophic and mixotrophic conditions [53–55]. Using a mixed feed of 90% unlabeled glucose and 10% [U-^{13}C]glucose tracer under heterotrophic conditions, the study revealed the oxidative PP pathway (oxPP) to be used almost exclusively for energy production, with more than 90% of the incoming glucose metabolized by this pathway to produce NADPH for growth and respiration. In contrast, under mixotrophic conditions, CO_2 fixation flux through the Calvin cycle was approximately two-fold higher than glucose assimilation. This was fueled by ATP and NADPH production from photosynthetic light reactions. Additionally, a substantial cyclic flux through PEP carboxylase (PEPC) and malic enzyme (ME) was noted, which led to the postulation of a functional C4 pathway in cyanobacteria. In a complementary study, Yang et al. looked at the effects of glucose addition on mRNA transcript levels and protein expressions of key enzymes for carbon assimilation. This study showed that most of the changes in carbon pathway fluxes could not be explained by expression changes. This highlights the usefulness of ^{13}C MFA to uncover novel insights about regulatory mechanisms when combined with other ‘omics’ platforms.

Nakajima et al. [56] also combined ^{13}C MFA with other 'omics' platforms. This study investigated the underlying metabolic regulation mechanisms in *Synechocystis* sp. PCC 6803 under mixotrophic and photoheteroptrophic conditions by integrating metabolomics and transcriptomics with ^{13}C MFA. A drastic difference in fluxes between the two culture conditions was observed even though the changes in the gene expression levels and metabolite concentrations were small. This suggests that the differences in flux could not primarily be explained by the changes in expression levels of the corresponding genes. Oxidative pentose phosphate (OxPP) pathway flux was elevated under photoheterotrophic conditions to balance out the loss of NADPH that would have normally been produced photosynthetically, even though gene expression was unaffected. Transcriptomics data did suggest that the repression of the *gap1* gene, which encodes an isoform of glyceraldehye-3-phosophate dehydrogenase (GAPDH) that is essential for glycolytic glucose breakdown, functions as a control valve to shift carbon flow between glycolysis and oxPP pathway as a response to NADPH levels. Under photomixotrophic conditions in *Synechocystis*, You et al. [57] used $NaH^{13}CO_3$ and [U-^{13}C]glucose to show that flux through CO_2 fixation was higher than flux through glucose utilization, there was zero flux though the glyoxylate shunt, and that there was malic enzyme flux activity. These findings are in agreement with conclusions drawn from previous ^{13}C MFA studies [54,56]. Additionally, this study provided new perspectives into other pathways of central carbon metabolism, specifically the TCA cycle. Isotope dilution with glutamate detected minimal carbon flow through α-ketoglutarate to succinate, which is consistent with the recently discovered α-ketoglutarate decarboxylase bypass pathway [58].

Other strains of cyanobacteria have also been studied using ^{13}C MFA in addition to *Synechocystis.* An isotope labeling experiment of *Cyanothece* sp. ATCC 51142 looked at the effects of different carbon and nitrogen substrates on central carbon metabolism [59]. Using [U-^{13}C]glucose, [2-^{13}C]glycerol, and [3-^{13}C]pyruvate in either nitrogen-fixing or nitrogen-sufficient conditions, this study revealed that only glycerol addition increased growth under both conditions; neither glucose nor pyruvate addition enhanced growth. Taking a further look at the ^{13}C labeling data in amino acids, it was observed that carbon contribution from glycerol was much higher in comparison to contributions from glucose and pyruvate, consistent with the growth findings. Alagesan et al. [60] also applied ILEs to *Cyanothece* sp. ATCC 51142, but provided a more comprehensive flux analysis to estimate intracellular fluxes. This study was able to measure labeling in a greater number of amino acids, providing increased redundancy and pathway coverage. Flux analysis also revealed increased growth through the addition of glycerol to the media, as well as increased flux in CO_2 incorporation through PEP carboxylase, indicating C4-like metabolism.

In the past, most of the isotope labeling studies in cyanobacteria have been limited to mixotrophic or heterotrophic conditions because of the challenges associated with studying autotorophic growth. However, recent advances in mass spectrometry instrumentation and software capable of handling isotopically nonstationary growth conditions have enabled INST-MFA to be applied to cyanobacteria. Young et al. [6] first applied INST-MFA to model photoautotrophic growth in *Synechocystis* sp. 6803. Steady-state labeling was typically achieved in less than 10 minutes, with notable exception of

the TCA pathway intermediates. The resulting flux map that was generated using INST-MFA was compared to a previously published study using flux balance analysis (FBA) to predict the theoretical optimum flux need to maximize growth [5]. ^{13}C flux analysis results revealed that the cells exhibited suboptimal carbon efficiency, with significant loss of fixed CO_2 in the oxPP pathway. This study shows how the use of experimental isotope labeling measurements and flux analysis can be used to identify wasteful pathways that cannot be predicted solely by predictive modeling methods. Huege et al. [61] also performed a study using transient ^{13}C labeling studies to study wild-type *Synechocystis* and two photorespiratory pathway mutants in either high or low carbon conditions. While this study did not attempt to quantify flux estimates from carbon labeling data, this study did assess metabolite turnover to provide local flux estimates. Although the growth conditions in this study were different from the study performed by Young et al., the results of the wild-type strain in both studies were in agreement with one another. Both groups noted C3 metabolism as the primary source of carbon fixation through the enzyme RuBisCO, even though there was some notable C4 metabolism detected through PEPC. Additionally, both groups saw minimal flux through the photorespiratory pathway, agreeing with previous findings of the presence of carboxysomes in cyanobacteria, which are effective carbon concentrating mechanisms that function to elevate CO_2 concentration near RuBisCO [62]. Finally, both groups showed the possibility of metabolic channeling within pathways, where enzymes catalyzing successive reactions cluster together spatially in order to minimize diffusional imitations. This effect was revealed by more rapid ^{13}C enrichment of downstream metabolites in comparison to upstream metabolites, which could not be explained in the absence of metabolite channeling. The number of

flux analysis studies being applied to cyanobacteria have been increasing and there are now a handful of examples of how cyanobacteria have been characterized under different conditions that are steps closer to industrial production conditions. There are a number of academic labs and a few industrial companies attempting to use cyanobacteria as production hosts. Further application of flux analysis as a tool for pathway engineering can eventually lead to the identification of other wasteful pathways and potential metabolic bottlenecks.

2.4.2 APPLICATIONS OF FLUX ANALYSIS TO PLANTS

Pant metabolic engineering has been hindered in the past by a lack of understanding of the complex metabolic network structure, function, and regulation [63,64]. The application of flux analysis studies to plants in recent years have been highly informative and continue to pave a path for a better understanding of plant metabolic functioning and its implications for plant genetic engineering. A number of ^{13}C MFA studies have been recently applied to isolated plant cells or tissues under a variety of experimental conditions, such as maize root tips [65–68], tomato suspension cells [69], developing seeds of rapeseed [70–74], soybean [75–78], sunflower [79], maize kernels [80,81], and *Catharanthus rosesus* and *Nicotiana tabacum* hairy root cultures [82,83]. Several of these MFA results have interestingly revealed a similar pyruvate kinase bypass pathway, involving PEP carboxylase, malate dehydrogenase, and malic enzyme, to produce pyruvate. It was determined that 14% of mitochondrial pyruvate comes from mitochondrial malic enzyme in soybean seeds [78], 20% in developing sunflower seeds [79], and 40% in developing *Brassica napus* embryos [73]. Additionally, several of these

studies have revealed that a significant amount of cellular ATP is lost to futile substrate cycles [65–67,71].

While the use of steady state MFA has been informative to many plant studies, it is more applicable to look at isotopic labeling time-courses when studying photoautotrophic metabolism in plants [84,85]. In particular, transient labeling experiments have been recently applied in combination with INST-MFA or kinetic flux profiling (KFP) to characterize flux phenotypes in complex photosynthetic systems. Chapters 4 and 5 of this dissertation discuss the work we have carried out to apply INST-MFA to *Arabidopsis thaliana*. Szecowka et al. [86] recently applied KFP to *Aradibdopsis* rosettes. KFP requires both isotopic labeling data and the measurement of subcellular pool sizes, and it is this requirement of direct pool size measurements that makes this technique arguably more difficult to implement. This point was discussed in a recent review article [87] and it remains to be seen whether the KFP protocol described in [88] will be adopted in the future for exploring photosynthetic metabolism in plants. Overall, it is clear that there are emerging methods being developed and applied to study photoautotrophic metabolism in plants, which represents an important step toward improving product yield and/or biomass productivity in plant hosts, which are not amenable to high-throughput engineering approaches.

2.5 CONCLUSION

Photoautotrophic metabolism is a highly fascinating, yet complex process that serves as the underlying method in which all food on earth and bio-based chemicals are produced. ^{13}C flux analysis, in particular INST-MFA, is an ideal way to assess the metabolic phenotype of many photosynthetic hosts being used as production platforms for either bio-based chemicals or biomass itself. In the rest of this dissertation, the application of INST-MFA to dissect metabolic pathways associated with photoautotrophic metabolism will be discussed in more detail.

2.6 APPENDIX: SIMPLE NETWORK EXAMPLE FOR INST-MFA CALCULATIONS

A simple metabolic network appears in **Figure 2A.1** as an example of how to construct the stoichiometric matrix *S*, identify the set of EMUs required to simulate MIDs of measured metabolites, and set up dynamic isotopomer balances on these EMUs. Table 2A.1 delineates the atom transitions for the network. In this network example, metabolite A is the sole substrate and metabolite G is the only final product. The intermediary metabolites B, C, D, E, and F are assumed to be at metabolic steady state, but isotopically nonstationary.

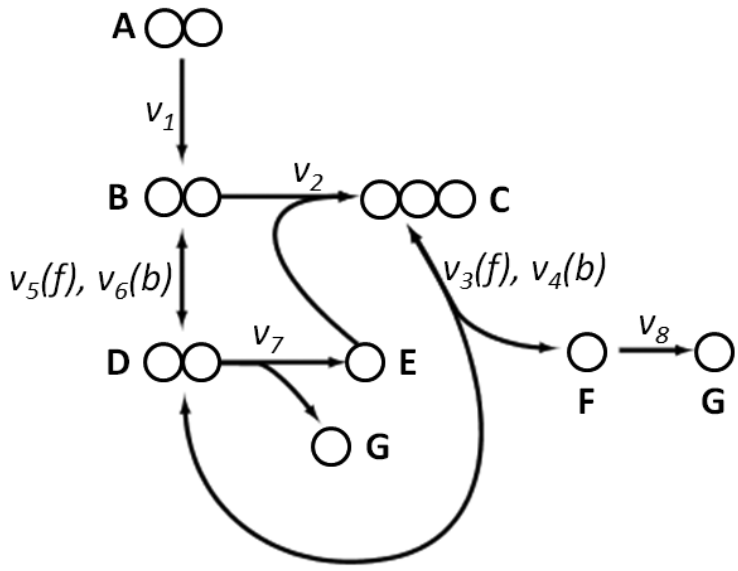

Figure 2A.1. Simple metabolic network used to illustrate the decomposition into EMUs.

Atom transitions for the reactions in this model are given in Table 2A.1. The network fluxes are assumed to be constant since the system is at metabolic steady state. Extracellular metabolite A is assumed to be at a fixed state of isotopic labeling to which intracellular metabolites B, C, D, E, F, and G adapt over time.

Table 2A.1. Stoichiometry and atom transitions for the reactions in the example metabolic network.

Reaction no.	Reaction stoichiometry	Atom transitions
1	A → B	ab → ab
2	B + E → C	ab + c → abc
3 and 4	C ↔ D + F	abc ↔ cb + a
5 and 6	B ↔ D	ab ↔ ab
7	D → E + G	ab → b + a
8	F → G	a → a

The stoichiometric matrix S is shown below, which has $k = 5$ intermediary metabolites and $j = 8$ fluxes, resulting in a 5 × 8 matrix.

$$S = \begin{bmatrix} 1 & -1 & 0 & 0 & -1 & 1 & 0 & 0 \\ 0 & 1 & -1 & 1 & 0 & 0 & 0 & 0 \\ 0 & 0 & 1 & -1 & 1 & -1 & -1 & 0 \\ 0 & -1 & 0 & 0 & 0 & 0 & 1 & 0 \\ 0 & 0 & 1 & -1 & 0 & 0 & 0 & -1 \end{bmatrix}$$

Therefore, $S \cdot v = 0$ is expressed in vector form as

$$\begin{bmatrix} v_1 - v_2 - v_5 + v_6 \\ v_2 - v_3 + v_4 \\ v_3 - v_4 + v_5 - v_6 - v_7 \\ -v_2 + v_7 \\ v_3 - v_4 - v_8 \end{bmatrix} = 0$$

A systematic method of EMU network decoupling in which metabolite units are grouped into mutually dependent blocks is described through this simple network example. For this example, we will set up the simplest possible model to simulate the MID of metabolite C, i.e., EMU C_{123}. First, we need to identify all the possible EMUs that contribute to the formation of C_{123} – in this reaction model, C_{123} is formed from the condensation of B_{12}+E_1 and D_{12}+F_1 in reactions 2 and 4, respectively. This is recorded

and the process is then repeated for all new EMUs, starting with the largest EMU in size; in this case, all EMUs of size 3 have already been identified. Next, the process is repeated to determine all the EMUs of size 2 that were previously identified, starting with D_{12}. D_{12} is formed from two different reactions – from B_{12} in reaction 5 and from C_{23} in reaction 3. Following this, we determine which reactions form C_{23}; C_{23} is formed from D_{12} in reaction 4 and B_2+E_1 in reaction 2. Finally, we need to determine which reactions form B_{12}. B_{12} is formed from A_{12} and D_{12} in reactions 1 and 6, respectively. A_{12} is a network substrate and is not produced by any other reactions and D_{12} has already been considered in the previous step. Therefore, all EMU reactions of size 2 have been identified. The process is repeated once again for EMUs of size 1, until all the EMUs have been traced back to network substrates or previously identified EMUs. **Table 2A.2** shows the complete EMU decomposition of this system, which involves 24 EMU reactions connecting 16 EMUs.

After EMU decomposition, the reaction network can be further decoupled into blocks, which group together minimal sets of mutually dependent metabolite units that must be solved simultaneously. **Figure 2A.2** shows the EMU network decomposition for the simple network example after block decoupling. The blocks are arranged so that each one is a self-contained subproblem, which will depend on the outputs of the previously solved blocks. Therefore, EMUs in block 1 should first be solved, then block 2, etc.

Table 2A.2. Complete list of EMU reactions generated for metabolite C.

Subscripts denote atoms that are part of their respective EMUs. The EMU reactions are also divided into their respective blocks after Dulmage-Mendelsohn decomposition has been applied.

Reaction no.	EMU reaction	EMU reaction size balance	Block
2	$B_{12} + E_1 \rightarrow C_{123}$	2 +1 = 3	6
4	$D_{12} + F_1 \rightarrow C_{123}$	2 +1 = 3	6
2	$B_2 + E_1 \rightarrow C_{23}$	1 + 1 = 2	5
4	$D_{12} \rightarrow C_{23}$	2 = 2	5
3	$C_{23} \rightarrow D_{12}$	2 = 2	5
5	$B_{12} \rightarrow D_{12}$	2 = 2	5
6	$D_{12} \rightarrow B_{12}$	2 = 2	5
1	$A_{12} \rightarrow B_{12}$	2 = 2	5
2	$B_1 \rightarrow C_1$	1 = 1	4
4	$F_1 \rightarrow C_1$	1 = 1	4
3	$C_1 \rightarrow F_1$	1 = 1	4
2	$E_1 \rightarrow C_3$	1 = 1	3
4	$D_1 \rightarrow C_3$	1 = 1	3
3	$C_3 \rightarrow D_1$	1 = 1	3
5	$B_1 \rightarrow D_1$	1 = 1	3
6	$D_1 \rightarrow B_1$	1 = 1	3
1	$A_1 \rightarrow B_1$	1 = 1	3
7	$D_2 \rightarrow E_1$	1 = 1	2
2	$B_2 \rightarrow C_2$	1 = 1	1
4	$D_2 \rightarrow C_2$	1 = 1	1
1	$A_2 \rightarrow B_2$	1 = 1	1
6	$D_2 \rightarrow B_2$	1 = 1	1
5	$B_2 \rightarrow D_2$	1 = 1	1
3	$C_2 \rightarrow D_2$	1 = 1	1

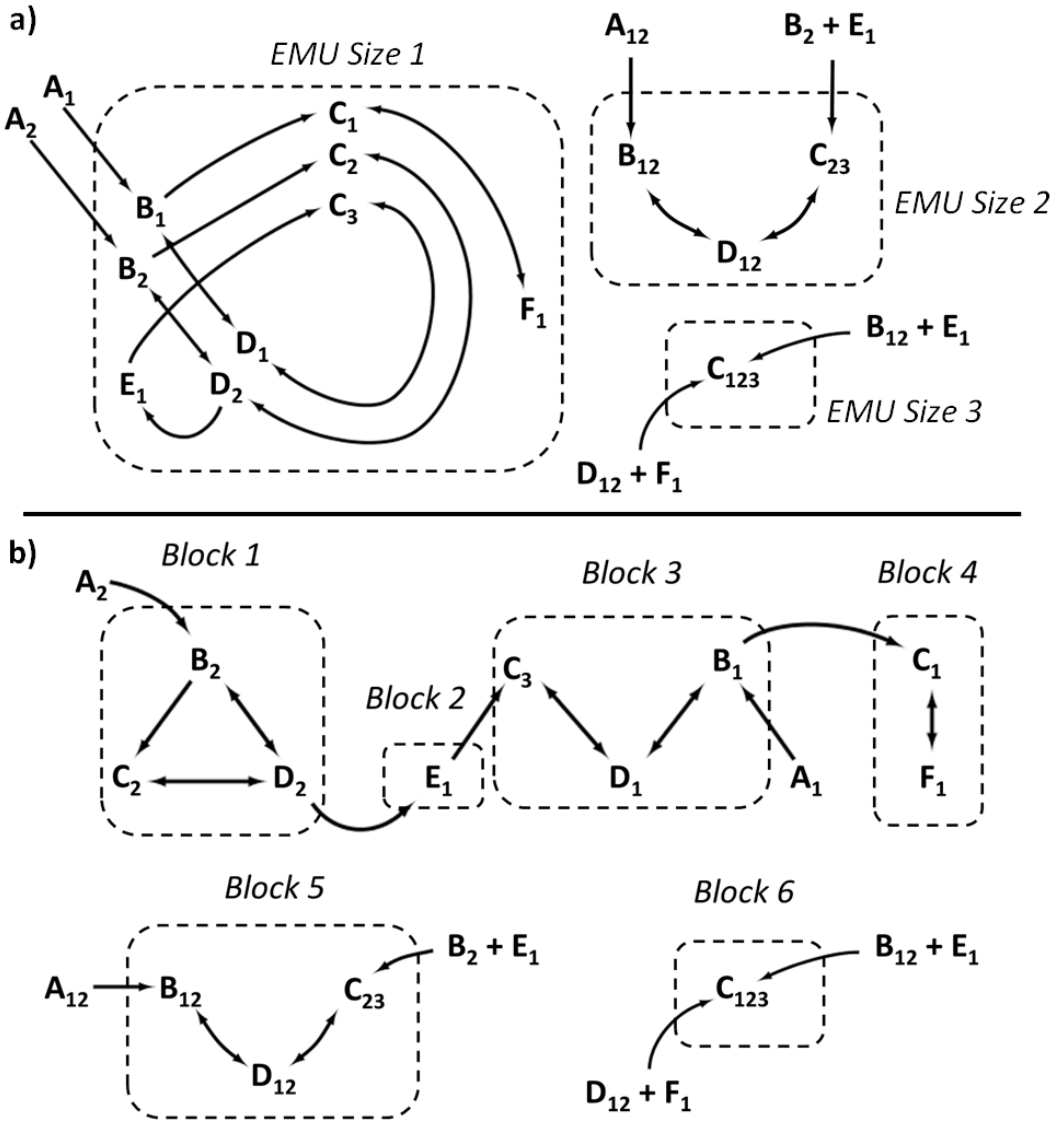

Figure 2A.2. EMU Network decompositions.

a) EMU network decomposition for simple example network (**Figure 2A.1**) generated to simulate the labeling of metabolite C. The EMU network was decoupled based on EMU size and network connectivity. b) EMU network decomposition for the same network using block decoupling. Subscripts refer to the atoms that are contained within the EMU.

The EMU reactions obtained from network decomposition and block decoupling form the new basis for generating system equations. The decoupled blocks can be arranged into a cascaded system of ODEs with the following form, as described in section 2.3.2.

$$\mathbf{C}_n \cdot \frac{\mathrm{d}\mathbf{X}_n}{\mathrm{d}t} = \mathbf{A}_n \cdot \mathbf{X}_n + \mathbf{B}_n \cdot \mathbf{Y}_n$$

The concentration matrix $\mathbf{C}_n$ is a diagonal matrix whose elements are pool sizes corresponding to EMUs represented in $\mathbf{X}_n$. $\mathbf{X}_n$ is comprised of row vectors that represent the MIDs of each EMU and $\mathrm{d}\mathbf{X}_n/\mathrm{d}t$ is the time derivative of $\mathbf{X}_n$. Analogously, the input matrix $\mathbf{Y}_n$ is also comprised of row vectors that represent MIDs of EMUs that have been previously calculated. The system matrices $\mathbf{A}_n$ and $\mathbf{B}_n$ come from calculating the "true" flux vectors (v) based on the chosen free fluxes (u) and null space matrix (N). Furthermore, in the decoupled blocks, the full MID of products formed from condensation reactions can be obtained from the convolution (or Cauchy product, denoted by '×') of MIDs of preceding EMUs. In the case of C_{123}, these MIDs are B_{12} and E_1 or D_{12} and F_1 i.e., $C_{123}=B_{12}\times E_1$ or $C_{123}=D_{12}\times F_1$. The following equations represent the system of ODEs for the simple network example.

$$\begin{bmatrix} C_c & 0 & 0 \\ 0 & C_B & 0 \\ 0 & 0 & C_D \end{bmatrix} \begin{bmatrix} \frac{dC_2}{dt} \\ \frac{dB_2}{dt} \\ \frac{dD_2}{dt} \end{bmatrix} = \begin{bmatrix} -v_2 - v_4 & v_2 & v_4 \\ 0 & -v_1 - v_6 & v_6 \\ v_3 & v_5 & -v_3 - v_5 \end{bmatrix} \begin{bmatrix} C_2 \\ B_2 \\ D_2 \end{bmatrix} + \begin{bmatrix} 0 \\ v_1 \\ 0 \end{bmatrix} [A_2]$$

$$[C_E] \left[\frac{dE_1}{dt}\right] = [-v_7][E_1] + [v_7][D_2]$$

$$\begin{bmatrix} C_c & 0 & 0 \\ 0 & C_D & 0 \\ 0 & 0 & C_B \end{bmatrix} \begin{bmatrix} \frac{dC_3}{dt} \\ \frac{dD_1}{dt} \\ \frac{dB_1}{dt} \end{bmatrix} = \begin{bmatrix} -v_2 - v_4 & v_4 & 0 \\ v_3 & -v_3 - v_5 & v_5 \\ 0 & v_6 & -v_1 - v_6 \end{bmatrix} \begin{bmatrix} C_3 \\ D_1 \\ B_1 \end{bmatrix} + \begin{bmatrix} v_2 & 0 \\ 0 & 0 \\ 0 & v_1 \end{bmatrix} \begin{bmatrix} E_1 \\ A_1 \end{bmatrix}$$

$$\begin{bmatrix} C_c & 0 \\ 0 & C_F \end{bmatrix} \begin{bmatrix} \frac{dC_1}{dt} \\ \frac{dF_1}{dt} \end{bmatrix} = \begin{bmatrix} -v_2 - v_4 & v_4 \\ v_3 & -v_3 \end{bmatrix} \begin{bmatrix} C_1 \\ F_1 \end{bmatrix} + \begin{bmatrix} v_2 \\ 0 \end{bmatrix} [B_1]$$

$$\begin{bmatrix} C_c & 0 & 0 \\ 0 & C_D & 0 \\ 0 & 0 & C_B \end{bmatrix} \begin{bmatrix} \frac{dC_{23}}{dt} \\ \frac{dD_{12}}{dt} \\ \frac{dB_{12}}{dt} \end{bmatrix}$$

$$= \begin{bmatrix} -v_2 - v_4 & v_4 & 0 \\ v_3 & -v_3 - v_5 & v_5 \\ 0 & v_6 & -v_1 - v_6 \end{bmatrix} \begin{bmatrix} C_{23} \\ D_{12} \\ B_{12} \end{bmatrix} + \begin{bmatrix} v_2 & 0 \\ 0 & 0 \\ 0 & v_1 \end{bmatrix} \begin{bmatrix} B_2 \times E_1 \\ A_{12} \end{bmatrix}$$

$$[C_C] \left[\frac{dC_{123}}{dt}\right] = [-v_2 - v_4][C_{123}] + [v_2 \quad v_4] \begin{bmatrix} B_{12} \times E_1 \\ D_{12} \times F_1 \end{bmatrix}$$

Solving this system of ODEs will simulate the EMU labeling trajectories needed to calculate the time-dependent mass isotopomer distribution of metabolite C. The flux and pool size parameters can then be adjusted iteratively using an optimization search algorithm to converge on parameter values that minimize the lack-of-fit with experimental mass isotopomer data.

3. ISOTOPICALLY NONSTATIONARY ^{13}C FLUX ANALYSIS OF CYANOBACTERIAL ISOBUTYRALDEHYDE PRODUCTION

3.1 ABSTRACT

Synechococcus elongatus PCC 7942 has been engineered to produce isobutyraldehyde (IBA), a precursor for the biofuel isobutanol. Isotopically nonstationary ^{13}C metabolic flux analysis (INST-MFA) was applied to the IBA-producing *S. elongatus* strain SA590 and a wild-type (WT) control strain. Comparison of flux maps generated for the two strains identified a potential bottleneck at the pyruvate kinase (PK) reaction step that was associated with diversion of flux into a three-step PK bypass pathway involving the enzymes PEP carboxylase (PEPC), malate dehydrogenase (MDH), and malic enzyme (ME). Single-gene overexpression of PK in the parental SA590 strain led to 56% improvement in IBA specific productivity. Single-gene overexpression of the three enzymes in the proposed PK bypass pathway also led to improvements in IBA production, although not to the same extent as PK overexpression. However, combined overexpression of two of the three enzymes in the proposed PK bypass pathway (MDH and ME) led to 68% improvement in specific productivity. This study shows how ^{13}C flux analysis can be used to identify potential metabolic bottlenecks and to guide rational metabolic engineering to increase biochemicals production from photosynthetic host cells.

3.2 INTRODUCTION

Recent studies have demonstrated the feasibility of converting energy from sunlight and carbon from CO_2 directly into biofuels using photosynthetic microorganisms [89,50]. Specifically, cyanobacteria offer a direct process for capturing light and concentrated CO_2 into biomass, and can be installed in locations that do not compete with food for water and land resources. In addition to the growing number of engineered pathways for the conversion of CO_2 into useful products in cyanobacteria, tools for design and genetic manipulation are also becoming diverse [90,91,1,52]. However, despite the advances made in cyanobacterial biofuels production, the growth rates and productivities achieved in cyanobacteria are not economically feasible and are often lower than that of heterotrophic bacteria currently used in industry [92,93]. Additionally, there are few tools available that specifically address the challenges of determining and redirecting metabolic flux in photosynthetic microbes.

As previously discussed in Chapter 2, isotope labeling experiments and metabolic flux analysis (MFA) studies have recently been carried out to accurately assess *in vivo* regulation of photosynthetic metabolism. This has been crucial to identifying potential pathways that will maximize carbon flux from the Calvin cycle, where CO_2 fixation occurs, into biofuel-producing pathways. One promising biofuel-producing pathway engineered into the cyanobacteria *Synechococcus elongatus* PCC 7942 involves the production of isobutyraldehyde [94]. This engineered strain showed relatively high-flux production of isobutyraldehyde (1100 mg/L) and demonstrates the feasibility for commercial scale synthesis from CO_2. Additionally, isobutyraldehyde is a direct

precursor of the potential fuel substitute, isobutanol, which has several properties that make it an attractive biofuel option over the first generation biofuel, ethanol. Isobutanol has a relatively high energy density (98% of gasoline), has low water solubility, which prevents the corrosion of engines and pipelines, and can be mixed at any proportion with gasoline, allowing it to be a "drop in" replacement or additive to the existing petroleum infrastructure [95]. Compared to isobutanol, isobutyraldehyde is a more advantageous target product for biosynthesis in our studies because it has been previously shown to be less toxic to *S. elongatus* cells [94].

Previously, Young et al. [6] mapped carbon fluxes in the cyanobacterium *Synechocystis* sp. PCC 6803 by applying isotopically nonstationary metabolic flux analysis (INST-MFA) under photoautotrophic condition. The flux analysis revealed unanticipated photosynthetic inefficiencies tied to oxidative metabolic pathways, despite minimal photorespiration. In this study, we aimed to close the 'design-build-test-learn' metabolic engineering cycle by applying isotopically nonstationary metabolic flux analysis (INST-MFA) an engineered strain of *S. elongatus*, so that we could pinpoint wasteful byproduct pathways and potential bottlenecks towards isobutyraldehyde production. *S. elongatus* can only grow under photoautotrophic conditions, thus necessitating the need for transient labeling conditions and INST-MFA. The INST-MFA results showed a bottleneck at the pyruvate node, specifically at the pyruvate kinase (PK) reaction, which catalyzes the conversion of phosphoenolpyruvate into pyruvate. Pyruvate is a precursor of isobutyraldehyde production. Additionally, the results highlighted a natural PK bypass pathway, which we propose involves the three enyzmes that direct carbon from the

metabolite phosphoenolpyruvate to oxaloacetate to malate and finally into pyruvate; the accompanying enzymes to these reactions involve phosphoenolpyruvate carboxylase (PEPC), malate dehydrogenase (MDH), and malic enzyme (ME). Based on these results, we generated single-, double-, and triple-gene overexpression strains in the parental isobutyraldehyde producing strain to investigate the effects of these genetic manipulations on isobutyraldehyde production. We were able to see significant increases in isobutyraldehyde productivity in two of these engineered strains, which have been identified for further flux analysis characterization in future rounds of metabolic engineering. This work highlights the importance and usefulness of flux analysis to identify rational targets for strain engineering in cyanobacterial hosts, so that industrial feasibility in these photosynthetic organisms can ultimately be attained.

3.3 METHODS

3.3.1 MEDIUM AND CULTURE CONDITIONS

Synechococcus elongatus strain PCC 7942 was obtained from the Johnson lab at Vanderbilt University and serves as the wild-type (WT) strain. The parental IBA-producing strain (SA590) was obtained from the Liao lab at UCLA [94]. All other engineered strains generated for this study were constructed by the Johnson lab. The WT and engineered *S. elongatus* 7942 strains (Table 3.1) were grown on modified BG-11 agar [96] (1.5% w/v) plates with appropriate antibiotics (40 µg/mL spectinomycin, 10 µg/mL kanamycin, and/or 4 µg/mL carbenicillin). All strains were cultured in modified BG-11 medium containing an additional 50 mM $NaHCO_3$ with appropriate antibiotics in

shake flasks. Precultures were grown under 150 μE m^{-2} s^{-1} light, supplied by 8 custom fluorescent lights (Build My LED, LLC, Austin, TX) at 30°C with rotary shaking at 130 rpm, bubbling with air. Light was measured using a PAR quantum flux meter (Apogee Instruments, Logan, UT). Cell density was monitored by measuring OD_{750}.

Table 3.1. Strains used in this study.

Strain	Description	Reference
WT	Wild-type *S. elongatus* PCC 7942	S.S. Golden
SA590	IBA-producing parental strain. P_{trc}::*kivd* in NSI ($Spec^R$), $P_L lacO_1$::*alsS-alvC-alvD* in NSII (Km^R)	[94]
SA590-PK	SA590 P_{trc}::*pyk* in NS III (Cb^R)	This work
SA590-PEPC	SA590 P_{trc}::*pepc* in NS III (Cb^R)	This work
SA590-MDH	SA590 P_{trc}::*mdh* in NS III (Cb^R). The *Synechocystis* sp. PCC 6803 *mdh* gene was codon-optimized for expression in *S. elongatus.*	This work
SA590-ME	SA590 P_{trc}::*me* in NS III (Cb^R)	This work
SA590-MDH/ME	SA590 P_{trc}::*mdh*, P_{trc}::*me* in NS III (Cb^R)	This work
SA590-PEPC/MDH/ME	SA590 P_{trc}::*pepc,* P_{trc}::*mdh*, P_{trc}::*me* in NS III (Cb^R)	This work

3.3.2 QUANTIFICATION OF ALDHEYDE PRODUCTION

Precultures were used to inoculate 75 mL of fresh medium to an initial OD_{750} of 0.4 in 125 mL flasks. After inoculation, the cultures were supplemented with 50 mM NaHCO3 as an inorganic carbon source and were placed in the dark for 12 hours to synchronize the circadian rhythms of the cells. Flasks were then removed from the dark and spiked with 1

mM isopropyl-β-D-1-thiogalactoside (IPTG) to induce expression of the recombinant genes. After the dark pulse, all cultures were allowed to grow in continuous light with air bubbling. Six hours after being placed in the light, cultures were closed with rubber stoppers to prevent loss of any product during incubation for the next 24 hours. Culture samples (1 mL) were collected at the start (t=6hr) and end (t=30hr) of the 24-hour incubation period and analyzed for aldehyde concentration and growth.

Culture samples were centrifuged for 5 min at 15,000 rpm to remove cells. Then, 495 µL of the supernatant was mixed with 5 µL of 100 mM n-butyraldehyde (nBA) as internal standard. The mixture was vortexed and directly analyzed on a GC-FID (Shimadzu GC-2010 system with flame ionization detector) using a DB-WAX column (30m, 0.20 mm ID, 0.20 µm film thickness) from Agilent Technologies (Santa Clara, CA). The injector and detector temperatures were maintained at 210°C and 250°C, respectively. Helium was used as the carrier gas, and the injection volume was 0.5 µL. The GC oven temperature was initially held at 30°C for 6 min and then raised to 60°C with a temperature ramp of 6°C/min. The GC oven was then maintained at 60°C for 2 min, then raised to 220°C with a ramp of 40°C/min. Finally, the oven was held at 220°C for 7 minutes before completion of analysis. Column flow rate was 0.78 mL/min and the purge flow rate was 0.5 mL/min. IBA and isovaleraldehyde (IVA) peaks were identified and normalized to the internal standard peak. Serial dilutions of IBA and IVA standards with concentrations in the range of 0.01–2 mM were used to construct calibration curves. The amounts of IBA and IVA in each sample were calculated based on the ratios of the integrated IBA/nBA and IVA/nBA peak areas using linear regression from the

corresponding calibration curve. Specific productivity was calculated by using the publically available MATLAB-based software package Extracellular Timecourse Analysis [97], which takes into account cellular growth to regress metabolite uptake and production rates based on cell density and metabolite concentrations at given time points.

3.3.3 ^{13}C LABELING EXPERIMENTS

Precultures were used to inoculate 500 mL of fresh medium to an initial OD_{750} of 0.4 in 1 L flasks. After inoculation, the flasks were placed in the dark for 12 hours to synchronize the circadian rhythm of the cells. Flasks were then removed from the dark after 12 hours and induced with 1 mM isopropyl-β-D-1-thiogalactoside (IPTG) to begin expression of the introduced genes. After the dark pulse, all cultures were allowed to grow in continuous light and air bubbling. The labeling experiment was initialized 30 hours after the dark pulse, when the cell density had reached an OD_{750} of 0.6-0.8. A 20mL sample corresponding to t=0 (unlabeled) was withdrawn from the flask using a syringe and luer-lock needle (12 gauge, 12", Sigma-Aldrich). Airflow was stopped to prevent unlabeled CO_2 from entering the system. A 50 mL aliquot of BG11 media with added $NaH^{13}CO_3$ (Cambridge Isotope Laboratories, 97% isotopic purity) was quickly introduced to the culture to achieve a final tracer concentration of 100 mM. Following this pulse, a series of 20mL samples were withdrawn and rapidly quenched at time points 30, 60, 120, 180, 300, 600, and 900 s.

Each sample was quenched in a 50 mL centrifuge tube that contained 30 mL of partially-frozen PBS maintained at 0°C on ice. Each quenched sample was centrifuged for 15 min at 5000 rpm and -10°C. The supernatant was discarded and the cell pellet was extracted using a modified Folch extraction method, which utilizes a biphasic chloroform:methanol:water (8:4:3) solvent mixture [98]. Polar metabolites were recovered in the methanol/water phase. Norvaline was added as an internal standard to all samples at the start of the extraction process to achieve a final concentration of 6.67 μM in the derivatized solution.

3.3.4 SAMPLE PREPARATION AND DERIVATIZATION

Derivatization for GC-MS was initiated by dissolving evaporated polar metabolite extracts in 50 mL of methoxyamine reagent (MOX; Pierce, Rockford, IL), sonicating at room temperature for 30 min, then incubating at 40°C for 90 min. 70 mL of BSTFA + 10% TMCS (TMS; Pierce) was added, and the sample was incubated at 40°C for an additional 30 min. The sample was further incubated and placed in a refrigerator at 4°C overnight to ensure full derivatization. Lastly, the samples were centrifuged at 14,000 RPM to pellet any undissolved residue. The resulting methoxime-trimethylsilyl (MOX-TMS) derivatives were subjected to GC-MS analysis.

3.3.5 GC-MS MEASUREMENT OF METABOLITE LABELING AND POOL SIZE

The GC-MS method was adapted from Young et al. [6] and was performed using an Agilent 7890 gas chromatograph equipped with a DB-35ms column (30m x 0.25 mm i.d.

x 0.25mm; Agilent J&W Scientific). The injection volume was 1 μL and all samples were run in splitless mode with an inlet temperature of 270°C. Helium flow rate was set to 1 mL/min and purge flow of 50 mL/min was set to activate 2 min after injection. The GC oven temperature was held at 80°C for 5 min, ramped at 10°C/min to 320°C, and held at 320°C for an additional 5 min. Mass spectra were obtained in scan mode over the range 100-800 m/z. Raw ion chromatograms were integrated using a custom MATLAB M-file that applies consistent integration bounds and baseline correction to each ion [99].

3.3.6 ISOTOPOMER NETWORK MODEL

An isotopomer model describing photosynthetic central carbon metabolism in *S. elongatus* PCC 7942 was adapted from a previous *Synechocystis* reaction network [6]. All isotopic measurements used for flux determination are listed in Table 3.2, and a list of the reactions included in the biochemical reaction network is provided in the Appendix. INST-MFA was used to estimate intracellular metabolic fluxes. Least-squares parameter regression, and statistical and sensitivity analysis of the optimal solution, were performed by using the publicly available software package Isotopomer Network Compartmental Analysis [24], which runs within MATLAB^{TM}. INCA relies on an elementary metabolite unit decomposition of the underlying isotopomer network to efficiently simulate the effects of varying fluxes on the labeling trajectories of measurable metabolites. Metabolic fluxes and pool sizes were estimated by minimizing the lack-of-fit between experimentally measured and computationally simulated mass isotopomer distributions (MIDs) by using a Levenberg-Marquardt optimization algorithm [20]. Flux evaluation was repeated a minimum of 50 times from random initial values to obtain best-fit

estimates. All results were subjected to a chi-square statistical test to assess goodness of fit, and accurate 95% confidence intervals were computed for all estimated parameters by evaluating the sensitivity of the sum-of-squared residuals (SSR) to parameter variations [34].

Table 3.2. **Isotope labeling measurements used for metabolic flux determination.**

Metabolite	Mass	Carbons	Composition
3PGA	459	1 2 3	C14 H36 O7 P Si4
3PGA	357	2 3	C11 H30 O5 P Si3
F6P	357	5 6	C11 H30 O5 P Si3
G6P	471	3 4 5 6	C16 H40 O6 P Si4
G6P	357	4 5 6	C11 H30 O5 P Si3
PEP	369	1 2 3	C11 H26 O6 P Si3
ALA	116	2 3	C5 H14 N Si
2PG	357	1 2	C10 H26 O6 P Si3
2PG	328	2	C10 H29 O4 P Si3
GLY	276	1 2	C10 H26 N O2 Si3
GLY	174	2	C7 H20 N Si2
SER	306	1 2 3	C11 H28 N O3 Si3
GA	307	1 2 3	C11 H27 O4 Si3
GA	292	2 3	C11 H28 O3 Si3
CIT	465	1 2 3 4 5 6	C17 H37 O7 Si4
CIT	363	1 2 3 4 5	C14 H31 O5 Si3
AKG	304	1 2 3 4 5	C11 H22 N O5 Si2
SUC	247	1 2 3 4	C9 H19 O4 Si2
FUM	245	1 2 3 4	C9 H17 O4 Si2
MAL	233	2 3 4	C9 H21 O3 Si2

3.4 RESULTS

3.4.1 GROWTH AND ISOBUTYRALDEHYDE PRODUCTION

Comparison of growth and IBA production between the WT and SA590 strains was used to assess the metabolic impact of genetic manipulations introduced in SA590 (Figure 3.1). There was no significant difference in growth rate between the WT and SA590 strains. As expected, the WT strain did not produce IBA. We initially hypothesized that the introduction of new carbon-consuming pathways in the engineered strains would result in decreased growth, with carbon being potentially redirected away from biomass. However, the reduction in growth was not significant, indicating low metabolic burden due to IBA production in the engineered strain. We also measured tolerance of WT *S. elongatus* to isobutyraldehyde in the closed flask collection system and saw that there was no significant effect on growth within the expected range of IBA concentrations (Figure 3A.1).

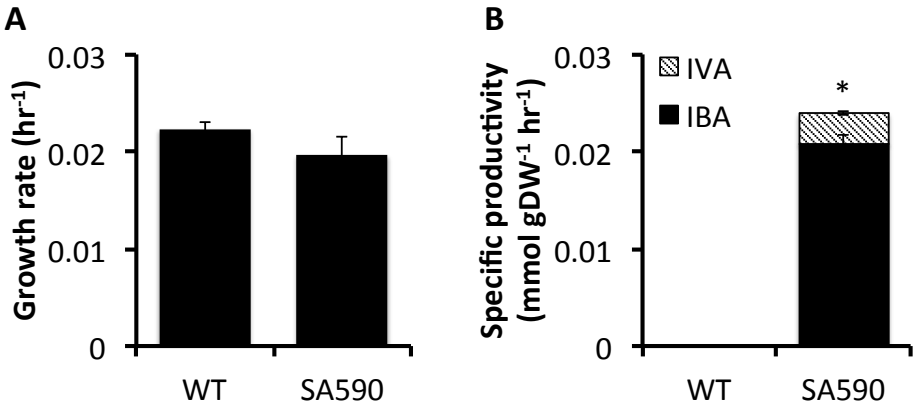

Figure 3.1. (A) Growth rate and (B) aldehyde specific productivity in WT and SA590 strains.

Data ± SE; n≥3.

While assessing samples for IBA production, we detected an additional aldehyde compound produced by SA590 cultures. This compound was identified as isovaleraldehyde (IVA) through comparison to IVA standards. We hypothesize that the recombinant ketoisovalerate decarboxylase (*kivd)* enzyme, which converts ketoisovalerate to IBA, also facilitates the conversion of ketoisocaproate to IVA. Ketoisocaproate is a precursor found in the leucine biosynthesis pathway, which branches off from the valine biosynthesis pathway that leads to IBA. The relative abundance of IVA was approximately 13% of the total aldehydes produced (IBA + IVA). This pointed to the leucine biosynthetic pathway as a potential knockdown target in future studies to shunt carbon flux back towards the intended IBA production pathway.

3.4.2 ISOTOPICALLY NONSTATIONARY METABOLIC FLUX ANALYSIS

INST-MFA was applied to characterized and compare the WT and SA590 strains. The measured MIDs, growth, and aldehyde production rates were used to construct comprehensive flux maps of photoautotrophic metabolism using a modified version of the reaction network developed by Young et al. [6] for wild-type *Synechocystis.* The SA590 flux map is shown in Figure 3.2. The major carbon fluxes occurred in the CBB cycle, where carbon fixation takes place. We also observed little to no flux through the photorespiratory pathway [100]. Additionally, there was minimal flux through the oxidative arm of the TCA cycle (citrate to α-ketogluatarate), which is consistent with previous flux analysis studies performed in cyanobacteria [6,57]. The fits were statistically acceptable based on a chi-square test of the SSR, which was assessed at the 95% confidence level with 358 degrees of freedom for both models (SSR=376.3 and

397.6 for the WT and SA590 flux maps, respectively with the expected range [307.5, 412.3]. The full list of optimal parameter estimates including net fluxes, exchange fluxes, subcellular fluxes, and pool sizes for both WT and SA590 can be found in the Appendix.

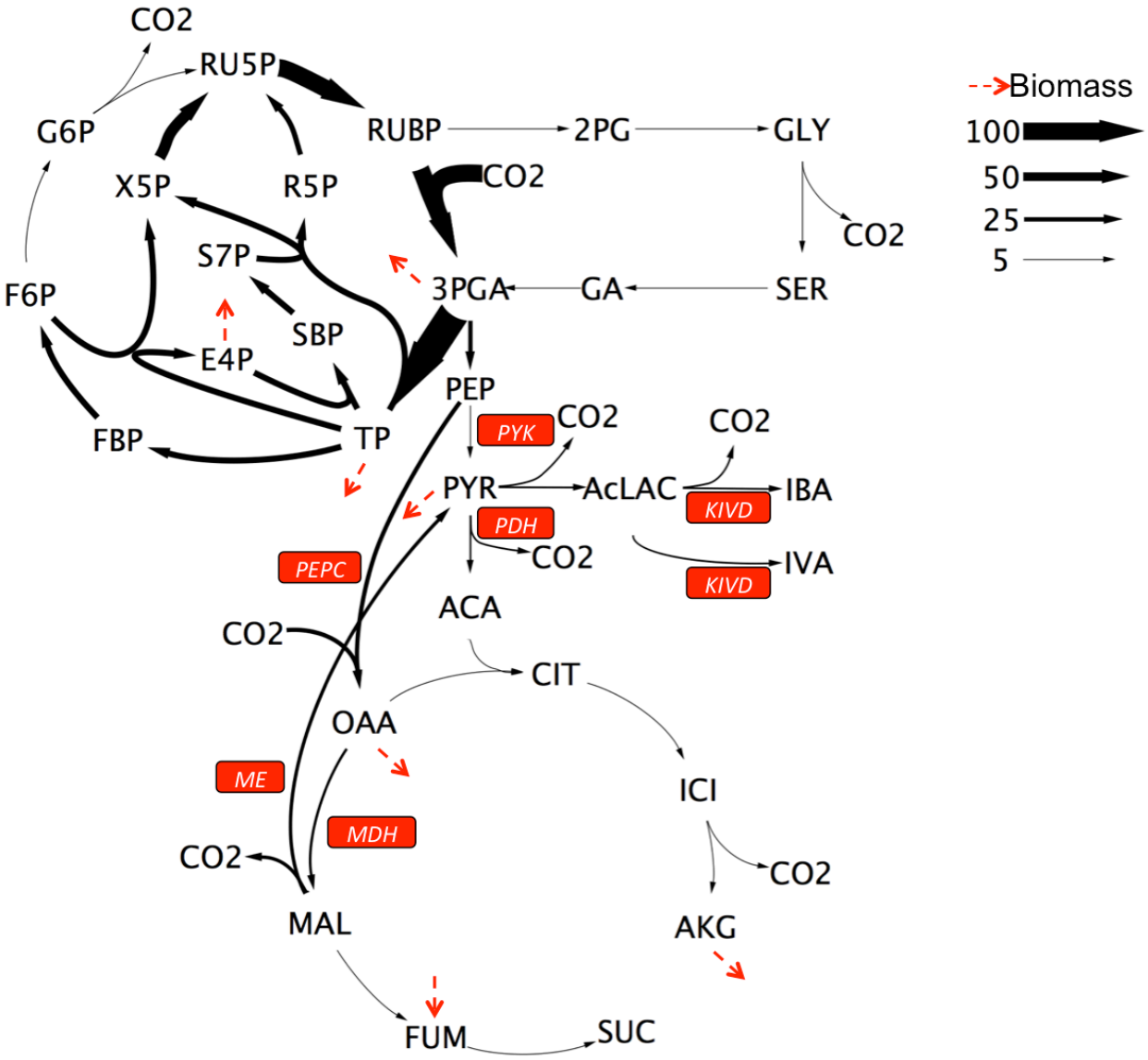

Figure 3.2. Flux map of engineered *S. elongatus* IBA-producing strain determined under photoautotrophic conditions.

Fluxes are shown normalized to a net CO2 uptake rate of 100. Arrow thickness is scaled proportional to net flux. Dotted arrows indicate fluxes to biomass formation.

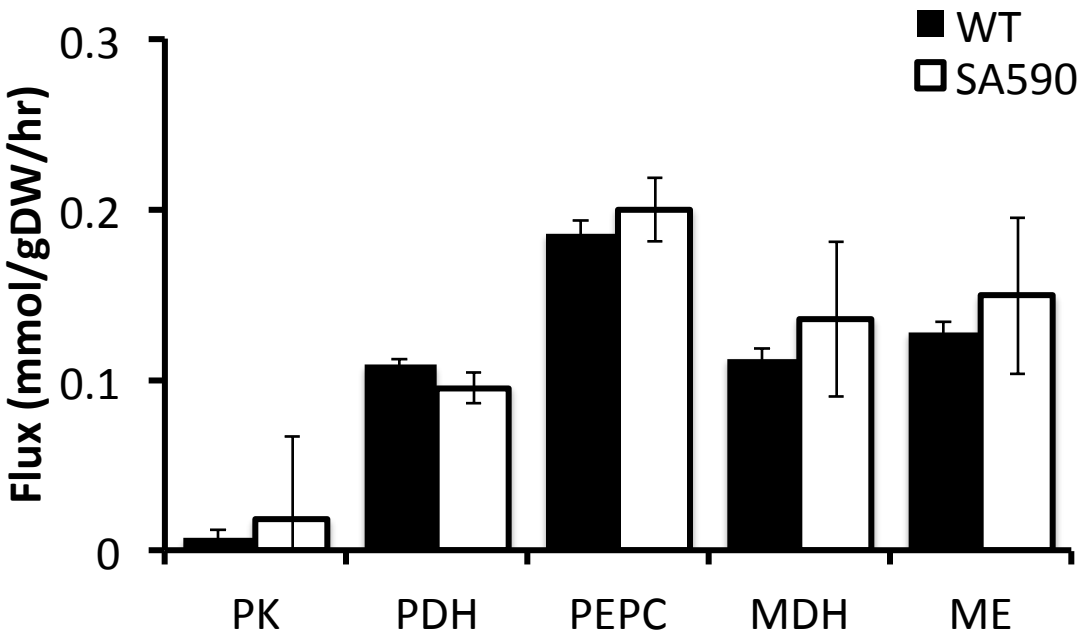

Figure 3.3. Intracellular fluxes in WT and SA590 at the pyruvate node.

A comparison of the pyruvate kinase (PK), pyruvate dehydrogenase (PDH), PEP carboxylase (PEPC), malate dehydrogenase (MDH), and malic enzyme (ME) fluxes as determined by INST-MFA. Error bars represent 95% confidence intervals on the flux estimates, and the plotted values represent the medians of the confidence intervals.

The flux analysis highlighted a natural metabolic route within cyanobacterial central carbon metabolism to bypass pyruvate kinase (PK) in both WT and IBA strains. PK catalyzes the glycolytic conversion of phosphoenolpyruvate (PEP) to pyruvate. High levels of ATP, produced in abundance during photosynthesis, have been found to inhibit PK activity [101]. The proposed PK bypass involves carbon being routed sequentially through PEPC, MDH, and ME (Figure 3.2). The flux analyses of both the WT and SA590 strains indicate that the majority of PEP flux was directed through PEPC rather than PK (Figure 3A.1). This finding reveals a major alternative route for pyruvate formation and

suggests that flux to pyruvate through PK is inhibited during photoautotrophic growth of *Synechococcus*, as has been previously suggested for *Synechocystis* [6]. Because pyruvate supplies carbon for IBA production in SA590, we hypothesized that overexpressing PK would relieve this metabolic bottleneck and increase flux towards IBA. Simultaneously, we overexpressed all three genes involved in the PK bypass pathway, both individually and in combination, to determine if IBA production could be increased by forcing more flux through this alternative pathway to pyruvate.

3.4.3 SINGLE GENE OVEREXPRESSION STRAINS

Based on the INST-MFA results, we generated the following single-gene overexpression strains to enhance flux toward pyruvate in the SA590 parent: SA590-PK, SA590-PEPC, SA590-MDH, and SA590-ME. The SA590-PEPC and SA590-ME strains exhibited significantly slower growth in comparison to the parental strain (Figure 3.4).

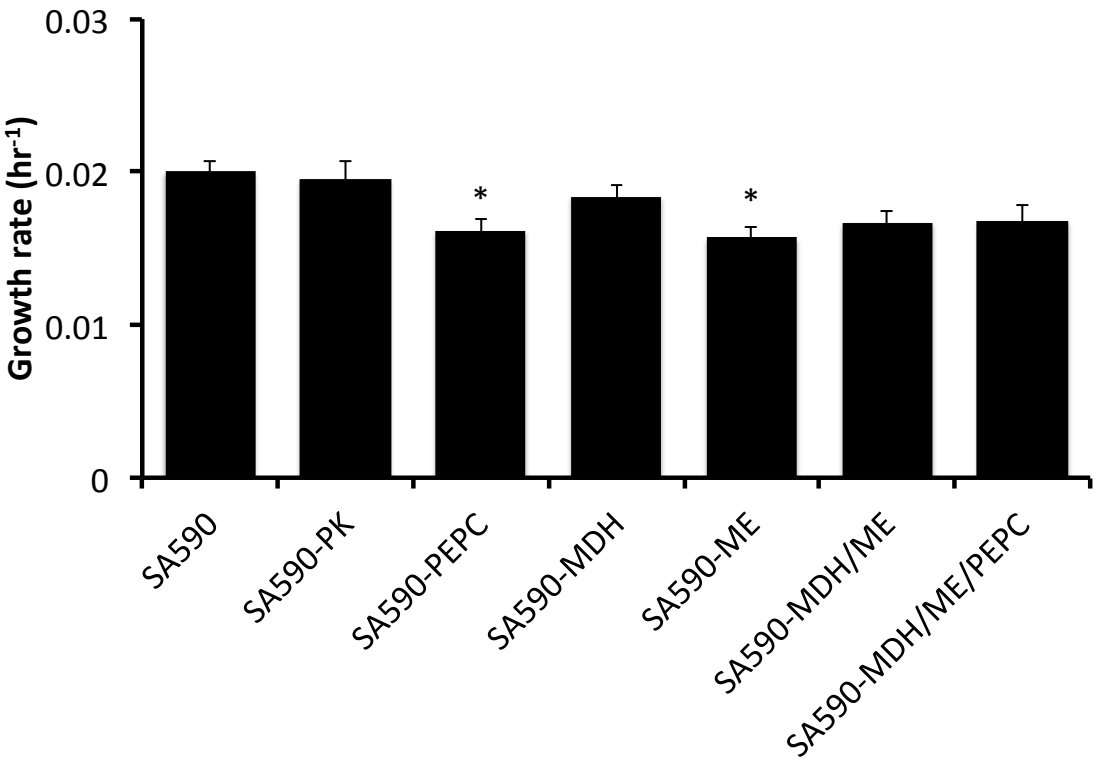

Figure 3.4. Effect of strain engineering on growth.

Growth was calculated by measuring optical density at the start (t=6hr) and end (t=30hr) of the capped flask aldehyde collection experiments. The parental IBA strain served as control. Dunnett's test was used to calculate significant differences. Data ± SE, n=3. *$p<0.05$.

Figure 3.5 shows a comparison in the combined aldehyde specific productivity (IBA + IVA) of the IBA-producing strains. On average, IVA productivity in all strains was approximately 10-13% of the total aldehyde productivity. While there was no significant difference in aldehyde production among the single-gene overexpressing strains as tested by ANOVA, all showed significant increases in specific productivity compared to SA590. Interestingly, the IBA-PK strain showed the greatest increase in aldehyde production when compared to the parental IBA strain.

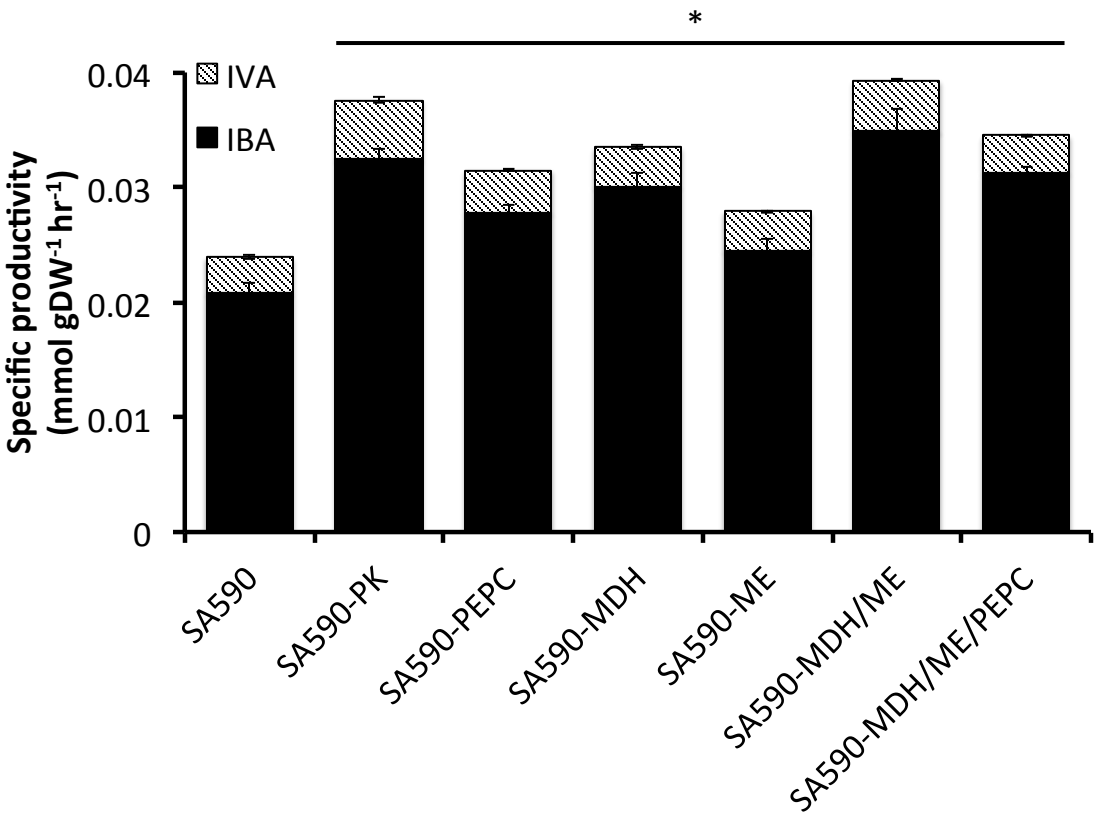

Figure 3.5. Effect of enzyme overexpression on aldehyde production.

Aldehyde specific productivity was calculated by measuring aldehyde concentration and cell density at the start (t=6hr) and end (t=30hr) of the capped flask collection experiments. These values were regressed using the ETA software package to determine specific rates [97]. The parental SA590 strain served as control. Dunnett's test was used to calculate significant differences. Data ± SE, n=3. *$p<0.05$.

3.4.4 DOUBLE AND TRIPLE GENE OVEREXPRESSION STRAINS

Given the increased productivities observed in the single-gene overexpression strains, we hypothesized that the creation of double- or triple-gene overexpression strains could potentially push more flux towards aldehyde production by increasing flux through the PK bypass pathway. We chose to overexpress MDH in combination with ME for the

double-overexpression strain (SA590-MDH/ME) because intermediate pool size measurements showed that MDH overexpression led to malate accumulation while ME overexpression resulted in malate depletion (Figure 3.6). Therefore, we hypothesized that overexpressing both MDH and ME simultaneously would balance flux through the PK bypass and restore malate to homeostatic levels. A triple overexpression strain (SA590-PEPC/MDH/ME) was also generated and tested in parallel to determine whether overexpressing all three PK bypass genes together would result in even further increases in aldehyde specific productivity.

The growth data showed that both SA590-MDH/ME and SA590-PEPC/MDH/ME had similar growth rates to one another and trended towards slower growth in comparison to the parental SA590 strain (Figure 3.4). The aldehyde specific productivity data showed that both the double and triple overexpression strains had increased production rates in comparison to the parental strain (Figure 3.5). Interestingly, the double overexpression strain had higher IBA productivity than the triple overexpression strain and had a slightly higher production rate than the IBA-PYK single overexpression strain.

3.4.5 POOL SIZE MEASUREMENTS

In addition to characterizing the growth and aldehyde production rates of the engineered strains, we also applied targeted metabolite pool size measurements in the engineered strains. Figure 3.6 shows the pool sizes of four metabolites, each normalized to OD_{750} at t=30hr and an internal standard, norvaline. The values shown are all expressed relative to

the pool sizes of the WT strain. For the parental SA590 and single-gene overexpression strains, we were able to quantify the pyruvate, alanine, succinate and malate pool sizes. For the double and triple overexpression strains, pyruvate was not quantifiable because the chromatographic peak was below the noise threshold of the GC-MS. While the malate pool size showed significant variation among the single-gene overexpression strains, the double and triple overexpression strains exhibited malate concentrations that were similar to SA590. This implies that enzymes within the PK bypass pathway should be overexpressed in combination to achieve balanced flux to pyruvate.

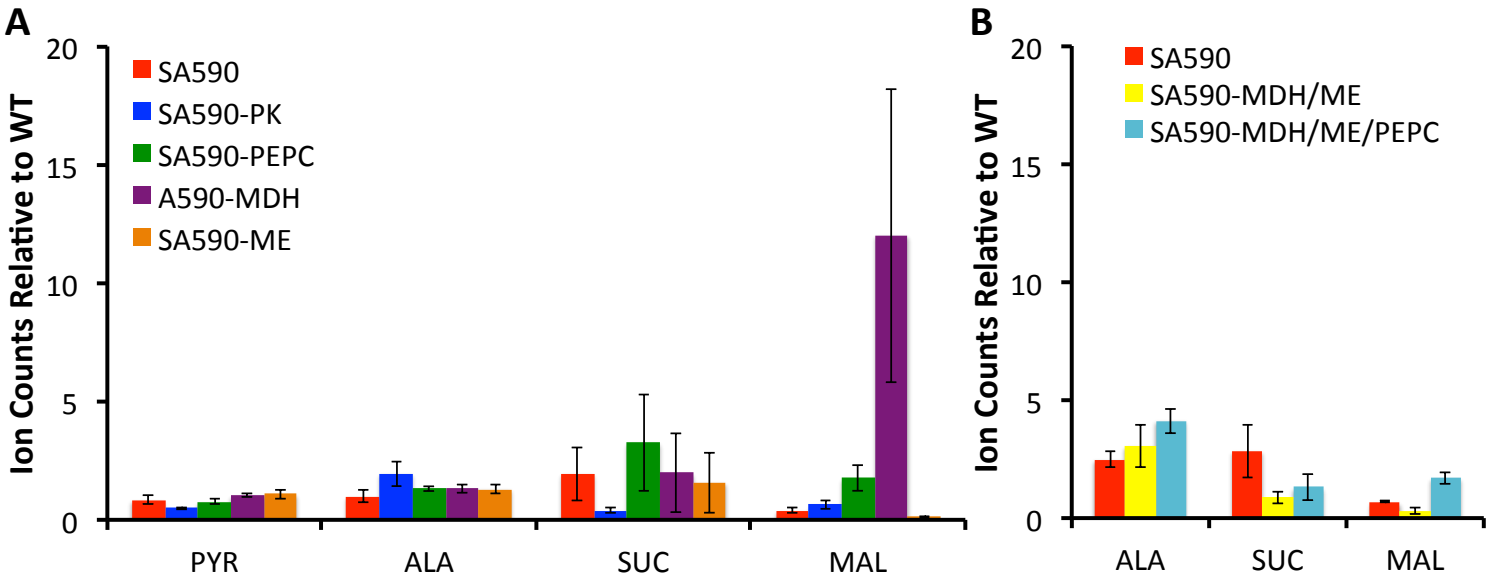

Figure 3.6. Intracellular pool sizes of pyruvate and related metabolites.

The GC-MS ion counts of central carbon intermediates. Metabolites were extracted and derivatized by MOX/TMS. Ion counts were normalized to an internal standard (norvaline) peak and to optical density (OD_{750}) at time of sample measurement (t=30). Values are shown relative to WT (=1). Data ± SE, n=4.

3.5 DISCUSSION

Production of chemicals and fuels from CO_2 is advantageous for reducing carbon emissions, as well as reducing reliance on petroleum. In this study, we applied INST-MFA to provide a direct readout of *in vivo* metabolic pathway activity in cyanobacteria that have been engineered to produce the chemical isobutyraldehyde under photoautotrophic conditions. The analysis revealed a substantial flux of PEP-derived carbon directed through PEPC rather than PK in both the WT and SA590 strains. This result is similar to the INST-MFA results in *Synechocystis* [6], where a natural PK bypass was observed in which carbon was channeled from PEP into pyruvate. The proposed PK bypass pathway converted carbon indirectly from PEP to pyruvate through reactions catalyzed by PEPC, MDH, and ME (Figure 3.2). In the previous INST-MFA study performed by Young et al. [6], the results showed approximately 49% of the flux emanating from PEP went through PEPC, as opposed to 40% through PK (the remaining 11% went towards biomass production). In this study, we found that carbon flux through PEPC was significantly greater than flux through PK (86% vs 3% for the WT strain and 84% vs 8% for the SA590).

Previous studies have suggested that malic enzyme could be involved in a carbon concentrating mechanism that is similar to that found in C4 plants [54]. Additionally, previous studies have shown that knockout of ME significantly reduced growth in *Synechocystis* under both autotrophic and mixotrophic conditions, while growth could be recovered by providing exogenous pyruvate [102,103]. Therefore, it has been suggested that high flux through ME may serve as a key route for pyruvate synthesis when PK

activity is down-regulated due to reduced ADP/ATP ratios in the light. As a whole, the high flux in the proposed PK bypass pathway suggested to us that there was a potential bottleneck in the conversion of PEP to pyruvate. We therefore hypothesized that flux to pyruvate—and subsequently to IBA—could be increased by overexpressing PK or, alternatively, key enzymes in the PK bypass pathway.

While all three of the PK bypass single-gene overexpression strains (SA590-PEPC, SA590-MDH, and SA590-ME) showed significant increases in aldehyde productivity in comparison to the parental SA590 strain, the SA590-PK strain showed the greatest increase in specific productivity (56% improvement) when using a closed flask system to capture the aldehyde products (Figure 3.5). However, preliminary data on aldehyde productivity obtained in an open flask cold-trap system (Figure 3A.2; [104]) showed only the SA590-ME strain had increased IBA productivity. Although the results from these two studies differ, the data generated are not necessarily contradictory. It is possible that the closed flask system limited the amount of CO_2 available to the cells or led to more dramatic increases in pH over time, which would further reduce the availability of dissolved CO_2 in the medium. A study by Schwarz et al. [105] investigated the metabolic and transcriptomic effects of acclimating *S. elongatus* PCC 7942 from high to low carbon conditions. In this study, they found that limiting available carbon to the cyanobacterial cells decreased levels of malate and fumarate, while increasing levels of PEP. These changes in pool sizes could potentially account for the differences in performance between the open and closed flask systems. A shift in dCO_2 could have altered the availability of substrates for the PK and ME reactions and thus biased the assessment of

aldehyde productivity in the engineered strains. One previous study showed that a 50 mM $NaHCO_3$ spike was sufficient to produce isobutanol for 6 days in a closed flask culture of *Synechocystis* [92]. However, we are currently evaluating whether changes in pH and dCO_2 could confound measurements of IBA productivity in the closed flask system.

Under the closed flask system, both double overexpression of MDH/ME and triple overexpression of PEPC/MDH/ME showed significant increases in aldehyde productivity when compared to the parental SA590 strain. The double overexpression strain had slightly higher aldehyde productivity than the SA590-PK strain. These data suggest that the majority of flux control within the PK bypass pathway is distributed between the MDH and ME reaction steps, while PEPC does not represent a significant bottleneck. Even though both the SA590-PK and SA590-MDH-ME strains showed similar aldehyde productivities, the PK overexpressing strain showed slightly better growth, possibly due to the reduced metabolic burden of amplifying expression of one gene instead of two.

Preliminary pool size measurements using an open flask system were generated for the WT and engineered strains. The SA590-MDH strain showed a significant increase in malate pool size, while the SA590-ME strain showed a significant decrease in malate. Interestingly, out of the three strains with single-gene overexpression of PK bypass enzymes, SA590-MDH showed the largest increase in aldehyde specific productivity using the closed flask collection system, while SA590-ME showed the largest increase in the open flask system. Future studies will re-examine these pool size measurements in the

closed flask system to determine if carbon-limiting conditions might have played a role in shifting the availability of substrates for the PK bypass reactions. Overall, this dataset shows the potential usefulness of combined MFA and pool size measurements to provide complementary tools for optimizing product formation in engineered host strains.

This study provides an illustrative example of how flux analysis can be applied to close the 'design-build-test-learn' metabolic engineering cycle, thereby guiding further rounds of strain improvement. Flux analysis was useful in identifying potential targets to debottleneck flux towards aldehyde production. These targets were overexpressed in the parental SA590 strain, and further characterization of growth and aldehyde specific productivity showed that the SA590-PK and SA590-MDH-ME strains had the greatest increases in aldehyde production. Further flux analysis studies should be performed on these two strains to quantify changes in metabolic flux and to determine if these overexpressions unexpectedly affected other pathways of central carbon metabolism. In addition, future studies could examine additional engineering targets, such as knocking down pyruvate dehydrogenase to shunt more carbon flux towards aldehyde production. Efforts to limit IVA production will also be beneficial to increase carbon flux towards IBA as the sole aldehyde product.

3.6 ACKNOWLEDGEMENTS

This work was supported by the following grants: GAANN (P200A090323), DOE (DE-AC05-06OR23100), and DOE (DE-SC008118). I am grateful for the help and contributions of Adeola Adebiyi, Yao Xu, and Peijun Ma to this work.

3.7 APPENDIX: SUPPLEMENTAL FIGURES AND TABLES

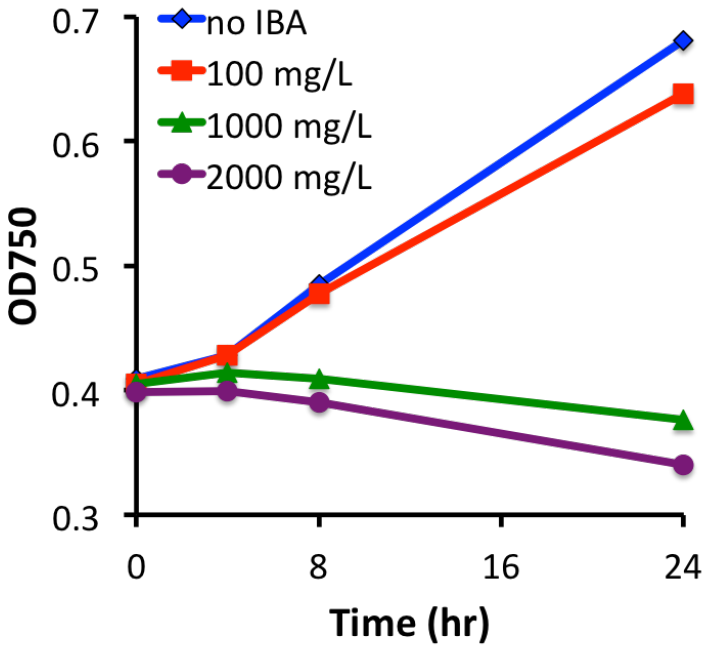

Figure 3A.1. *S. elongatus* tolerance to isobutyraldehyde.

Effect of IBA addition on growing cultures of *S. elongatus* as determined by optical density (OD_{750}). At OD_{750} ~0.4, IBA was added to the cultures to final concentrations of: 0, 100, 1000, and 2000 mg/L.

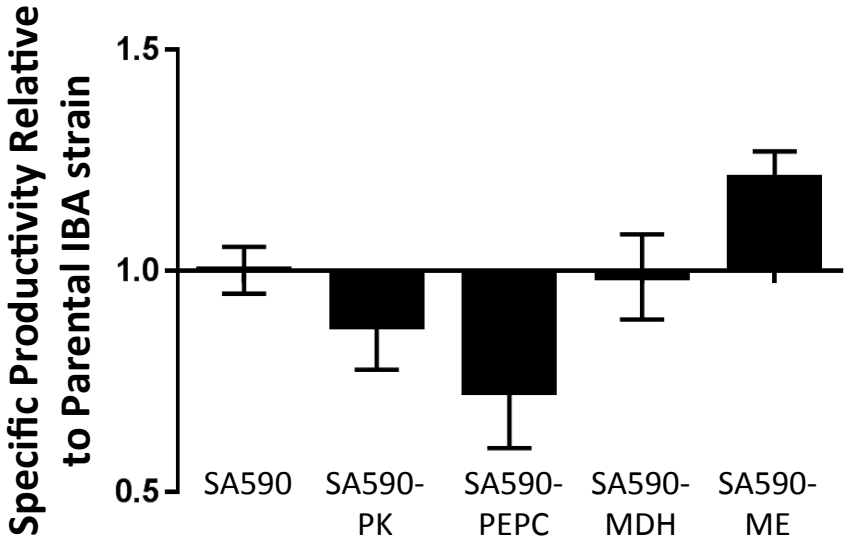

Figure 3A.2. Effect of enzyme overexpression on aldehyde production using an open flask and cold trap collection system.

These data were generated by Adebiyi [104]. IBA and IVA were captured for 24 hours, 6 hours after induction of aldehyde production with IPTG. The total aldehyde productivity from each flask was normalized to the average productivity of the parental SA590 strain. Data ± SE; n ≥6.

Table 3A.1. Complete list of reactions and atom transitions for *Synechococcus elongatus* PCC 7942 metabolic network.

Enzymatic Reactions for *S. elongatus* PCC 7942 metabolic network			
RUBISCO_CO2	RUBP (abcde) + CO2 (f)	→	3PGA (cde) + 3PGA (fba)
GAPDH	3PGA (abc)	→	TP (abc)
ALD	TP (abc) + E4P (defg)	→	SBP (cbadefg)
SBP	SBP (abcdefg)	→	S7P (abcdefg)
FBA	TP (def) + TP (cba)	↔	FBP (abcdef)
PFK	FBP (abcdef)	↔	F6P (abcdef)
TK1	TP (cde) + EC2 (ab)	↔	X5P (abcde)
TK2	S7P (abcdefg)	↔	R5P (cdefg) + EC2 (ab)
TK3	F6P (abcdef)	↔	E4P (cdef) + EC2 (ab)
PPE	X5P (abcde)	↔	RU5P (abcde)
PPI	R5P (abcde)	↔	RU5P (abcde)
PRK	RU5P (abcde)	→	RUBP (abcde)
PGI	F6P (abcdef)	↔	G6P (abcdef)
PGM	G6P (abcdef)	↔	G1P (abcdef)
GS	G1P (abcdef)	↔	GLYC (abcdef)
G6PDH	G6P (abcdef)	→	RU5P (bcdef) + CO2 (a)
RUBISCO_O2	RUBP (abcde)	→	3PGA (cde) + 2PG (ba)
PGP	2PG (ab)	→	GLY (ab)
GDC	GLY (ab) + GLY (cd)	→	SER (cdb) + CO2 (a)
SGA	SER (abc)	→	GA (abc)
GK	GA (abc)	↔	3PGA (abc)
ENO	3PGA (abc)	↔	PEP (abc)
PK	PEP (abc)	→	PYR (abc)
ALT	PYR (abc)	↔	ALA (abc)
ALS	PYR (abc) + PYR (def)	→	AcLAC (abcde) + CO2 (f)
KIV1	AcLAC (abcde)	→	IBA (abcd) + CO2 (e)
KIV2	AcLAC (abcde)	→	IVA (abcde)
PDH	PYR (abc)	→	ACA (bc) + CO2 (a)
CS	OAA (abcd) + ACA (ef)	→	CIT (dcbfea)
ACO	CIT (abcdef)	↔	ICI (abcdef)
IDH	ICI (abcdef)	→	AKG (abcde) + CO2 (f)
SDH	SUC (abcd)	↔	FUM (abcd)
FUM	FUM (abcd)	↔	MAL (abcd)
MDH	MAL (abcd)	↔	OAA (abcd)
ME	MAL (abcd)	→	PYR (abc) + CO2 (d)
PPC	PEP (abc) + CO2 (d)	→	OAA (abcd)

Table 3A.1. Continued.

Growth	0.715*R5P + 3.624*ACA + 1.191*G6P + 0.501*E4P + 1.205*3PGA + 1.002*PEP + 1.197*PYR + 2.039*OAA (abcd) + 1.233*AKG + 0.133*TP + 1.017*CO2	→	Biomass + 0.683*FUM (abcd)

Table 3A.2. Net fluxes determined by ^{13}C INST-MFA in WT and SA590.

Estimated flux values (mmol/gDW/hr) and 95% confidence bounds are shown (n=3).

	WT			SA590		
Reaction	**Value**	LB95	UB95	**Value**	LB95	UB95
RUBP + CO2 → 3PGA + 3PGA	**1.019**	0.950	1.089	**1.040**	0.873	1.207
3PGA → TP	**1.796**	1.676	1.955	**1.821**	1.526	2.144
TP + E4P → SBP	**0.341**	0.318	0.373	**0.349**	0.292	0.411
SBP → S7P	**0.341**	0.318	0.373	**0.349**	0.292	0.411
TP + TP ↔ FBP	**0.379**	0.353	0.412	**0.382**	0.319	0.448
FBP ↔ F6P	**0.379**	0.353	0.412	**0.382**	0.319	0.448
TP + EC2 ↔ X5P	**0.694**	0.647	0.757	**0.707**	0.593	0.834
S7P ↔ R5P + EC2	**0.341**	0.318	0.373	**0.349**	0.292	0.411
F6P ↔ E4P + EC2	**0.353**	0.328	0.384	**0.358**	0.300	0.422
X5P ↔ RU5P	**0.694**	0.647	0.757	**0.707**	0.593	0.834
R5P ↔ RU5P	**0.325**	0.303	0.356	**0.335**	0.281	0.395
RU5P → RUBP	**1.019**	0.951	1.113	**1.041**	0.874	1.230
F6P ↔ G6P	**0.027**	0.025	0.043	**0.023**	0.019	0.063
G6P ↔ G1P	**0.000**	0.000	0.000	**0.000**	0.000	0.000
G1P ↔ GLYC	**0.000**	0.000	0.000	**0.000**	0.000	0.000
G6P → RU5P + CO2	**0.000**	0.000	0.016	**0.000**	0.000	0.039
RUBP → 3PGA + 2PG	**0.000**	0.000	0.051	**0.001**	0.001	0.082
2PG → GLY	**0.000**	0.000	0.051	**0.001**	0.001	0.082
GLY + GLY → SER + CO2	**0.000**	0.000	0.025	**0.001**	0.000	0.041
SER → GA	**0.000**	0.000	0.025	**0.001**	0.000	0.041
GA ↔ 3PGA	**0.000**	0.000	0.025	**0.001**	0.000	0.041
3PGA ↔ PEP	**0.215**	0.201	0.230	**0.237**	0.202	0.273
PEP → PYR	**0.007**	0.001	0.016	**0.018**	0.000	0.190
PYR ↔ ALA	**0.000**	0.000	0.000	**0.000**	0.000	0.000
PYR + PYR → AcLAC + CO2	**0.000**	0.000	0.000	**0.024**	0.022	0.026
AcLAC → IBA + CO2	**0.000**	0.000	0.000	**0.021**	0.019	0.023
AcLAC → IVA	**0.000**	0.000	0.000	**0.003**	0.003	0.003
PYR → ACA + CO2	**0.108**	0.101	0.116	**0.095**	0.078	0.113
OAA + ACA → CIT	**0.028**	0.026	0.029	**0.024**	0.020	0.029
CIT ↔ ICI	**0.028**	0.026	0.029	**0.024**	0.020	0.029
ICI → AKG + CO2	**0.028**	0.026	0.029	**0.024**	0.020	0.029
SUC ↔ FUM	**0.000**	0.000	0.000	**0.000**	0.000	0.000
FUM ↔ MAL	**0.015**	0.014	0.016	**0.013**	0.011	0.016
MAL ↔ OAA	**0.112**	0.101	0.123	**0.135**	-0.016	0.163
MAL → PYR + CO2	**0.128**	0.116	0.139	**0.149**	0.000	0.178
PEP + CO2 → OAA	**0.185**	0.171	0.200	**0.200**	0.164	0.236

Table 3A.2. Continued.

0.715*R5P + 3.624*ACA + 1.191*G6P + 0.501*E4P + 1.205*3PGA + 1.002*PEP + 1.197*PYR + 2.039*OAA + 1.233*AKG + 0.133*TP + 1.017*CO2 → Biomass + 0.683*FUM	**0.022**	0.021	0.024	**0.020**	0.016	0.023

Table 3A.3. Exchange fluxes determined by ^{13}C INST-MFA for WT and SA590.

The exchange flux is the minimum of the forward and backward fluxes of a reversible reation. Estimated flux values (mmol/gDW/hr) and 95% confidence bounds are shown (n-=3).

	WT			SA590		
Reaction	**Value**	LB95	UB95	**Value**	LB95	UB95
TP + TP ↔ FBP	**Unidentifiable**	0.000	Inf	**Unidentifiable**	0.000	Inf
FBP ↔ F6P	**Unidentifiable**	0.000	Inf	**Unidentifiable**	0.000	Inf
TP + EC2 ↔ X5P	**Unidentifiable**	0.000	Inf	**0.702**	0.000	2.571
S7P ↔ R5P + EC2	**Unidentifiable**	0.000	Inf	**Unidentifiable**	0.000	Inf
F6P ↔ E4P + EC2	**Unidentifiable**	0.000	Inf	**Unidentifiable**	0.000	Inf
X5P ↔ RU5P	**Unidentifiable**	0.000	Inf	**0.000**	0.000	0.233
R5P ↔ RU5P	**Unidentifiable**	0.000	Inf	**Unidentifiable**	0.000	Inf
F6P ↔ G6P	**0.027**	0.000	0.118	**0.000**	0.000	0.015
G6P ↔ G1P	**0.468**	0.061	Inf	**Unidentifiable**	0.065	Inf
G1P ↔ GLYC	**Unidentifiable**	0.000	Inf	**Unidentifiable**	0.065	Inf
GA ↔ 3PGA	**0.304**	0.129	0.451	**0.000**	0.000	0.007
3PGA ↔ PEP	**Unidentifiable**	0.000	Inf	**Unidentifiable**	0.000	Inf
PYR ↔ ALA	**3.224**	1.570	13.635	**Unidentifiable**	0.000	Inf
CIT ↔ ICI	**Unidentifiable**	0.000	Inf	**0.658**	0.143	1.282
SUC ↔ FUM	**3.229**	2.100	7.255	**1.287**	0.831	2.801
FUM ↔ MAL	**4.858**	2.706	17.451	**0.765**	0.497	1.692
MAL ↔ OAA	**27642**	7.966	Inf	**Unidentifiable**	0.000	Inf

Table 3A.4. Pool sizes determined by ^{13}C INST-MFA for WT and SA590.

nmol/gDW	WT		SA590	
Pool	LB95	UB95	LB95	UB95
2PG	0.0	9.6	0.0	0.6
3PGA	0.0	9.6	0.0	2.4
ACA	116.2	Inf	0.0	64.8
AKG	0.0	0.3	0.0	0.7
ALA	0.0	2.9	0.0	11.9
AcLAC	0.0	Inf	0.0	Inf
CIT	0.0	0.2	0.0	8.1
CO2	0.0	1.3	6.1	16.6
E4P	0.0	7.8	0.0	0.7
F6P	0.0	3.0	0.0	0.7
FBP	0.0	3.0	0.0	1.5
FUM	0.0	7.9	0.0	10.8
G1P	0.0	Inf	0.0	Inf
G6P	0.0	13.3	0.0	3.3
GA	163.9	737.3	0.0	0.1
GLY	0.0	24.3	0.1	11.6
GLYC	0.0	Inf	0.0	Inf
IBA	0.0	Inf	0.0	Inf
ICI	0.0	0.3	27.2	190.3
IVA	0.0	0.0	0.0	Inf
MAL	0.0	4.3	0.0	2.9
OAA	0.0	4.3	0.0	1.4
PEP	0.0	0.0	0.0	0.0
PEP	19.3	42.6	0.0	2.4
PYR	0.0	2.9	0.0	11.9
R5P	0.0	1.8	0.0	1.1
RU5P	0.0	1.8	0.0	1.1
RUBP	0.0	1.8	0.0	1.1
S7P	0.0	1.2	0.0	1.1
SBP	0.0	0.8	0.0	0.4
SER	0.0	0.3	0.3	Inf
SUC	287.5	375.4	203.4	484.1
TP	0.0	3.7	0.0	2.9
X5P	0.0	3.4	14.2	26.2

4. ISOTOPICALLY NONSTATIONARY 13C FLUX ANALYSIS OF CHANGES IN *ARABIDOPSIS THALIANA* LEAF METABOLISM DUE TO HIGH LIGHT ACCUMULATION

Proceedings of the National Academy of Sciences (2014). 111:16967-16972.

4.1 ABSTRACT

Improving plant productivity is an important aim for metabolic engineering. There are few comprehensive methods that quantitatively describe leaf metabolism, though such information would be valuable for increasing photosynthetic capacity, enhancing biomass production, and rerouting carbon flux toward desirable end products. Isotopically nonstationary metabolic flux analysis (INST-MFA) has been previously applied to map carbon fluxes in photoautotrophic bacteria, which involves model-based regression of transient ^{13}C-labeling patterns of intracellular metabolites. However, experimental and computational difficulties have hindered its application to terrestrial plant systems. We performed *in vivo* isotopic labeling of *Arabidopsis thaliana* rosettes with $^{13}CO_2$ and estimated fluxes throughout leaf photosynthetic metabolism by INST-MFA. Leaves were acclimated to either 200 or 500 μmol $m^{-2}s^{-1}$ light. Approximately 1,400 independent mass isotopomer measurements obtained from analysis of 37 metabolite fragment ions were regressed to estimate 136 fluxes under each condition. The results provide a comprehensive description of changes in carbon partitioning and overall photosynthetic flux in response to high-light acclimation of leaves. Despite a doubling in the

carboxylation rate, the photorespiratory flux increased from 17% to 28% of net CO_2 assimilation with high-light acclimation (Vc/Vo: 3.5:1 vs. 2.3:1, respectively) and was independently validated by ^{14}C-labeling. The concentrations of multiple Calvin cycle intermediates were reduced during acclimation, indicating an inverse relationship between intermediate pool sizes and fluxes. This study highlights the potential of ^{13}C INST-MFA to describe emergent flux phenotypes that respond to environmental conditions or plant physiology and cannot be obtained by other complementary approaches.

4.2 INTRODUCTION

Photosynthetic organisms assimilate over 100 billion tons of carbon, approximately 15% of the atmospheric total, each year and generate organic compounds for food and renewable chemicals [106]. However, photosynthesis is a complex process that responds to heterotrophic tissue demands and environmental stimuli such as drought, temperature, and light intensity [107,108]. The light incident on the plant varies with intensities in the range of 0-2000 μmol photons m^{-2} s^{-1} and can change dramatically due to passing clouds, shading, and the position of the sun. Thus, plants adjust light harvesting and carbon assimilation steps to accommodate many fluctuations, resulting in changes in plant morphology, physiology, and metabolism [109].

For ninety-five percent of all terrestrial plants (i.e., C3 plants), the reductive pentose phosphate (Calvin-Benson-Bassham, or CBB) cycle directly links light and dark

reactions and sustains anabolic activities [110]. RuBisCO (Ribulose-1,5-bisphosphate carboxylase oxygenase) plays a central role in the cycle by carboxylating ribulose-1,5-bisphosphate (RUBP) with CO_2 to form two 3-phosphoglycerate (3PGA) molecules. The other 10 enzymes in the CBB cycle regenerate the RUBP substrate to repeat this process. RuBisCO has a low turnover rate [~3/s; [111]] and also performs a competitive oxygenation side reaction that limits carboxylation activity. The binding of RuBisCO to oxygen produces 2-phosphoglycolate (2PG), and additional enzymatic steps, known collectively as photorespiration, are required to convert 2PG into 3PGA. Rectifying the oxygenase-based production of 2PG, that would otherwise be toxic, requires CO_2 release and consumes energy through photorespiration, thereby expending up to 50% of all fixed carbon [112] to maintain plant health [113]. Researchers have attempted to augment RuBisCO's specificity and throughput [114], introduce non-native forms of RuBisCO [111], increase the regenerative capacity of the CBB cycle [115,116], and minimize metabolic costs associated with photorespiration [117]. These studies produced mixed results, thus advocating for a more comprehensive, systems-level approach to enhance and/or redirect photosynthetic carbon flux.

In silico methods including kinetic [118] and stoichiometric [119–121] models can simulate metabolic network behavior and improve our mechanistic understanding of photosynthetic metabolism, but the predictions must be experimentally verified by other methods [122]. We and others have used metabolic flux analysis (MFA) based on steady-state ^{13}C labeling studies to map the flow of carbon through the biochemical pathways of plant seeds [123–126] or cultured plant cells [82,127], which exhibit extended periods of

pseudo-steady-state metabolism. However, leaves exhibit diurnal patterns of metabolism with limited metabolic steady states [128,129]. Furthermore, autotrophic tissues produce uniform steady-state ^{13}C-labeling patterns that are largely uninformative [5]. Therefore, transient $^{13}CO_2$ labeling studies are necessary to quantify leaf metabolic fluxes.

A prior $^{13}CO_2$ labeling study by Szecowka *et al.* [130] applied kinetic flux profiling (KFP) to estimate net carbon fixation and photorespiration fluxes along with biosynthetic fluxes leading to sucrose, starch, trehalose, and myo-inositol in *Arabidopsis* rosettes under a single condition with illumination at 120 μmol m^{-2} s^{-1}. The KFP approach [12] uses a differential equation model to regress the trajectories of unlabeled mass isotopomer abundances (M0) and intracellular pool size measurements obtained for multiple ^{13}C-labeled metabolites, but without accounting for the distribution of higher mass isotopomers (M1, M2, etc.) observed. In contrast, isotopically nonstationary MFA (INST-MFA) is able to describe the full mass isotopomer distributions (MIDs) of measured metabolites, and is therefore capable of distinguishing flux contributions from different metabolic pathways based on the atomic rearrangements they produce. This provides enhanced flux resolution and does not require direct pool size measurements.

Previously, Young *et al.* applied ^{13}C INST-MFA to map 76 fluxes within the central carbon metabolism of the cyanobacterium *Synechocystis* sp. PCC 6803 [6]. The flux analysis revealed unanticipated photosynthetic inefficiencies tied to oxidative metabolic pathways, despite minimal photorespiration. In this study, we applied a similar modeling

approach to map autotrophic metabolism of *Arabidopsis* rosettes under varying light intensities. The Allen lab at the Donald Danforth Plant Science Center in St. Louis, MO grew the rosettes involved in this study, performed the labeling experiments by administering $^{13}CO_2$ to whole plants, and measured labeling using LC-MS/MS and GC-MS. I integrated and analyzed the MS data generated and carried out the ^{13}C INST-MFA. ^{13}C INST-MFA was applied to determine i) network-wide flux estimates from isotopomer labeling for both low light (LL) and high light acclimated (HL-ACC) *Arabidopsis* plants, including photorespiratory fluxes that were further validated by independent radiolabeling measurements; ii) a compartmentalized description of sucrose and starch biosynthesis; iii) a description of leaf export of sucrose and amino acids consistent with measurements of vascular exudates; and iv) model-based estimates of inactive pools consistent with cellular and subcellular leaf heterogeneity. The models were validated through benchmarking fluxes with the literature and by independent experiments not used for model identification. This study reveals the potential for ^{13}C INST-MFA to provide novel insights into photosynthetic metabolism that can guide plant metabolic engineering.

4.3 METHODS

4.3.1 PLANT GROWTH CHARACTERISTICS

Wild-type *Arabidopsis thaliana* ecotype Col-0 plants were grown in a Conviron growth chamber (model MTPS 120-2, Pembina, ND) under 16/8-hr day/night cycles, temperature of 22/18°C, light intensity of 200 μmol m^{-2} s^{-1}, and 50% relative humidity. At 24 days of age, plants were transferred to a Percival incubator (model E22L, Perry, IA) that was set up with identical incubation conditions, where plants were maintained for three days prior to isotopic labeling (LL). For the high light acclimation process, plants initially grown to 17 days of age at 200 μmol m^{-2} s^{-1} were exposed to 500 μmol m^{-2} s^{-1} for nine days prior to isotope labeling at 500 μmol m^{-2} s^{-1} (HL-ACC). In both cases, plants were labeled 28 days after planting when leaves were fully expanded. Pigments including chlorophyll were quantified spectroscopically, RuBisCO was quantified by western blot and gel image, sucrose was quantified by GC-MS, starch was quantified using an enzymatic assay (Megazyme, Wicklow, Ireland), leaf cross-sections and chloroplast ultrastructure were imaged in an energy filter transmission electron microscope (LEO 912 AB, LEO, Oberkochen, Germany), and oil was quantified by GC-FID (SI Materials and Methods).

4.3.2 GAS EXCHANGE AND $^{13}CO_2$ LABELING OF *ARABIDOPSIS* ROSETTES

A LI-6400 XT portable photosynthesis system (Li-Cor, Lincoln, NE) was used to monitor assimilation and light response of four-week-old plants. Isotopic labeling experiments ($n \geq 3$) were performed on plants acclimated to light intensities of 200 μmol m^{-2} s^{-1} (LL) or

500 μmol m^{-2} s^{-1} (HL-ACC). *Arabidopsis* rosettes were labeled in a Percival E22L incubator containing an inflated glove bag (Gas-Col) or custom-made individual gas-tight chambers, using premixed gas containing $^{13}CO_2$ (Sigma, St Louis, MO) at a $^{13}CO_2/N_2/O_2$ ratio of 0.033/78/21.967. Ten samples were collected over a 15-minute interval at the following time points: 30s, 60s, 90s, 120s, 150s, 180s, 300s, 420s, 600s, and 900s followed by immediate quenching with liquid nitrogen. In each case, liquid nitrogen was dumped directly on plants that were still in the incubator with care to avoid any shading. The liquid nitrogen resulted in some leaves falling off of the rosettes almost instantly (i.e., less than a second after the nitrogen was applied). Therefore, we expect that the quenching process was adequate.

4.3.3 LC-MS/MS AND GC-MS OF METABOLITE LABELING AND CONCENTRATION

Methods to extract metabolites were modified from Arrivault et al. [128]. Leaf tissue was extracted with methanol/chloroform/water (4ºC). Filtered samples were run on an AB Sciex QTRAP™ 4000 linked to a Shimadzu HPLC using negative ionization. Ion-pair chromatography (IPC) linked to tandem MS was performed as described in [6,128] with slight modifications. GC-MS was used to inspect labeling in amino and organic acids. The final parameters used for isotopomer measurements are listed in the Appendix.

4.3.4 ISOTOPOMER NETWORK AND FLUX DETERMINATION

An isotopomer model describing photosynthetic central carbon metabolism in *Arabidopsis* rosettes was constructed from reaction networks in biochemical literature. A

list of the reactions is provided in the Appendix. MFA was performed assuming intracellular metabolite levels and metabolic fluxes remained constant throughout the labeling experiment and were not perturbed by replacement of $^{12}CO_2$ with the same concentration of $^{13}CO_2$. MFA studies presume that the effect of carbon isotope fractionation is small. Even though different pathways of carbon fixation are known to exhibit varying levels of isotope fractionation (i.e., a preference for ^{12}C over ^{13}C or vice versa), these deviations are well below the levels that can be detected by the quadrupole MS instruments used in this study [9]. The enzyme-bound carbon fragment EC2 was present at infinitesimal concentrations and thus was in isotopic quasi-equilibrium with its metabolite precursors. E4P and SBP were treated similarly, since they could not be directly measured but were assumed to be small pools that equilibrate rapidly with their upstream precursors. Intermediates were in some cases less labeled than their downstream products, indicating the presence of spatial heterogeneity. Others have similarly noted the presence of inactive pools [130] and have also observed labeling patterns that indicate multiple pools that are spatially resolved and subject to different degrees of labeling. Rather than attempt to measure the pools by organelle fractionation, which can be compromised by organelle leakage and contamination, dilution parameters were introduced to describe the lack of equilibration between labeled (i.e., metabolically active) and unlabeled (i.e., metabolically inactive) pools of the same metabolite. These parameters are mathematically equivalent to the (1-*G*) parameters introduced by [131], which were later adopted by [6] and [132]to account for isotopic nonsteady state in isotopomer models of bacterial metabolism.

INST-MFA was used to estimate intracellular metabolic fluxes. Least-squares parameter regression, as well as statistical and sensitivity analysis of the optimal solution, was performed using the publically available software package Isotopomer Network Compartmental Analysis [INCA [24]], which runs within MATLAB™ [6,124]. INCA relies upon an elementary metabolite unit (EMU) decomposition of the underlying isotopomer network to efficiently simulate the effects of varying fluxes on the labeling trajectories of measurable metabolites. Metabolic fluxes and pool sizes were estimated by minimizing the lack-of-fit between experimentally measured and computationally simulated mass isotopomer distributions (MIDs) using a Levenberg-Marquardt optimization algorithm [20]. Flux evaluation was repeated a minimum of 50 times from random initial values to obtain best-fit estimates. All results were subjected to a chi-square statistical test to assess goodness-of-fit, and accurate 95% confidence intervals (CIs) were computed for all estimated parameters by evaluating the sensitivity of the sum-of-squared residuals (SSR) to parameter variations [34].

4.4 RESULTS

4.4.1 PLANT DEVELOPMENT AND PHOTOSYNTHETIC RATES

Developmental stages and photosynthetic metabolism are closely linked. Leaf morphology, pigmentation, photosynthetic rate, enzyme activities, and carbon partitioning impact plant development. In turn, the expansion of leaves, development of reproductive sink, and leaf senescence influence photosynthesis [133]. Leaves of three- to five-week-old *Arabidopsis* plants had comparable amounts of chlorophyll per unit leaf

fresh weight (FW) and net photosynthetic rates per unit leaf area; however, RuBisCO content per unit FW decreased with age (**Figure 4.1**), and five-week-old plants exhibited flower development. Fully expanded leaves of four-week-old plants were selected for all further experiments. Light-response curves (**Figure 4.1**) indicated that plants acclimated to high light have approximately 38±4% greater maximum photosynthetic rates than non-acclimated plants (measured at ~2000 μmol m-2 s-1) and an altered ratio of chlorophyll a/b (Figure 4A.1).

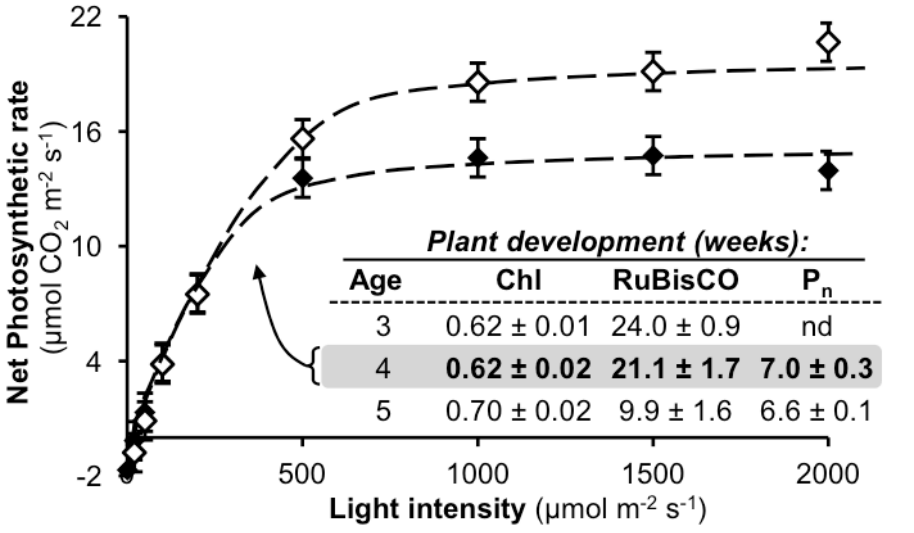

Figure 4.1. Net photosynthetic rate as a function of light intensity in four-week-old plants.

Plants were grown at light intensity of 200 μmol m^{-2} s^{-1} (black diamonds) or acclimated to 500 μmol m^{-2} s^{-1} for nine days (white diamonds) prior to measurement (SEM; n=4). (Table inset) Photosynthetic measurements of leaves of three- to five-week-old plants grown at 200 μmol m^{-2} s^{-1} including chlorophyll (Chl; mg gFW^{-1}; SEM, n=4), RuBisCO (mg gFW^{-1}; SEM, n=3) and net CO_2 assimilation rate (Pn; μmol CO_2 m^{-2} s^{-1}; SEM, n=6).

4.4.2 STARCH AND SUCROSE MEASUREMENTS

Starch and sucrose, two significant products of leaf photosynthetic metabolism, were quantified to determine the times during the day that leaves exhibit pseudo-steady-state metabolism. The amount of starch and sucrose per unit FW were measured hourly from morning to midday. The leaves produced starch at a rate of 6.3±0.3 μmol glucose gFW-1 hr-1 throughout the experimental time course (Figure 4A.1). The sucrose pool size did not change significantly during the same period of time, indicating that the biosynthetic and export rates were balanced. Therefore, plant leaves were isotopically labeled in the late morning.

4.4.3 ^{13}C-LABELING OF *ARABIDOPSIS* ROSETTES AT DIFFERENT LIGHT INTENSITIES

In order to map carbon fluxes after acclimation to varied light intensities, 3-6 replicate ^{13}C-labeling experiments were performed at low light (200 μmol m^{-2} s^{-1}; LL) or high light conditions after acclimation (500 μmol m^{-2} s^{-1}, 9-day acclimation; HL-ACC). Immediately after the introduction of ^{13}C-labeled CO_2, a time-series of leaf samples were collected and the mass spectra of 37 fragment ions from each of 10 time points were analyzed using LC-MS/MS and GC-MS. Raw measured isotopomer abundances can be found in the supplemental dataset of [23]. The average ^{13}C enrichment of most metabolites increased hyperbolically over time, with the MID shifting gradually toward heavier mass isotopomers (Figure 4.2, Figure 4A.2,Figure 4A.3). Intermediates involved in the CBB cycle, photorespiration, and sugar synthesis became enriched at a faster rate than organic and amino acids. Of the latter, only serine, glycine, alanine, and aspartate were significantly enriched during the initial 15-minute labeling period.

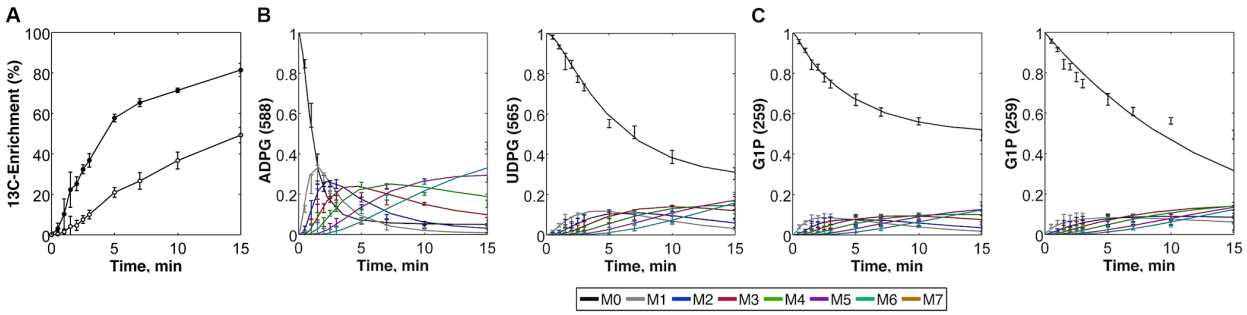

Figure 4.2. Transient ^{13}C-labeling in intracellular metabolites.

(A) Average ^{13}C-enrichments of ADP-glucose (ADPG; closed circles) and UDP-glucose (UDPG; open circles) under LL conditions calculated using the formula $\left(\frac{1}{N}\right)\sum_{i=1}^{N} \boldsymbol{Mi\ x\ i}$, where *N* is the number of carbon atoms in the metabolite and *Mi* is the fractional abundance of the *i*th mass isotopomer. The solid lines connecting average ^{13}C-enrichments were added to aid data visualization and do not represent model fits. (B) Experimentally measured mass isotopomer abundances (data points) and INST-MFA model fits (solid lines) of ADPG and UDPG under LL conditions. Error bars represent standard measurement errors (SEM, n=6). Mass isotopomer data corrected for natural isotope abundance are shown. Nominal masses of M0 mass isotopomers are shown in parentheses for ADPG and UDPG. (C) Experimentally measured MIDs and INST-MFA model fits of glucose-1-phosphate (G1P) with and without inclusion of dilution parameters to account for inactive pools. Cellular heterogeneity can result in inactive pools that are not significantly enriched within the time course of the experiment. The contribution of these pools to the measured MID can be accommodated by incorporating dilution parameters into the model.

4.4.4 ADPG AND UDPG REVEAL METABOLIC COMPARTMENTATION

The MIDs of ADP-glucose (ADPG) and UDP-glucose (UDPG), which are the respective precursors for starch and sucrose biosynthesis, were examined to assess subcellular compartmentation in central metabolic pathways. Initial tests indicated labeling only within the glucosyl component of the nucleotide phosphates; therefore, labeling was quantified only in this "metabolically active" component of ADPG and UDPG. Isotopic incorporation resulted in 81±3% enrichment of ADPG and 49±4% enrichment of UDPG at 15 minutes (Figure 4.2A). The labeling differences confirm that starch and sucrose are generated from precursors that originate within distinct subcellular locations (i.e., plastid and cytosol, respectively; Figure 4.2A, Figure 4.2B) and are consistent with current understanding of leaf carbon partitioning [134,135].

4.4.5 ISOTOPICALLY NONSTATIONARY METABOLIC FLUX ANALYSIS

A set of comprehensive isotopomer models were constructed to estimate metabolic fluxes based on the measured MIDs, the net CO_2 assimilation and starch production rates, and steady-state levels of sucrose and amino acids in vascular exudate (Figure 4.3). The reaction network and fluxes (Figure 4A.4, **Table 4A.5**) included the CBB cycle, photorespiration, a bifurcated TCA pathway, and pathways for starch, sucrose and amino acid biosynthesis [136]. Inclusion of inactive pools and subcellular compartmentation was required to pass the chi-square goodness-of-fit test and to describe the multicellular, heterogeneous anatomy of a leaf (Figure 4.2C). In general, the model-estimated sizes of inactive pools (expressed as a fraction of the total intracellular pool) were in qualitative agreement with M0 mass isotopomer abundances measured after a 60-min 13CO2-

labeling experiment (Figure 4A.5). Some quantitative disagreements were observed, most notably in the amino acid measurements collected under LL conditions, which were likely due to the existence of slowly labeled intracellular pools that were not explicitly included in the isotopomer model. These unmodeled pools appear inactive during the 15-min labeling experiment but become gradually enriched at longer times. Such discrepancies were less prevalent under HL-ACC conditions, likely because overall photosynthetic rates were enhanced and amino acid labeling equilibrated more rapidly.

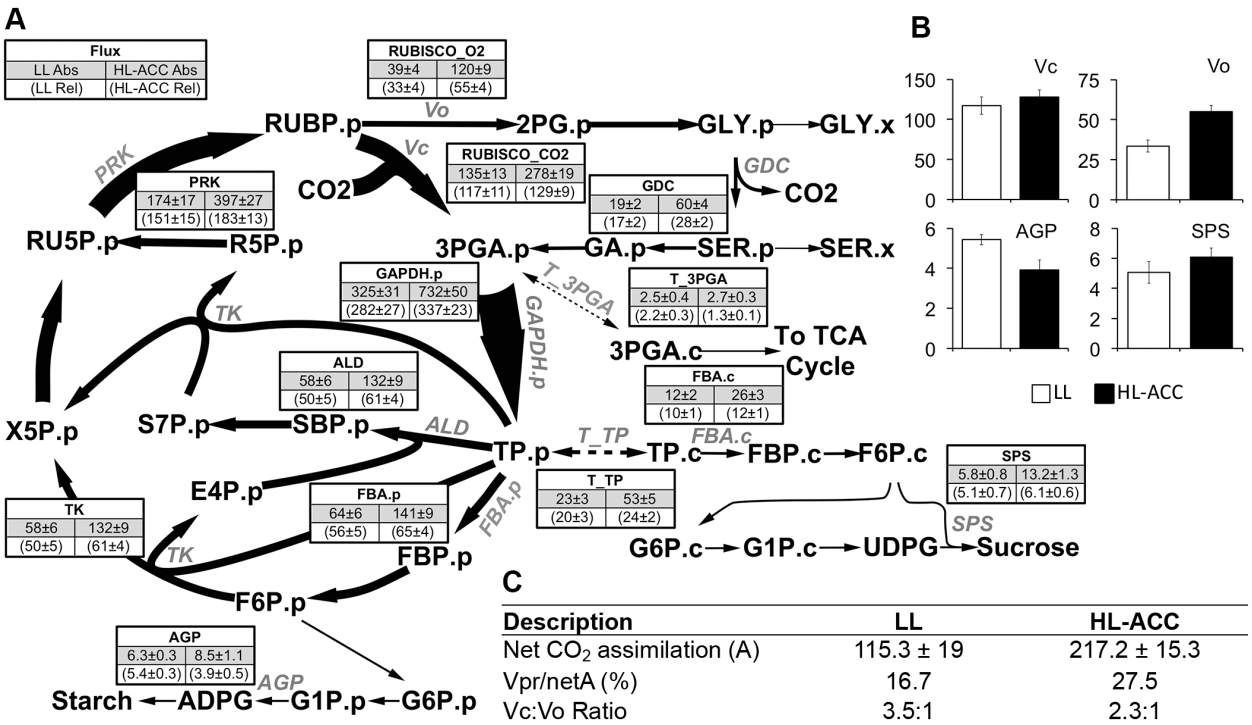

Description	LL	HL-ACC
Net CO_2 assimilation (A)	115.3 ± 19	217.2 ± 15.3
Vpr/netA (%)	16.7	27.5
Vc:Vo Ratio	3.5:1	2.3:1
Sucrose:Starch Ratio	1.9:1	3.1:1

Figure 4.3. Carbon assimilatory fluxes of a photosynthetic *Arabidopsis* leaf.

(A) *Arabidopsis* net flux maps determined under varying light conditions for the LL and HL-ACC conditions. Relative fluxes are presented after normalization to a net CO_2 uptake rate of 100 (SEM, n=6 LL; n=4 HL-ACC). Values shown are the medians of the 95% flux confidence intervals. The estimated standard errors are calculated as (UB95-LB95)/3.92, where UB95 and LB95 are the upper and lower bounds of each confidence interval, respectively, and 3.92 is the number of standard errors that span the 95% confidence interval of a normally distributed random variable. Metabolites compartmentalized to the plastid are denoted by '.p', while metabolites compartmentalized to the cytosol are denoted by '.c'. (B) Selected relative flux values (as a percentage of net CO_2 assimilation). (C) Comparison of photosynthetic parameters; net CO_2 assimilation is in terms of absolute fluxes (μmol metabolite gFW^{-1} hr^{-1}). Abbreviations: netA=net CO_2 assimilation, Vpr=photorespiratory CO_2 release, Vc=carboxylation flux, Vo=oxygenation flux, AGP=starch synthesis flux, SPS=sucrose synthesis flux.

TCA cycle metabolism is challenging to model in leaves because the combination of large organic acid pool sizes and low fluxes relative to CBB cycle (i.e., ~10% or less; [136]) result in poorly identifiable fluxes. To accurately depict the non-cyclic TCA pathway activity, output fluxes to amino acids and sucrose were stoichiometrically constrained to each other on the basis of their measured steady-state concentrations in vascular exudate (Figure 4A.6). As an apoplastic loader, Arabidopsis can export more sucrose during high light acclimation due to H^+/sucrose symport [137,138], which could result in an enhanced ratio of sucrose production relative to amino acids in HL-ACC plants.

Model-determined fluxes were not constrained to a particular measurement but rather were based on nonlinear regression of numerous MID measurements and experimentally-derived starch and CO_2 net assimilation rates. Each model included 54 free flux parameters and required over 1,000 ordinary differential equations (ODEs) to simulate the labeling time course of the measured MIDs (Figure 4.3, Figure 4A.2, Figure 4A.3). Computing the sensitivities of all MIDs to the adjustable parameters required an additional ~94,000 ODEs. The LL and HL-ACC models had sum-of-squared residuals (SSR) of 1003 and 808, which were both accepted based on chi-square tests with degrees of freedom (DOF) equal to 1139 and 1019, respectively (Figure 4.3).

4.4.6 METABOLIC RESPONSE TO ALTERED LIGHT AND ACCLIMATION

Photosynthetic adjustments range from less than seconds to weeks or months dependent on the species and specific developmental process. This study focused on metabolic fluxes determined after nine days of development with exposure to high light and was therefore aimed at examining the acclimated metabolic phenotype and not a short-term response to elevated irradiance. The nine-day time frame allowed plants to acclimate developmentally to a new metabolic pseudo-steady state that was compared to LL leaves through the use of transient isotopic labeling experiments. The short time scale (~15 minutes) of the labeling experiments relative to time scale of acclimation enabled us to apply INST-MFA to obtain a snapshot of the flux values at the end of the acclimation period.

Absolute fluxes (μmol metabolite gFW^{-1} hr^{-1}) obtained from the best-fit models were subsequently normalized by the net assimilation rate to enable direct comparisons of carbon partitioning between LL and HL-ACC conditions (Figure 4.3). Both the carboxylation and oxygenation activities of RuBisCO were established through the modeling process, resulting in a ratio of Vc/Vo that dropped from 3.5:1 in LL plants to 2.3:1 in HL-ACC plants. The change in this ratio reflected an absolute increase in photorespiratory flux from 19 to 60 μmol CO_2 released gFW^{-1} hr^{-1} whereas carboxylation changed from 135 to 278 μmol CO_2 fixed gFW^{-1} hr^{-1}. This resulted in photorespiratory fluxes that were 17 and 28% of net assimilation, respectively. The additional carbon lost to photorespiration in the HL-ACC condition was offset primarily by decreases in the relative flux to starch accumulation (from 33% to 24% of net assimilation).

Despite the increase in photorespiration, the relative flux to sucrose export also increased to support more biomass production in HL-ACC plants. Sucrose export flux more than doubled from 11.7 to 26.4 μmol (hexose units) gFW^{-1} hr^{-1}, while starch production increased marginally from 6.3 to 8.5 μmol (hexose units) gFW^{-1} hr^{-1}. Higher carryover starch levels were observed in HL-ACC leaves throughout the diurnal cycle (Figure 4A.1). HL-ACC plants also had elevated levels of RuBisCO on the basis of leaf area, FW or chlorophyll and produced thicker leaves with more biomass. Furthermore, HL-ACC plants produced more seed biomass (i.e., ten plants produced approximately twice the amount of seeds that resulted in 93% more biomass by weight) with a greater amount of oil, had altered leaf chlorophyll levels, and had reduced measured concentrations of several of the Calvin cycle intermediates (**Table 4A.1**).

Interestingly, measured changes in several CBB intracellular pool sizes were inversely correlated with the model-determined increase in CBB cycle fluxes for HL-ACC plants. We did not supply the pool size measurements to the model when performing data regressions because accurate measurement of absolute pool sizes can be challenging, and other methods aimed at indirectly assessing subcellular compartmentation [75,139] were not applicable within the short time period of this study. As a result, most intracellular pool sizes were not identifiable by INST-MFA. Since pool size estimates were not strongly correlated to flux estimates (Figure 4A.7, Figure 4A.8), precise determination of fluxes could still be achieved despite poor identifiability of pool sizes. This is a

significant advantage of INST-MFA over other modeling approaches that do not utilize full MID measurements, require direct pool size measurements for data regression, or depend upon kinetic parameter values that may not be reliably known *in planta*. We have observed a similar lack of coupling between flux and pool size estimates in previous studies [6], which appears to be a general characteristic of INST-MFA models.

4.5 DISCUSSION

4.5.1 LEAF METABOLIC PHENOTYPING BY INST-MFA

^{13}C INST-MFA provides a comprehensive approach to map the flow and fate of carbon throughout autotrophic metabolic networks [5]. This enables quantitative studies of integrated metabolic pathways, rather than individual reactions or nodes in isolation. Although INST-MFA has been previously applied to cultured cyanobacteria [6], this is the first time that it has been successfully performed in a terrestrial plant. Other recent studies have used $^{13}CO_2$ labeling to estimate fluxes [130] or metabolite turnover [140] from dynamic labeling data by modeling total ^{13}C enrichments, but without applying comprehensive isotopomer models. As presented here, isotopomer models that describe the full MIDs of the measured metabolites are capable of distinguishing flux contributions from different metabolic pathways based on the atomic rearrangements they confer. This approach allows increased pathway-specific information to be extracted from the MS measurements and, importantly, does not require direct pool size measurements to be supplied for model regression. The latter consideration is particularly germane to plant systems, as uncertainties introduced by metabolite compartmentation,

rapid exchange with unmeasurable metabolites, heterogeneous cell populations, or losses during the extraction process may corrupt the absolute pool size measurements and lead to biased flux estimates when using previously established methods.

Though other models were considered based upon biochemical descriptions in the literature, we found that dilution parameters to accommodate photosynthetically inactive metabolite pools were required to achieve statistically acceptable fits to the experimental data (Figure 4A.5), reflecting the cellular heterogeneity of leaves and also the mixing of compartmentalized pools that occurs during cell lysis. Incorporation of dilution parameters into the model enabled a parsimonious description of the labeling dynamics, which did not require detailed modeling of pools that cannot be independently measured and also did not depend on *ad hoc* assumptions found in the literature. The dilution parameters established by modeling were comparable to measurements obtained from a longer-term labeling experiment (t=60 min), thus providing independent validation of this approach. Constraining the dilution parameters in the LL model to match the measured M0 isotopomer abundances at t=60 min (with the exception of the amino acids alanine, serine and glycine that label more gradually than the other metabolites included in the model), resulted in only a small increase in SSR from 1003 to 1087 and did not significantly alter the estimated flux values. Therefore, the change in SSR remained within statistically acceptable bounds and indicated that the estimated dilution parameters were in quantitative agreement with isotope labeling measurements at t=60 min.

4.5.2 PHOTORESPIRATION CHANGES WITH ACCLIMATION TO HIGH LIGHT LEVEL

Methods to quantify photorespiration minimally include: post-illumination CO_2 burst, inhibition of net CO_2 assimilation by O_2, CO_2 influx into CO_2-free air, NH_4 formation, and ratio of $^{14}CO_2$ to $^{12}CO_2$ uptake. The assumptions and limitations for each approach have been summarized elsewhere [141,142]. We considered an alternative strategy using $^{13}CO_2$ labeling followed by computational flux estimation that does not require kinetic constants and therefore avoids some of the measurements and assumptions inherent to other methods. Furthermore, the approach (i) accounts for the exchange of intermediates across mitochondrial, peroxisomal, and cytosolic compartments (e.g., [143]) that interact with plastidic pools and (ii) couples photorespiration flux to biosynthetic demands for folate [144] and amino acid [145] metabolism. Thus photorespiration is treated as a branched network with multiple input and output nodes, consistent with the known biochemistry.

Recent direct measurements of photorespiration indicate values of 14-17% of carboxylation [145,146], consistent with the LL model; however, the range in the literature varies considerably (approximately 6-70% photorespiratory CO_2 release relative to net assimilation). Our results indicate that the absolute rates of carboxylation and oxygenation increased with acclimation to high light intensity, but the rate of oxygenation increased more substantially (Figure 4.3B). The HL-ACC case is not experimentally similar to a short-term exposure to high light because the additional acclimation time results in changes to leaf anatomy. In particular, HL-ACC plants have thicker leaves that maximize exposed chloroplast surface area to the intracellular space

and swollen chloroplasts (Figure 4A.1) that contain heightened levels of RuBisCO per unit leaf area. As the internal CO2 conductance cannot increase in proportion to RuBisCO, leaves have greater internal diffusion resistances and lower CO_2 partial pressures at the site of carboxylation [147] that enhance photorespiration [148]. Combining the ratio of model-derived Vo/Vc ratios for the LL and HL-ACC plants with gas exchange relationships that approximate photorespiration based on CO_2 concentration [141], the difference between LL and HL-ACC photorespiration would be explained by an additional 34% drawdown in the stromal CO_2 concentration at the carboxylation site C_c. This reduction is reasonable, as other studies on high light acclimation in leaves indicate up to 50% decrease in C_c [e.g. [148,149]].

Other parameters such as the enhanced levels of nucleotide cofactors that are co-substrates in photorespiration may also further activate this pathway, rebalancing and consuming additional reducing equivalents across organelles and subverting photodamage [150]. Photorespiration in HL-ACC plants led to consumption of an additional 72% ATP and 65% NADPH relative to the minimum required for CO_2 fixation, whereas in LL these percentages were lower (48% and 43%, respectively) but still significant.

4.5.3 METABOLISM ADJUSTS IN LIGHT

The increase in photorespiratory carbon loss under the HL-ACC condition was associated with a repartitioning of flux among the major carbon sinks represented in the isotopomer

model (Figure 4.3). Relative flux to support sucrose export increased, while relative flux to starch decreased, indicating a higher carbon export capacity that corresponded to increased growth and photosynthetic flux in HL-ACC plants [138]. The modeled sucrose to starch ratio (1.9:1) in LL plants was consistent with the literature and increased in HL-ACC plants to 3.1:1. Thus, the description of intermediary fluxes provided by INST-MFA enabled a global assessment of these flux alterations that would not be observable without a comprehensive, model-based analysis of isotope labeling dynamics.

This study also illustrates how combined analysis of flux and metabolite profiling data can provide complementary information about cellular reprogramming in response to light. For example, several measured metabolite intermediates appeared to adjust to the long-term high light acclimation through decreased pool sizes (on either a FW or chlorophyll basis) within the CBB cycle (Table 4A.11), even as their interconnected pathway fluxes increased. Though this was unanticipated, consistent results were obtained in multiple repeat experiments by using sample collection strategies specifically designed to minimize shading or other potential artifacts.

The pool size measurements were not used in the INST-MFA model regressions, which provide an independent assessment of the metabolic adaptation to high light. Unfortunately, measured changes in metabolite levels could not be verified by INST-MFA, since the 95% confidence intervals for most model-estimated pool sizes exhibited overlap between the two conditions (Table 4A.10). Furthermore, subcellular

compartmentation and/or dilution by inactive pools will impact the model-estimated pool sizes but will not be reflected in the pool size measurements, thus complicating direct comparisons.

Although the inverse correlation between measured intermediate pool sizes and CBB cycle fluxes may seem counterintuitive from the standpoint of mass-action kinetics, it could be explained by increases in enzyme expression or other regulatory changes that occur during the acclimation process and is considered elsewhere [151,152]. These longer-term physiological adaptations are not simply an extrapolation of the short-term response to high light. Further studies are needed to fully define the mechanism underlying this unexpected relationship between CBB cycle fluxes and intermediate pool sizes. However, this finding highlights the potential of ^{13}C INST-MFA to uncover systems-level properties of plant metabolic networks that are not directly observable by static metabolite profiling approaches.

4.6 ACKNOWLEDGEMENTS

We gratefully acknowledge James Gierse, Howard Berg and Sarit Weissmann for technical help and the Proteomics and Mass Spectrometry and Integrated Microscopy Facilities at the Donald Danforth Plant Science Center where instrumentation was located. The authors acknowledge the following funding support: NSF (EF-1105249), GAANN (P200A090323), DOE (DE-AC05-06OR23100) and the USDA-ARS.

4.7 APPENDIX: SUPPLEMENTAL FIGURES AND TABLES

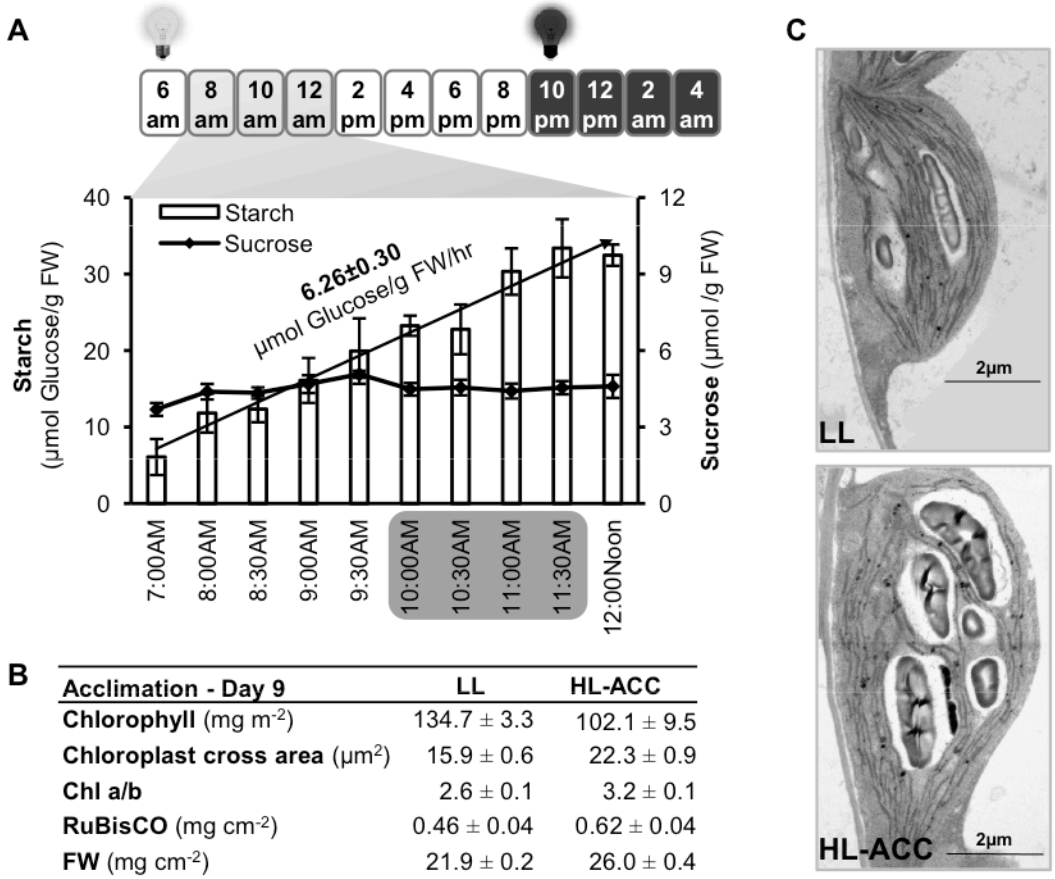

B

Acclimation - Day 9	LL	HL-ACC
Chlorophyll (mg m^{-2})	134.7 ± 3.3	102.1 ± 9.5
Chloroplast cross area (µm^2)	15.9 ± 0.6	22.3 ± 0.9
Chl a/b	2.6 ± 0.1	3.2 ± 0.1
RuBisCO (mg cm^{-2})	0.46 ± 0.04	0.62 ± 0.04
FW (mg cm^{-2})	21.9 ± 0.2	26.0 ± 0.4
DW (mg cm^{-2})	2.1 ± 0.04	2.8 ± 0.1
Total rosette area (cm^2)	29.9 ± 1.8	29.6 ± 1.3
Leaf thickness (µm)	141.0 ± 8.1	200.0 ± 9.1
Leaf carbon (mg g DW^{-1})	369.1 ± 4.7	412.5 ± 13.0
Leaf starch (mg g DW^{-1})	115.3 ± 8.0	210.3 ± 26.2
Seed oil (mg g DW^{-1})	303.0 ± 8.3	353.2 ± 1.8

Figure 4A.1. Leaf metabolism and characterization.

A) Starch production rate and sucrose pool size (SEM, n≥3). Four-week-old plants were grown at 200 µmol m^{-2} s^{-1}. Subsequent labeling experiments were performed near midday when plants exhibited pseudo-steady state metabolism. B) Leaf biomass and photosynthetic characterization acclimated to different light levels (SEM, n≥3) for LL and HL-ACC conditions. High light resulted in consistently altered ratio of Chla/b consistent with other reports [153]. C) Chloroplast ultrastructure imaged in TEM (bars=2µm).

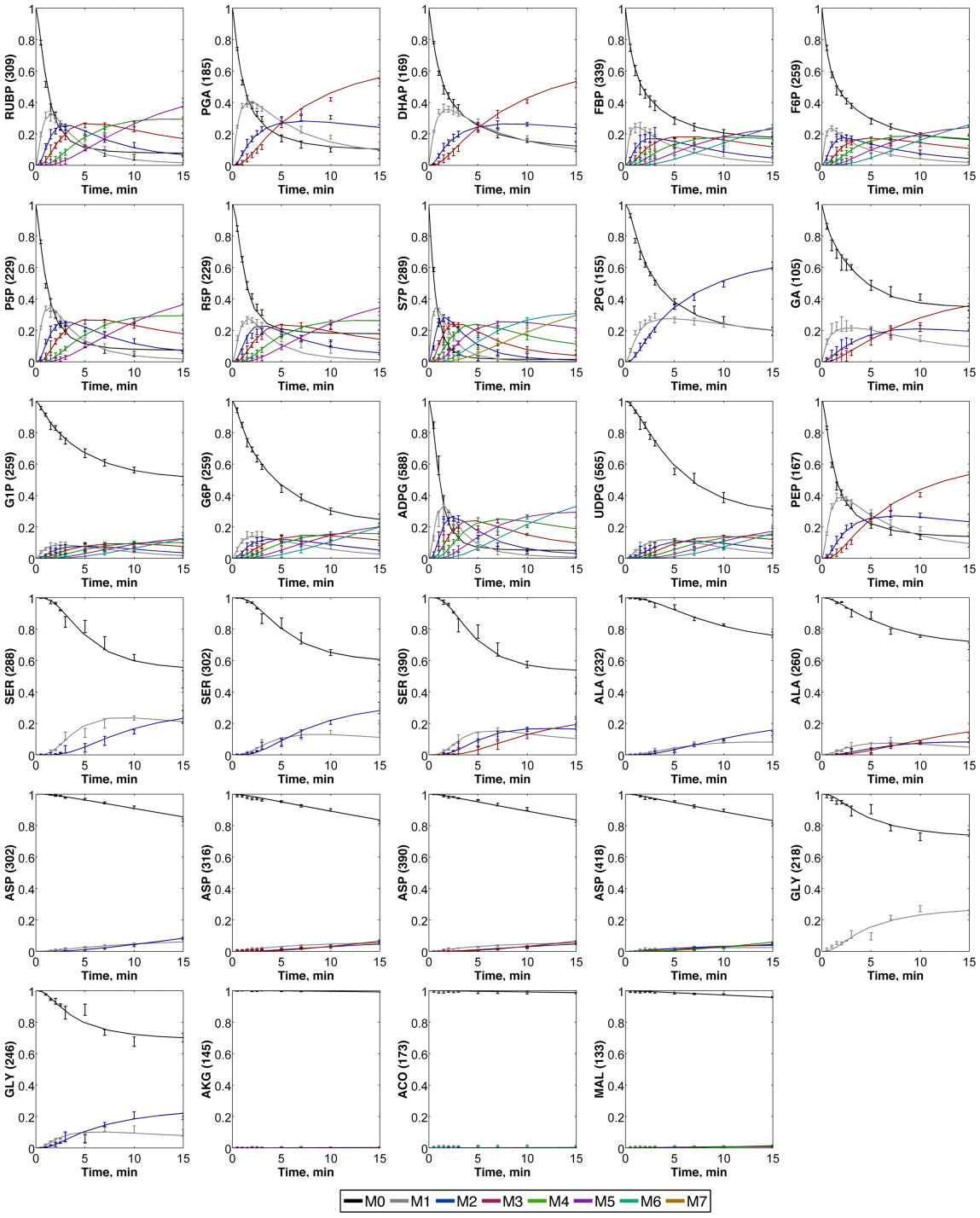

Figure 4A.2. Dynamic isotope labeling trajectories of measured metabolites in LL condition.

Experimentally determined (points with error bars) and INST-MFA fitted (lines) mass isotopomer distributions are shown for low light grown plants (LL). Nominal masses of M0 mass isotopomers are shown in parentheses. Error bars represent standard

measurement errors. Raw mass isotopomer data are shown with correction for natural isotope abundance (SEM; LL, n=6). MIDs of metabolites with near zero labeling (PRO, THR, ASN, GLU, and GLN) are not shown.

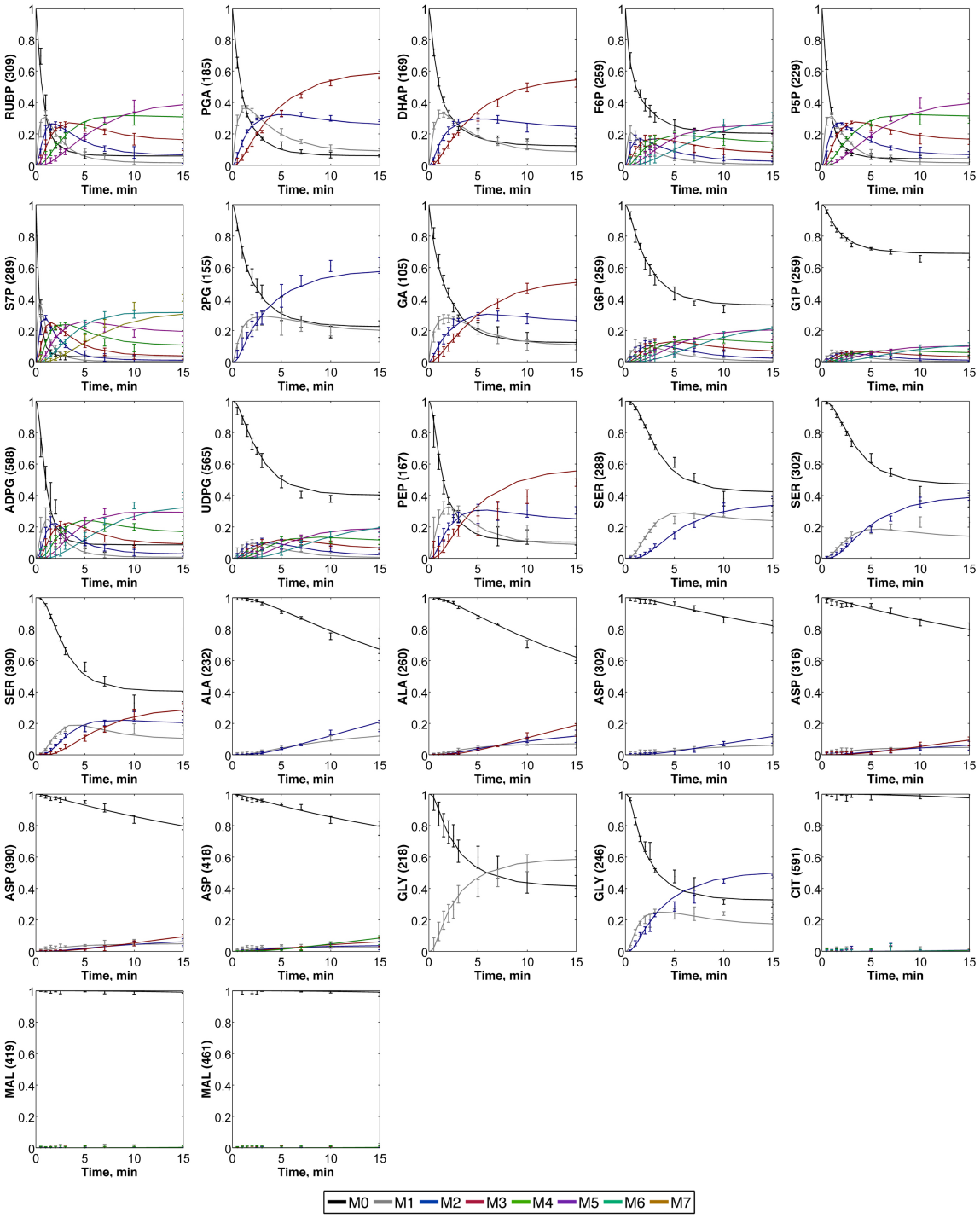

Figure 4A.3. Dynamic isotope labeling trajectories of measured metabolites in HL-ACC condition.

Experimentally determined (points with error bars) and INST-MFA fitted (lines) mass isotopomer distributions are shown for high light acclimated plants (HL-ACC). Nominal

masses of M0 mass isotopomers are shown in parentheses. Error bars represent standard measurement errors. Raw mass isotopomer data are shown with correction for natural isotope abundance (SEM; HL-ACC, n=4). MIDs of metabolites with near zero labeling (PRO, THR, ASN, GLU, and GLN) are not shown.

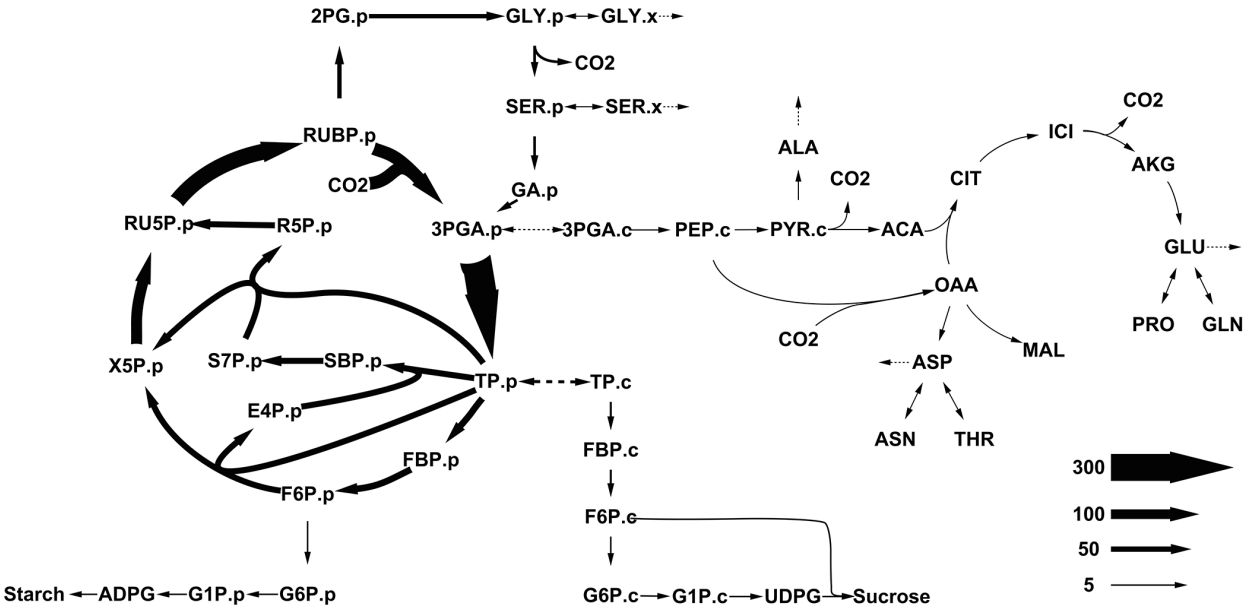

Figure 4A.4. Central carbon metabolic network in *Arabidopsis thaliana* leaves.

Absolute fluxes (μmol metabolite gFW^{-1} hr^{-1}) presented are representative of the LL condition.

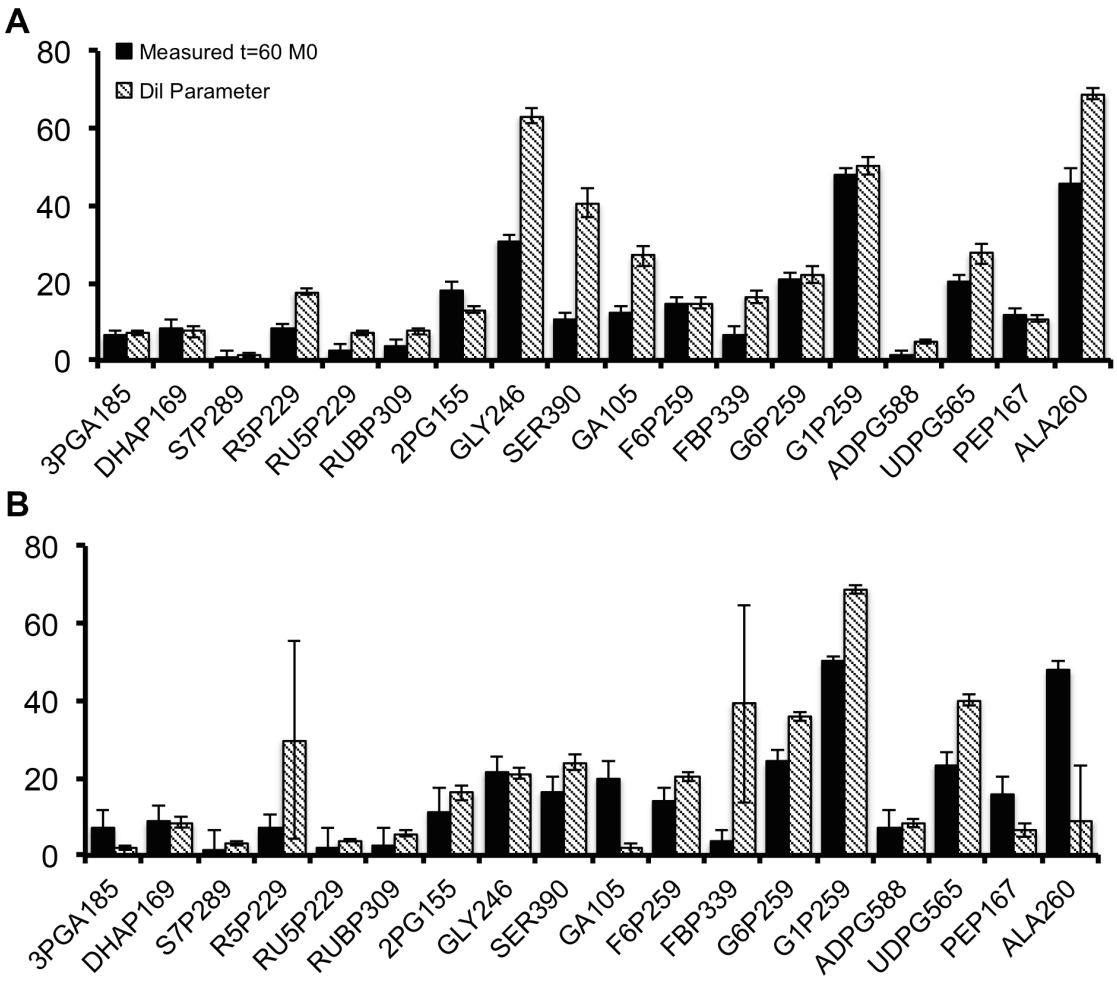

Figure 4A.5. Estimate of inactive pool contributions in A) LL and B) HL-ACC conditions.

Calvin cycle intermediates had relatively low dilution parameters, indicating that they were derived largely from photosynthetically active cells. Most of the model-estimated dilution parameters were qualitatively consistent with inactive pool contributions determined from a longer-term independent ^{13}C-labeling experiment, with the exceptions of amino acid dilutions obtained in the LL experiment. Generally, amino acids exist in multiple intracellular pools with differing metabolic roles, some of which are turned over at time scales that differ from the more rapidly labeled Calvin cycle intermediates. Independent measurements from all pools could not be obtained; therefore the inclusion of dilution parameters provides a parsimonious description of the complex labeling dynamics observed. During low light, the alternative metabolic roles of amino acids

comprise a more significant portion of their overall use. Under high-light acclimated conditions, the model-determined dilution parameters show closer agreement with the 60-min labeling study, which implies that photorespiration plays a more significant role in amino acid metabolism under this condition. Labeling measurements for R5P and FBP were not obtained for the HL-ACC experiment, which resulted in the high uncertainty for the dilution fluxes associated with those metabolites.

A

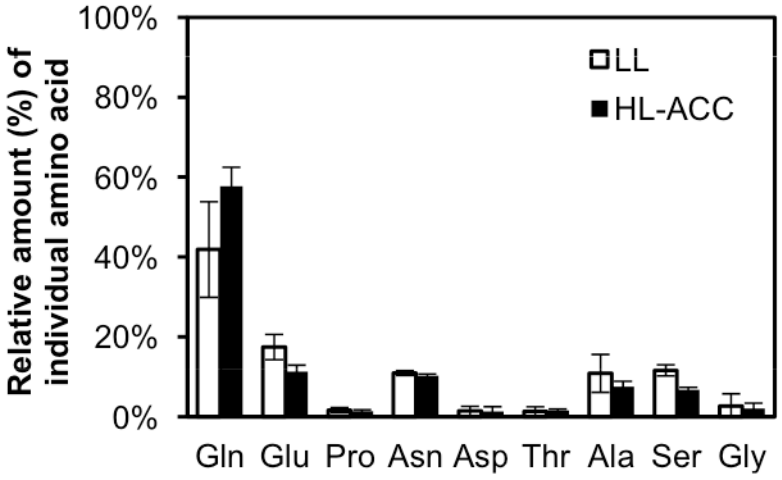

B

		LL	HL-ACC
Content (nmol/µl)	**Sucrose**	20.4 ± 1.5	56.1 ± 31.2
	Gln	3.48 ± 1.98	5.71 ± 4.40
	Glu	1.60 ± 1.12	0.85 ± 0.42
	Pro	0.17 ± 0.17	0.08 ± 0.02
	Asp	0.13 ± 0.10	0.08 ± 0.02
	Asn	1.00 ± 0.66	0.81 ± 0.48
	Thr	0.09 ± 0.04	0.10 ± 0.06
	Ala	0.95 ± 0.69	0.53 ± 0.27
	Gly	0.24 ± 0.19	0.12 ± 0.04
	Ser	1.05 ± 0.71	0.53 ± 0.34
	Total AA	8.7 ± 5.4	8.8 ± 5.6
Ratio (nmol:nmol)	**Sucrose/ G**	6.2 ± 5.0	11.6 ± 7.7
	Sucrose / A	13.9 ± 5.6	44.2 ± 12.2
	Sucrose / Ala	30.8 ± 20.2	92.9 ± 28.2
	Sucrose / Gly	98.1 ± 65.2	357.9 ± 68.9
	Sucrose / Ser	28.7 ± 24.6	95.7 ± 41.6

Figure 4A.6. Sucrose and amino acid concentrations in vascular exudates.

A) Relative amount (% of total) of individual amino acid in vascular exudates (SD, n = 9-12). B) Sucrose and amino acid levels in vascular exudates (SD, n=9-12) and the ratios of sucrose to several amino acids and the families of aspartate (A) and glutamate (G) amino acids that are derived from oxaloacetate and alpha ketoglutarate. Sucrose, glutamine (Gln), glutamate (Glu), proline (Pro), asparagine (Asn), aspartate (Asp), threonine (Thr),

alanine (Ala), serine (Ser) and glycine (Gly) were measurable in exudates. Concentrations and the sugar to amino acid ratios were comparable to previous reports on phloem sap that utilized EDTA exudation methods [154,155]. Amino acid contents in vascular exudates did not change significantly under different light treatments whereas sucrose content increased under HL-ACC, as has been previously reported [156], indicating the phloem loading of amino acids is an independent process and that leaf anatomical changes may facilitate carbon export during acclimation to high irradiance [157]. Mature leaves acclimated to high light that have increased palisade mesophyll thicknesses may export more carbohydrates to meet the increasing demands from sink tissues [138]. Apoplastic loaders are capable of using H+/sucrose symporters to alter sugar export into the phloem [137,138].

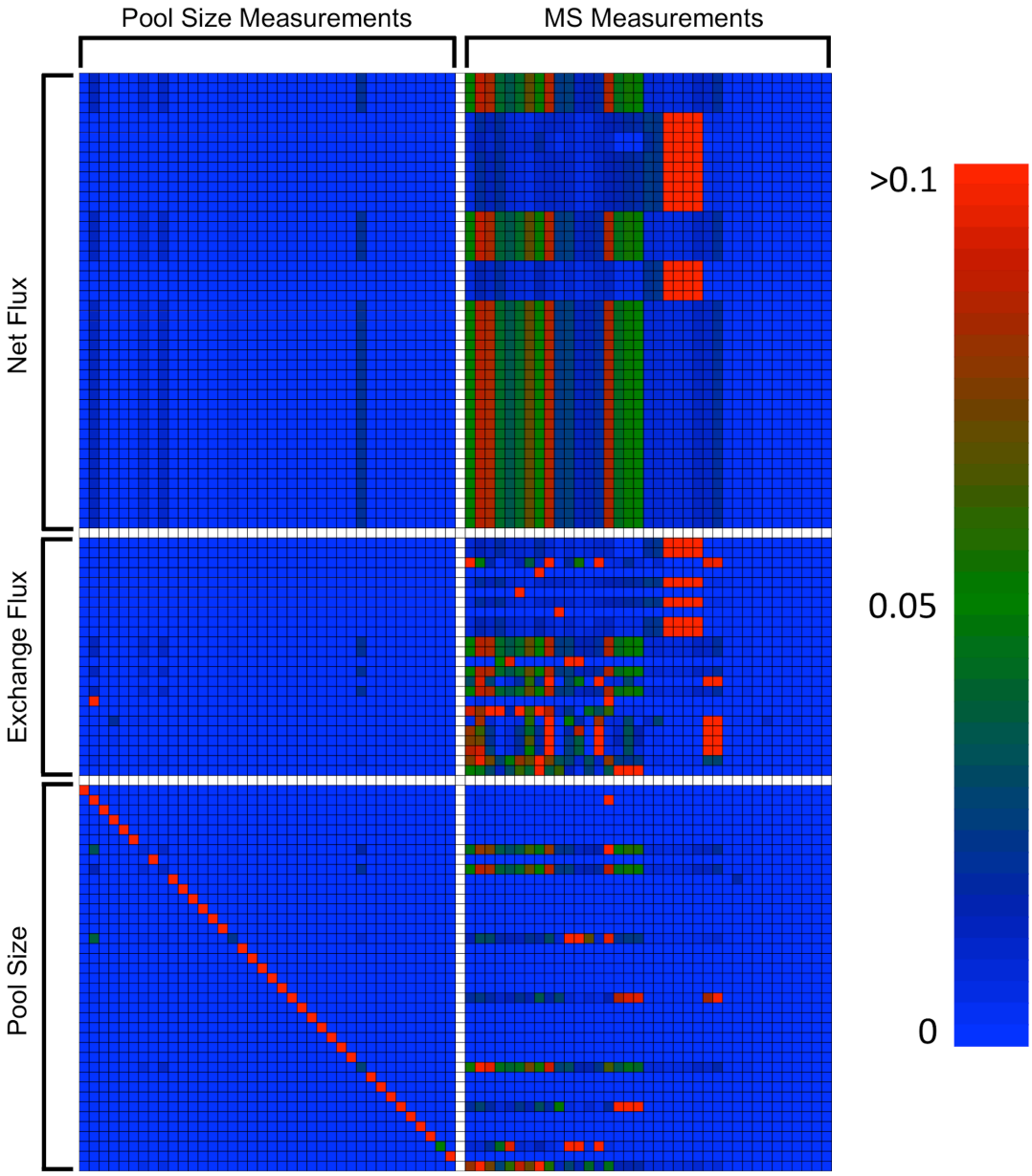

Figure 4A.7. Heat map showing contributions of pool size and isotopic labeling measurements to estimated parameters.

To study the effects of pool size measurements on estimated fluxes, we treated the pool sizes as measurements and computed a "contribution matrix" based on the local parameter sensitivities [34]. Each element of this contribution matrix (e.g., at row i and column j) represents the fractional contribution of the j^{th} measurement to the local variance of the i^{th} parameter. The heat map shows that the MS labeling measurements are more important than pool size measurements in determining the flux values.

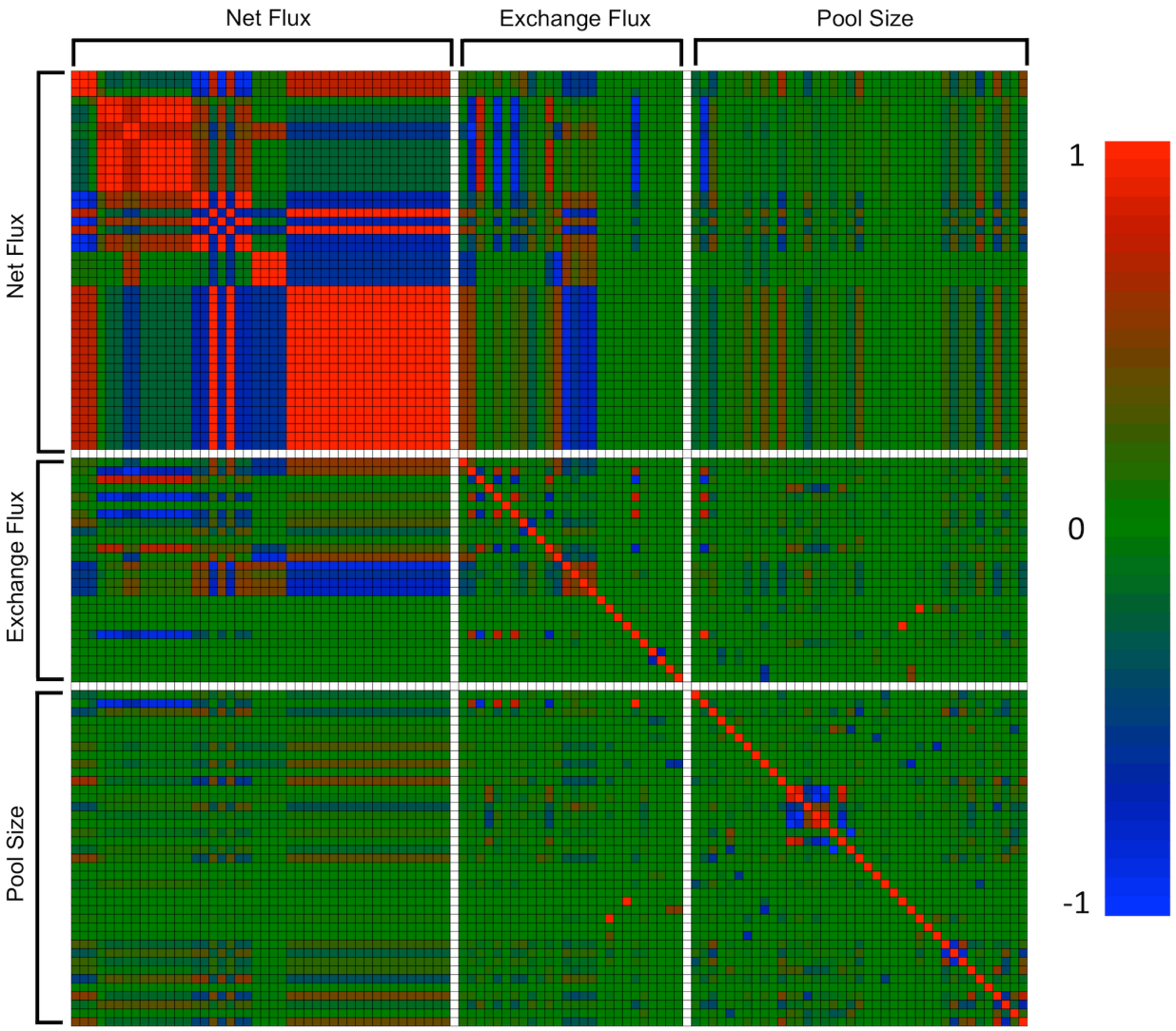

Figure 4A.8. Correlation heat map of estimated parameters.

Each element of this matrix (e.g., at row *i* and column *j*) represents the correlation coefficient between parameters *i* and *j*, where coefficients near 1 indicate positive correlation, coefficients near -1 indicate negative correlation, and coefficients near 0 indicate that the parameters *i* and *j* are uncorrelated. The heat map shows that the net and exchange fluxes are strongly correlated with each other, whereas the estimated pool size parameters only correlate weakly, if at all, with the net and exchange fluxes.

Table 4A.1. Specific compound dependent MS parameters used in multiple reaction monitoring (MRM) for LC-MS/MS.

Metabolites	Parent ion ($[M-H]^-$)		Product ion	
	Formula	Mass	Formula	Mass
PGA	$C_3H_6O_7P^-$	**185**	$[PO_3]^-$	**79**
GAP	$C_3H_6O_6P^-$	**169**	$[H_2PO_4]^-$	**97**
DHAP	$C_3H_6O_6P^-$	**169**	$[H_2PO_4]^-$	**97**
FBP	$C_6H_{13}O_{12}P_2^-$	**339**	$[H_2PO_4]^-$	**97**
F6P	$C_6H_{12}O_9P^-$	**259**	$[H_2PO_4]^-$	**97**
G6P	$C_6H_{12}O_9P^-$	**259**	$[H_2PO_4]^-$	**97**
S7P	$C_7H_{14}O_{10}P^-$	**289**	$[H_2PO_4]^-$	**97**
R5P	$C_5H_{10}O_8P^-$	**229**	$[H_2PO_4]^-$	**97**
P5P (Ru5P/Xu5P)	$C_5H_{10}O_8P^-$	**229**	$[H_2PO_4]^-$	**97**
RUBP	$C_5H_{11}O_{11}P_2^-$	**309**	$[H_2PO_4]^-$	**97**
G1P	$C_6H_{12}O_9P^-$	**259**	$[PO_3]^-$	**79**
ADPG	$C_{16}H_{24}N_5O_{15}P_2^-$	**588**	$C_6H_{11}O_8P^-$	**241**
UDPG	$C_{15}H_{23}N_2O_{17}P_2^-$	**565**	$C_9H_{12}N_2O_9P^-$	**323**
2PG	$C_2H_4O_6P^-$	**155**	$[PO_3]^-$	**79**
GA	$C_3H_5O_4^-$	**105**	$C_2H_3O_3^-$	**75**
PEP	$C_3H_4O_6^-$	**167**	$[PO_3]^-$	**79**
Pyruvate	$C_3H_3O_3^-$	**87**	$C_2H_3O^-$	**43**
ACO	$C_6H_5O_6^-$	**173**	$- 2CO_2$	**85**
AKG	$C_5H_5O_5^-$	**145**	$-CO_2$	**101**
SUC	$C_4H_5O_4^-$	**117**	$-CO_2$	**73**
FUM	$C_2HO_3^-$	**115**	$-CO_2$	**71**
MAL	$C_4H_5O_5^-$	**133**	$- H_2O$	**115**
S6P	$C_{12}H_{22}O_{14}P^-$	**421**	$[H_2PO_4]^-$	**97**
Glycolate	$C_2H_3O_3^-$	**75**	-CO	**47**
Glyoxylate	$C_2HO_3^-$	**73**	-CO	**45**
T6P	$C_{12}H_{22}O_{14}P^-$	**421**	$[PO_3]^-$	**79**

Table A4.2. Specific compound dependent MS parameters used in selected ion monitoring (SIM) with GC-MS.

Metabolite	Mass range	Carbon atoms	Fragmentation
Serine	*288-291*	2, 3	M-$C_7H_{15}O_2Si$
Serine	*302-305*	1, 2	M-$C_7H_{17}O_1Si$
Serine	*390-394*	1, 2, 3	M-C_4H_9
Glycine	*218-220*	2	M-C_5H_9O
Glycine	*246-249*	1, 2	M-C_4H_9
Alanine	*232-235*	2, 3	M-C_5H_9O
Alanine	*260-264*	1, 2, 3	M-C_4H_9
Aspartate	*316-320*	2, 3, 4	M-$C_7H_{15}O_2Si$
Aspartate	*390-394*	2, 3, 4	M-C_5H_9O
Aspartate	*418-423*	1, 2, 3, 4	M-C_4H_9
Threinine	*376-379*	2, 3, 4	M-C_5H_9O
Threinine	*404-408*	1, 2, 3, 4	M-C_4H_9
Glutamate	*330-334*	2, 3, 4, 5	M-$C_7H_{15}O_2Si$
Glutamate	*404-408*	2, 3, 4, 5	M-C_5H_9O
Proline	*258-262*	2, 3, 4, 5	M-C_5H_9O
Asparagine	*417-421*	1, 2, 3, 4	M-C_4H_9
Asparagine	*302-304*	1, 2	M-$C_8H_{18}NOSi$
Glutamine	*431-436*	1, 2, 3, 4, 5	M-C_4H_9
Citrate	*591-598*	1, 2, 3, 4, 5, 6	M-C_4H_9
Succinate	*289-294*	1, 2, 3, 4	M-C_4H_9
Succinate	*331-336*	1, 2, 3, 4	M-CH_3
Fumarate	*287-292*	1, 2, 3, 4	M-C_4H_9
Malate	*419-424*	1, 2, 3, 4	M-C_4H_9
Malate	*461-466*	1, 2, 3, 4	M-CH_3

Table 4A.3. Specific isotopomer-dependent LC-MS/MS parameters.

Q1, m/z of the precursor ion; Q3, m/z of the product ion. Dwell time was set at 20 ms for each transition.

Metabolites	C atoms	Isotopomers	$Q_1[Q_3]$ (m/z) of mass isotopomers
PGA	**3**	$[M]^+$ - $[M+3]^+$	185[79], 186[79], 187[79], 188[79]
DHAP	**3**	$[M]^+$ - $[M+3]^+$	169[97], 170[97], 171[97], 172[97]
FBP	**6**	$[M]^+$ - $[M+6]^+$	339[97], 340[97], 341[97], 342[97], 343[97], 344[97], 345[97]
HP	**6**	$[M]^+$ - $[M+6]^+$	259[97], 260[97], 261[97], 262[97], 263[97], 264[97], 265[97]
P5P	**5**	$[M]^+$ - $[M+5]^+$	229[97], 230[97], 231[97], 232[97], 233[97], 234[97]
S7P	**7**	$[M]^+$ - $[M+7]^+$	289[97], 290[97], 291[97], 292[97], 293[97], 294[97], 295[97], 296[97]
RUBP	**5**	$[M]^+$ - $[M+5]^+$	309[97], 310[97], 311[97], 312[97], 313[97], 314[97]
G1P	**6**	$[M]^+$ - $[M+6]^+$	259[79], 260[79], 261[79], 262[79], 263[79], 264[79], 265[79]
2PG	**2**	$[M]^+$ - $[M+2]^+$	155[79], 156[79], 157[79]
PEP	**3**	$[M]^+$ - $[M+3]^+$	167[79], 168[79], 169[79], 170[79]
GA	**3**	$[M]^+$ - $[M+3]^+$	105[75], 106[75], 106[76], 107[76], 107[77], 108[77]
ACO	**5**	$[M]^+$ - $[M+5]^+$	173[85], 174[85], 174[86], 175[85], 175[86], 175[87], 176[86], 176[87], 176[88],177[87], 177[88], 177[89], 178[88], 178[89], 179[89]
AKG	**5**	$[M]^+$ - $[M+5]^+$	145[101], 146[101], 146[102], 147[102], 147[103], 148[103], 148[104], 149[104], 149[105], 150[105]
SUC	**4**	$[M]^+$ - $[M+4]^+$	117[73],118[73], 118[74], 119[74], 119[75], 120[75], 120[76], 121[76]
FUM	**4**	$[M]^+$ - $[M+4]^+$	115[71], 116[71], 116[72], 117[72], 117[73], 118[73], 118[74], 119[74]
MAL	**4**	$[M]^+$ - $[M+4]^+$	133[115], 134[116], 135[117], 136[118], 137[119]

Table 4A.4. Specific isotopomer-dependent MS parameters for UDP-glucose (UDPG) and ADP-glucose (ADPG).

	Isotopomers	Q1[Q3] (m/z) of mass isotopomers
UDPG	$[M]^+$	565[323]
	$[M+1]^+$	566[323], 566[324]
	$[M+2]^+$	567[323], 567[324], 567[325]
	$[M+3]^+$	568[323], 568[324], 568[325], 568[326]
	$[M+4]^+$	569[323], 569[324], 569[325], 569[326], 569[327]
	$[M+5]^+$	570[323], 570[324], 570[325], 570[326], 570[327], 570[328]
	$[M+6]^+$	571[323], 571[324], 571[325], 571[326], 571[327], 571[328], 571[329]
	$[M+7]^+$	572[324], 572[325], 572[326], 572[327], 572[328], 572[329], 572[330]
	$[M+8]^+$	573[325], 573[326], 573[327], 573[328], 573[329], 573[330], 573[331]
	$[M+9]^+$	574[326], 574[327], 574[328], 574[329], 574[330], 574[331], 574[332]
	$[M+10]^+$	575[327], 575[328], 575[329], 575[330], 575[331], 575[332]
	$[M+11]^+$	576[328], 576[329], 576[330], 576[331], 576[332]
	$[M+12]^+$	577[329], 577[330], 577[331], 577[332]
	$[M+13]^+$	578[330], 578[331], 578[332]
	$[M+14]^+$	579[331], 579[332]
	$[M+15]^+$	580[332]
ADPG	$[M]^+$	588[241]
	$[M+1]^+$	589[241], 589[242]
	$[M+2]^+$	590[241], 590[242], 590[243]
	$[M+3]^+$	591[241], 591[242], 591[243], 591[244]
	$[M+4]^+$	592[241], 592[242], 592[243], 592[244], 592[245]
	$[M+5]^+$	593[241], 593[242], 593[243], 593[244], 593[245], 593[246]
	$[M+6]^+$	594[241], 594[242], 594[243], 594[244], 594[245], 594[246], 594[247]
	$[M+7]^+$	595[241], 595[242], 595[243], 595[244], 595[245], 595[246], 595[247]
	$[M+8]^+$	596[241], 596[242], 596[243], 596[244], 596[245], 596[246], 596[247]
	$[M+9]^+$	597[241], 597[242], 597[243], 597[244], 597[245], 597[246], 596[247]
	$[M+10]^+$	598[241], 598[242], 598[243], 598[244], 598[245], 598[246], 598[247]
	$[M+11]^+$	599[242], 599[243], 599[244], 599[245], 599[246], 599[247]
	$[M+12]^+$	600[243], 600[244], 600[245], 600[246], 600[247]

Table 4A.4. Continued

$[M+13]^+$	601[244], 601[245], 601[246], 601[247]
$[M+14]^+$	602[245], 602[246], 602[247]
$[M+15]^+$	603[246], 603[247]
$[M+16]^+$	604[247]

Table 4A.5. Complete list of reactions and atom transitions for *Arabidopsis* rosette metabolic network.

Enzymatic Reactions for *Arabidopsis* rosette metabolic network			
Calvin Cycle			
RUBISCO_CO2	RUBP.p (abcde) + CO2 (f)	→	3PGA.p (cde) + 3PGA.p (fba)
ALD	TP.p (abc) + E4P.p (defg)	→	SBP (cbadefg)
SBPase	SBP (abcdefg)	→	S7P.p (abcdefg)
TK1	TP.p (cde) + EC2 (ab)	↔	X5P.p (abcde)
TK2	S7P.p (abcdefg)	↔	R5P.p (cdefg) + EC2 (ab)
TK3	F6P.p (abcdef)	↔	E4P.p (cdef) + EC2 (ab)
PPE	X5P.p (abcde)	↔	RU5P.p (abcde)
PPI	R5P.p (abcde)	↔	RU5P.p (abcde)
PRK	RU5P.p (abcde)	→	RUBP.p (abcde)
Photorespiration			
RUBISCO_O2	RUBP.p (abcde)	→	3PGA.p (cde) + 2PG.p (ba)
PGP	2PG.p (ab)	→	GLY.p (ab)
GLYdil	GLY.p (ab)	↔	GLY.x (ab) + GLYout
GDC	GLY.p (ab) + GLY.p (cd)	→	SER.p (cdb) + CO2 (a)
SERdil	SER.p (ab)	↔	SER.x (ab) + SERout
SGA1	SER.p (abc)	→	GA.p (abc)
GK	GA.p (abc)	↔	3PGA.p (abc)
Starch Synthesis			
GAPDH.p	3PGA.p (abc)	→	TP.p (abc)
FBA.p	TP.p (def) + TP.p (cba)	↔	FBP.p (abcdef)
PFP.p	FBP.p (abcdef)	↔	F6P.p (abcdef)
PGI.p	F6P.p (abcdef)	↔	G6P.p (abcdef)
PGM.p	G6P.p (abcdef)	↔	G1P.p (abcdef)
AGP	G1P.p (abcdef)	→	ADPG (abcdef)
SS	ADPG (abcdef)	→	Starch (abcdef)
Sucrose Synthesis			
FBA.c	TP.c (def) + TP.c (cba)	↔	FBP.c (abcdef)
PFP.c	FBP.c (abcdef)	↔	F6P.c (abcdef)
PGI.c	F6P.c (abcdef)	↔	G6P.c (abcdef)
PGM.c	G6P.c (abcdef)	↔	G1P.c (abcdef)
GPU	G1P.c (abcdef)	↔	UDPG (abcdef)
SPS	F6P.c (abcdef) + UDPG (ghijkl)	→	S6P (abcdefghijkl)
TCA cycle			
PGAM.c	3PGA.c (abc)	↔	PEP.c (abc)
PK.c	PEP.c (abc)	→	PYR.c (abc)

Table 4A.5. Continued

PDH	PYR.C (abc)	→	ACA (bc) + CO2 (a)
CS	OAA (abcd) + ACA (ef)	→	CIT (dcbfea)
ACO	CIT (abcdef)	↔	ICI (abcdef)
IDH	ICI (abcdef)	→	AKG (abcde) + CO2 (f)
MDH	MAL (abcd)	↔	OAA (abcd)
Anaplerotic			
PPC	PEP.c (abc) + CO2 (d)	→	OAA (abcd)
Amino Acids			
ALT	PYR.c (abc)	→	ALA.c (abc)
ASPT	OAA (abc)	→	ASP (abc)
GLUDH	AKG (abcde)	→	GLU (abcde)
PCR	GLU (abcde)	↔	PRO (abcde)
GS	GLU (abcde)	↔	GLN (abcde)
TS	ASP (abcd)	↔	THR (abcd)
AS	ASP (abcd)	↔	ASN (abcd)
PhloemOut	S6P + α(GLU) + β(ASP) + γ(ALA.c) + δ(GLYout) + ε(SERout)	→	Sink
Transporters			
T_3PGA	3PGA.p (abc)	↔	3PGA.c (abc)
T_TP	TP.p (abc)	↔	TP.c (abc)

Note: α, β, γ, δ, and ε are measured ratios of output fluxes in amino acids and sucrose

Table 4A.6. Net fluxes determined by ^{13}C INST-MFA under LL and HL-ACC conditions.

Values are absolute fluxes (μmol metabolites gFW^{-1} hr^{-1}) based on the measured net CO_2 uptake rate. Estimated flux values and 95% confidence bounds are shown (SEM; LL, n=6; HL-ACC, n=4).

	LL			HL-ACC		
Reaction	**Value**	LB95	UB95	**Value**	LB95	UB95
Calvin cycle						
RUBP.p + CO2 → 3PGA.p + 3PGA.p	**135.1**	110.3	160.4	**277.8**	239.0	314.8
TP.p + E4P.p → SBP	**57.9**	47.1	69.0	**132.4**	114.4	150.1
SBP → S7P.p	**57.9**	47.1	69.0	**132.4**	114.4	150.1
TP.p + EC2 ↔ X5P.p	**115.8**	94.3	138.1	**264.8**	228.7	300.2
S7P.p ↔ R5P.p + EC2	**57.9**	47.1	69.0	**132.4**	114.4	150.1
F6P.p ↔ E4P.p + EC2	**57.9**	47.1	69.0	**132.4**	114.4	150.1
X5P.p ↔ RU5P.p	**115.8**	94.3	138.1	**264.8**	228.7	300.2
R5P.p ↔ RU5P.p	**57.9**	47.1	69.0	**132.4**	114.4	150.1
RU5P.p → RUBP.p	**173.7**	141.4	207.1	**397.3**	343.1	450.3
Photorespiration						
RUBP.p → 3PGA.p + 2PG.p	**38.6**	30.6	47.8	**119.5**	102.4	137.2
2PG.p → GLY.p	**38.6**	30.6	47.8	**119.5**	102.4	137.2
GLY.p ↔ GLY.x + GLYout	**0.1**	0.0	0.1	**0.0**	0.0	0.0
GLY.p + GLY.p → SER.p + CO2	**19.3**	15.2	23.9	**59.7**	51.2	68.5
SER.p ↔ SER.x + SERout	**0.2**	0.1	0.3	**0.1**	0.1	0.2
SER.p → GA.p	**19.1**	15.1	23.6	**59.6**	51.1	68.1
GA.p ↔ 3PGA.p	**19.1**	15.1	23.6	**59.6**	51.1	68.1
Starch Synthesis						
3PGA.p → TP.p	**325.4**	265.4	387.2	**731.9**	632.3	828.3
TP.p + TP.p ↔ FBP.p	**64.2**	53.4	75.3	**140.9**	122.8	158.8
FBP.p ↔ F6P.p	**64.2**	53.4	75.3	**140.9**	122.8	158.8
F6P.p ↔ G6P.p	**6.3**	5.7	6.8	**8.5**	6.4	10.6
G6P.p ↔ G1P.p	**6.3**	5.7	6.8	**8.5**	6.4	10.6
G1P.p → ADPG	**6.3**	5.7	6.8	**8.5**	6.4	10.6
Sucrose Synthesis						
TP.c + TP.c ↔ FBP.c	**11.7**	8.4	14.9	**26.4**	21.2	31.5
FBP.c ↔ F6P.c	**11.7**	8.4	14.9	**26.4**	21.2	31.5
F6P.c ↔ G6P.c	**5.8**	4.2	7.5	**13.2**	10.6	15.7
G6P.c ↔ G1P.c	**5.8**	4.2	7.5	**13.2**	10.6	15.7
G1P.c ↔ UDPG	**5.8**	4.2	7.5	**13.2**	10.6	15.7

Table 4A.6. Continued

F6P.c + UDPG → S6P	**5.8**	4.2	7.5	**13.2**	10.6	15.7
TCA cycle						
3PGA.c ↔ PEP.c	**2.5**	1.8	3.2	**2.7**	2.2	3.2
PEP.c → PYR.c	**1.1**	0.8	1.4	**1.3**	1.0	1.5
PYR.c + dummy → ACA + CO2	**0.9**	0.7	1.2	**1.1**	0.9	1.4
OAA + ACA → CIT	**0.9**	0.7	1.2	**1.1**	0.9	1.4
CIT ↔ ICI	**0.9**	0.7	1.2	**1.1**	0.9	1.4
ICI + dummy → AKG + CO2	**0.9**	0.7	1.2	**1.1**	0.9	1.4
MAL ↔ OAA	**0.0**	0.0	0.0	**0.0**	0.0	0.0
Anaplerotic						
PEP.c + CO2 → OAA + dummy	**1.4**	1.0	1.7	**1.4**	1.2	1.7
Amino Acids						
PYR.c → ALA.c	**0.2**	0.1	0.2	**0.1**	0.1	0.2
OAA → ASP	**0.4**	0.3	0.5	**0.3**	0.2	0.4
AKG → GLU	**0.9**	0.7	1.2	**1.1**	0.9	1.4
GLU ↔ PRO	**0.0**	0.0	0.0	**0.0**	0.0	0.0
GLU ↔ GLN	**0.0**	0.0	0.0	**0.0**	0.0	0.0
ASP ↔ THR	**0.0**	0.0	0.0	**0.0**	0.0	0.0
ASP ↔ ASN	**0.0**	0.0	0.0	**0.0**	0.0	0.0
S6P + α(GLU) + β(ASP) + γ(ALA.c) + δ(GLYout) + ε(SERout) → Sink	**5.8**	4.2	7.5	**13.2**	10.6	15.7
Transporters						
3PGA.p ↔ 3PGA.c	**2.5**	1.8	3.2	**2.7**	2.2	3.2
TP.p ↔ TP.c	**23.3**	16.9	29.9	**52.8**	42.3	62.9

Note: α, β, γ, δ, and ε are measured ratios of output fluxes in amino acids and sucrose

Table 4A.7. Exchange fluxes determined by ^{13}C INST-MFA under LL and HL-ACC conditions.

Values are scaled according to the transformation $V_{exch} = 100 \times V_{exch}/(V_{exch} + V_{ref})$ where V_{ref} is the net CO_2 uptake flux. The exchange flux is the minimum of the forward and backward fluxes of a reversible reaction. Estimated flux values and 95% confidence bounds are shown.

		LL		HL-ACC		
Reaction	**Value**	LB95	UB95	**Value**	LB95	UB95
Calvin cycle						
TP.p + EC2 ↔ X5P.p	**Unidentifiable**	0.0	100.0	**0.0**	0.0	10.5
S7P.p ↔ R5P.p + EC2	**20.5**	14.8	26.4	**0.0**	0.0	5.3
F6P.p ↔ E4P.p + EC2	**0.0**	0.0	2.8	**0.0**	0.0	6.5
X5P.p ↔ RU5P.p	**49.5**	0.0	70.2	**0.0**	0.0	51.0
R5P.p ↔ RU5P.p	**59.8**	44.3	75.4	**Unidentifiable**	0.0	100.0
Photorespiration						
GLY.p ↔ GLY.x + GLYout	**3.9**	2.1	5.8	**4.4**	3.1	5.8
SER.p ↔ SER.x + SERout	**3.3**	0.8	6.3	**5.9**	4.5	7.4
GA.p ↔ 3PGA.p	**19.4**	14.1	26.2	**31.7**	26.1	39.7
Starch Synthesis						
TP.p + TP.p ↔ FBP.p	**Unidentifiable**	0.0	100.0	**Unidentifiable**	0.0	100.0
FBP.p ↔ F6P.p	**Unidentifiable**	0.0	100.0	**Unidentifiable**	0.0	100.0
F6P.p ↔ G6P.p	**1.4**	0.0	13.4	**Unidentifiable**	0.0	100.0
G6P.p ↔ G1P.p	**99.9**	9.8	100.0	**Unidentifiable**	0.0	100.0
Sucrose Synthesis						
TP.c + TP.c ↔ FBP.c	**23.5**	11.7	37.7	**1.8**	0.4	4.3
FBP.c ↔ F6P.c	**15.7**	9.1	40.0	**Unidentifiable**	0.0	100.0
F6P.c ↔ G6P.c	**67.6**	20.2	100.0	**Unidentifiable**	0.0	100.0
G6P.c ↔ G1P.c	**99.8**	40.4	100.0	**Unidentifiable**	0.0	100.0
G1P.c ↔ UDPG	**71.6**	42.1	100.0	**Unidentifiable**	0.0	100.0
TCA cycle						
3PGA.c ↔ PEP.c	**Unidentifiable**	0.0	100.0	**Unidentifiable**	0.0	100.0
CIT ↔ ICI	**Unidentifiable**	0.0	100.0	**Unidentifiable**	0.0	100.0
MAL ↔ OAA	**0.0**	0.0	0.7	**0.4**	0.0	2.4

Table 4A.7. Continued

Amino Acids						
GLU ↔ PRO	**Unidentifiable**	0.0	100.0	**Unidentifiable**	0.0	100.0
GLU ↔ GLN	**Unidentifiable**	0.0	100.0	**0.0**	0.0	0.9
ASP ↔ THR	**0.0**	0.0	0.2	**0.0**	0.0	0.5
ASP ↔ ASN	**0.0**	0.0	0.2	**0.1**	0.0	0.7
Transporters						
3PGA.p ↔ 3PGA.c	**Unidentifiable**	0.0	100.0	**0.0**	0.0	5.7
TP.p ↔ TP.c	**23.6**	9.0	36.2	**0.0**	0.0	13.4

Table 4A.8. Subcellular contribution parameters determined by ^{13}C INST-MFA under LL and HL-ACC conditions.

The estimated lower and upper 95% confidence bounds of subcellular contributions of metabolites spatially separated in the plastid and cytosol are shown below as percentages of the contribution towards total labeling.

	LL		HL-ACC	
Subcellular Compartmentation, %	LB95	UB95	LB95	UB95
3PGA.p	0.0	93.6	0.0	85.3
3PGA.c	0.0	94.5	12.3	99.1
DHAP.p	6.5	62.9	0.0	64.3
DHAP.c	27.6	88.0	26.3	94.1
F6P.p	29.8	56.3	46.8	57.5
F6P.c	27.6	55.2	21.3	33.9
FBP.p	0.0	27.7	0.0	100.0
FBP.c	56.3	87.1	0.0	100.0
G1P.p	0.0	15.7	8.5	18.4
G1P.c	31.5	51.8	11.2	23.8
G6P.p	5.8	27.2	0.0	27.0
G6P.c	49.1	72.9	36.1	58.8
RU5P.p	0.0	65.1	81.9	96.9
X5P.p	28.0	94.2	0.0	15.0
R5P.p	80.8	83.8	0.0	100.0
GA.p	68.3	78.6	94.7	100.0
SER.p	52.6	67.1	72.4	80.0
GLY.p	33.3	40.4	76.3	81.4
RUBP.p	91.1	94.0	92.9	95.8
S7P.p	97.2	99.8	95.9	97.9
2PG.p	85.4	88.8	80.2	87.7
ADPG.p	94.0	96.3	89.5	93.8
PEP.c	87.6	90.9	90.4	97.1
UDPG.c	67.4	78.6	57.3	62.7
ALA.c	28.5	34.4	44.8	100.0

Table 4A.9. Dilution parameters determined by ^{13}C INST-MFA under LL and HL-ACC conditions.

Dilution parameters represent the percentage of the total sampled pool that is metabolically active, which is equivalent to the 1-G parameter introduced by Kelleher and Masterson [131]. Median parameter estimates and 95% confidence bounds are shown.

	LL			HL-ACC		
Dilution Parameters, %	**Value**	LB95	UB95	**Value**	LB95	UB95
3PGA	**7.1**	5.5	8.6	**2.0**	1.0	2.9
DHAP	**7.5**	4.2	10.2	**8.5**	5.9	10.9
FGP	**14.8**	11.4	17.7	**20.2**	17.9	22.5
FBP	**16.5**	12.9	19.6	**39.2**	0.0	100.0
G1P	**50.2**	45.9	54.2	**68.9**	66.6	71.1
G6P	**22.1**	17.7	25.8	**36.0**	33.7	38.3
RU5P	**7.2**	5.8	8.5	**3.9**	3.1	4.6
R5P	**17.7**	16.2	19.2	**29.8**	0.0	100.0
GA	**27.0**	21.4	31.7	**1.8**	0.0	5.3
SER	**40.7**	32.9	47.4	**24.0**	20.0	27.6
GLY	**63.2**	59.6	66.7	**21.2**	18.6	23.7
RUBP	**7.5**	6.0	8.9	**5.7**	4.2	7.1
S7P	**1.5**	0.2	2.8	**3.1**	2.1	4.1
2PG	**13.0**	11.2	14.6	**16.3**	12.3	19.8
ADPG	**4.9**	3.7	6.0	**8.4**	6.2	10.5
PEP	**10.8**	9.1	12.4	**6.4**	2.9	9.6
UDPG	**27.6**	21.4	32.6	**40.1**	37.3	42.7
ALA	**68.8**	65.6	71.5	**9.1**	0.0	55.2

Table 4A.10. Pool sizes determined by ^{13}C INST-MFA under LL and HL-ACC conditions.

Identifiable pool sizes are those with both nonzero lower and finite upper bounds on their 95% confidence interval. Bounded pool sizes are those with a finite upper bound but with zero lower bound. 95% confidence bounds are shown. Pool sizes units in nmol/gFW.

nmol/g-FW	**LL**		**HL-ACC**	
Pool	LB95	UB95	LB95	UB95
2PG.p	0.0	13.4	132.3	756.8
3PGA.c	0.0	83.0	0.0	147.9
3PGA.p	0.0	81.8	0.0	312.5
ACA	0.0	Inf	0.0	Inf
ADPG.p	0.0	14.9	0.0	11.5
AKG	0.0	Inf	0.0	250.7
ALA.c	10.5	20.1	21.2	73.1
ASN	0.0	Inf	0.0	2057.9
ASP	304.8	687.5	0.0	3.1
CIT	0.0	Inf	0.0	26564.9
CO2	1141.5	1745.2	1908.3	2716.0
F6P.c	0.0	1906.4	0.0	315.1
F6P.p	0.0	54.9	0.0	116.4
FBP.c	0.0	43.2	0.0	1404.9
FBP.p	0.0	55.7	0.0	115.9
G1P.c	0.0	933.0	0.0	351.5
G1P.p	0.0	158.5	0.0	153.3
G6P.c	0.0	911.1	0.0	413.2
G6P.p	0.0	159.4	0.0	79.5
GA.p	0.0	66.9	0.0	290.8
GLN	0.0	Inf	0.0	Inf
GLU	0.0	Inf	0.0	251.8
GLY.p	568.5	1013.1	334.8	1164.7
ICI	0.0	Inf	0.0	26540.2
MAL	0.0	2925.3	0.0	Inf
OAA	0.0	11.3	169.4	1648.6
PEP.c	0.0	73.1	0.0	149.9
PRO	0.0	Inf	0.0	Inf
PYR.c	0.0	1.0	0.0	8.5
R5P.p	809.6	1245.9	0.0	269.5
RU5P.p	0.0	36.3	0.0	272.4
RUBP.p	0.0	19.2	0.0	134.3
S7P.p	0.0	36.8	0.0	51.8

Table 4A.10. Continued

SER.p	399.7	891.2	1264.7	1901.2
THR	0.0	Inf	0.2	Inf
TP.c	0.0	72.3	35.5	510.9
TP.p	0.0	88.2	0.0	231.0
UDPG.c	0.0	1956.3	0.0	1405.9
X5P.p	0.0	35.3	669.0	1071.5

Table 4A.11. Measured metabolite Pool Sizes.

Metabolite pool sizes in LL and HL-ACC samples on the basis of leaf fresh weight, area, and chlorophyll content (SD, n>4) compared with reported metabolite data [128,130,158]. Data were generally comparable. Of note, RuBP concentration was lowest in the HL-ACC condition, though comparable to others [158–161], indicating that available active sites on RuBisCO is more pertinent than the hypothetical total number [162,163]. High light increases the percent activation of RuBisCO and photosynthetic carbon flow that negatively correlate with RuBP levels in *Arabidopsis* [158,164]. Hexose phosphate levels are far from equilibrium, consistent with a regulatory role for starch production relative to RuBP regeneration [165,166]. Increased organic acid contents reflect differences in developmental stage (growth stage was 5.10; [167]) and higher irradiance and were more comparable to [158,168,169]. Amino acid pools were not quantified in absolute though qualitative observations during mass spectrometry were consistent with prior acclimation studies that report minor to insignificant changes in amino acid concentrations, including those linked to photorespiration [109].

	nmol gFW^{-1}					nmol $mgChlorophyll^{-1}$	
Compound	**LL**	**(24)**	**(27)**	**(62)**	**HL-ACC**	**LL**	**HL-ACC**
RUBP	71.0 ± 20.2	46.7 ± 8.2	118.0 ± 11.0	42.0 ± 8.2	10.2 ± 7.1	115.1 ± 32.7	25.9 ± 18.0
3-PGA	180.2 ± 33.9	200.0 ± 45.0	168.0± 15.0	n.d.	57.3 ± 45.6	292.5 ± 55.1	145.5 ± 115.8
DHAP	66.5 ± 18.1	2.7 ± 0.6	57.3 ± 4.2	13.2 ± 2.9	30.0 ± 12.4	108.0 ± 29.4	76.2 ± 31.5
FBP	11.64 ± 4.5	8.9 ± 2.3	31.2 ± 2.4	3.1 ± 0.2	3.6 ± 2.0	18.8 ± 7.3	9.2 ± 5.1
G6P	228.1 ± 56.5	173.0 ± 51.0	272.0 ± 15.0	159.2 ± 17.4	109.5 ± 35.3	370.2 ± 91.7	278.1 ± 89.5
F6P	175.0 ± 16.9	86.4 ± 14.6	128.0 ± 8.0	71.5 ± 12.5	126.4 ± 21.8	283.9 ± 27.5	321.0± 55.4
G1P	29.0 ± 12.7	11.7± 2.4	11.4 ± 1.2	17.9 ± 1.6	33.7 ± 7.9	47.0 ± 20.7	98.7 ± 20.0
S7P	58.9 ± 12.0	28.0 ± 5.4	87.5 ± 4.3	33.8 ± 11.6	48.4 ± 14.1	95.6 ± 19.5	122.9± 35.9
R5P	5.2 ± 0.8	1.2 ± 0.2	3.3 ± 0.8	6.2 ± 1.8	3.9 ± 1.0	8.5 ± 1.4	10.0 ± 2.5
UDPG	163.4 ± 38.7	35.7 ± 5.7	151.0 ± 4.0	86.0 ± 4.8	127.2 ± 37.2	265.1 ± 62.7	323.1± 94.4
ADPG	2.7 ± 0.7	0.6 ± 0.1	1.0 ± 0.1	1.0 ± 0.3	5.0 ± 1.9	4.5 ± 1.2	12.7 ± 4.9
Glycerate	101.1 ± 18.2	169.0 ± 65.0	290.0 ± 11.0	522.3 ± 101.0	209.4 ± 66.4	164.1 ± 29.6	531.8 ± 168.7
2-PGA	8.5 ± 3.4	20.0 ± 4.5	nd	nd	3.6 ± 2.2	13.8 ± 5.5	9.0 ± 5.7
Glycolate	33.1 ± 9.2	nd	nd	nd	44.8 ± 5.1	53.8 ± 14.9	113.8 ± 13.0
Aconitate	143.0 ± 61.9	14.5 ± 5.5	22.8 ± 1.6	nd	106.3 ± 40.5	232.0 ± 100.5	270.0 ± 102.9

Table 4A.11. Continued

2-OG	174.7 ± 27.1	63.1 ± 18.8	90.4 ± 2.6	132.6 ± 32.8	236.8 ± 87.5	283.4 ± 43.9	601.4 ± 222.2
Succinate	353.5 ± 105.4	84.0 ± 48.2	122.0 ± 7.0	nd	472.3 ± 201.0	573.6 ± 171.1	1199.4 ± 510.4
Fumarate	12988.8 ± 1620.8	1154.0 ± 47.0	nd	nd	26330.2 ± 3621.6	21077.1 ± 2630.2	66866.4 ± 9197.2
Malate	9213.0 ± 1381.4	1820.0 ± 547.0	3222.0 ± 185.0	11147.0 ± 1217.0	9301.1 ± 1557.1	14950.1 ± 2241.7	23620.5 ± 3954.4

5. EFFECTS OF A HIGH CARBON ENVIRONMENT AND OVEREXPRESSING A BACTERIAL CARBONIC ANHYDRASE ON *ARABIDOPSIS THALIANA* LEAF METABOLISM

5.1 ABSTRACT

Quantitatively understanding the impacts of environmental and genetic perturbations on photosynthetic carbon fluxes is important for plant metabolic engineering. We previously applied isotopically nonstationary metabolic flux analysis (INST-MFA) for the first time *in planta* to map photoautotrophic metabolism of *Arabidopsis thaliana* leaves at varying light conditions. In this study, we performed INST-MFA on wild-type *Arabidopsis* leaves at varying atmospheric CO_2 concentrations and on three transgenic *Arabidopsis* lines with varying levels of bacterial carbonic anhydrase (BCA) overexpression. These transgenic lines represent the first steps towards recapitulating a fully functional algal carbon concentrating mechanism (CCM) in C3 plants as a strategy to enhance photosynthetic efficiency. INST-MFA revealed that plants exposed to high-CO_2 conditions showed an expected increase in RuBisCO carboxylation and decrease in oxygenation. The transgenic lines also showed an increase in absolute carboxylation flux, but accompanied by an unexpected increase in absolute oxygenation flux. This led to simulation studies that probed both positional and mass isotopomer distributions of key metabolites involved in carboxylation and oxygenation. We found that the labeling patterns that arise from RUBP (ribulose 1,5-bisphosphate) can be used to qualitatively predict low and high ratios of carboxylation and oxygenation, in the absence of

comprehensive flux analysis. This study highlights the usefulness of INST-MFA to describe and quantify the global impacts of targeted genetic modifications on photosynthetic metabolism, which is necessary to guide further rounds of metabolic engineering. The resulting improvements in photosynthetic capacity in *Arabidopsis* leaves provide a scientific framework for similarly transformative steps in crops that are important for biofuel and chemical feedstock needs.

5.2 INTRODUCTION

A major limitation of photosynthetic efficiency in C3 plants is the competitive carboxylase and oxygenase activities of RuBisCO, the enzyme responsible for carbon dioxide fixation [170]. Oxygen fixation by RuBisCO is the first-dedicated step in the photorespiratory pathway, which further reduces photosynthetic efficiency by releasing previously fixed CO_2 during glycine decarboxylation and by limiting regeneration of the CO_2 acceptor molecule RuBP. Overall, photorespiration reduces photosynthetic efficiency by as much as 30% [171]. To date, attempts to engineer RuBisCO isoforms with decreased oxygenase activity have largely been unsuccessful. Significantly, cyanobacteria [172,173], eukaryotic microalgae [174], and C4 plants [175,176] have evolved mechanisms to concentrate CO_2 near the active site of RuBisCO, thus competitively inhibiting oxygenase activity leading to substantial increases in yield and water use efficiency per unit carbon fixed. However, carbon concentrating systems are not operational in the vast majority of plant species. Therefore, there is a critical need to improve the photosynthetic efficiency of C3 plants by engineering mechanisms that will concentrate CO_2 near the active site of RuBisCO.

Currently, there are a number of groups working towards engineering carbon concentrating mechanisms (CCMs) in C3 plants. For example, there is a large effort to improve the yield of rice by redesign of this crop at the cellular level to include a C4 photosynthetic pathway [177–180]. Additionally, Lin et al [181] recently engineered a functional RuBisCO from the cyanobacteria *S. elongatus* PCC 7942 in two transplastomic tobacco lines, which represents an important step toward engineering a cyanobacterial CCM in plants. To our knowledge, no known attempts have been made to incorporate the algal CCM into other species, and our collaborators in the Sayre lab at Los Alamos National Laboratory have been working towards achieving this goal. Eukaryotic microalgae use plasma membrane and chloroplastic envelope bicarbonate transporters to deliver dissolved inorganic carbon to chloroplastic pyrenoid bodies, which contain RuBisCO and carbonic anhydrase (CA); CA accelerates the conversion of bicarbonate to CO_2. When algae are grown under low CO_2 conditions, both bicarbonate pumps and CA expression are increased to elevate internal CO_2 concentrations [182]. As a first step towards testing our algal CCM hypothesis, the Sayre lab has generated three transgenic *Arabidopsis* lines with plastidial overexpression of a bacterial CA (BCA) from *Neisseria gonorrhoeae*, which resulted in substantial biomass increases.

We previously applied isotopically nonstationary metabolic flux analysis (INST-MFA), a comprehensive method that quantitatively describes leaf metabolism, to *Arabidopsis thaliana* rosettes for the first time *in planta*. As described in Chapter 4, this study was

able to assess the effects of environmental light perturbations on the central carbon metabolism of *Arabidopsis* leaves [183]. The flux analysis revealed simultaneous increases in carboxylation and photorespiration fluxes as light intensity increased. In this study, we applied a similar modeling approach to map photoautotrophic metabolism of wild-type *Arabidopsis* rosettes exposed to a high-CO_2 environment and in the three transgenic lines with overexpressed plastidial BCA. Our expectation was that, if BCA functioned to elevate chloroplast CO_2 levels by partially recapitulating the algal CCM, the BCA transgenic lines would mimic the phenotype observed under high-CO_2 conditions in wild-type plants. The Allen lab at the Danforth Plant Science center grew all plants involved in this study, performed the $^{13}CO_2$ labeling experiments, and measured isotope labeling using LC-MS/MS and GC-MS. I integrated and analyzed the MS data generated and carried out the INST-MFA calculations. These studies revealed that the plants exposed to high-CO_2 conditions had increased carboxylation and decreased oxygenation, as expected. However, while the BCA plants had increased biomass and carboxylation flux, the oxygenation flux also increased unexpectedly. This led to further scrutiny of the individual mass isotopomers of the CBB cycle metabolite RUBP to better understand and validate the calculation of oxygenation flux using our INST-MFA model. Through the use of simulation studies, I found that the measured patterns of RUBP enrichment had the highest contribution to the estimated oxygenation flux out of all the available isotopomer measurements. This study shows that accurately assessing *in planta* regulation of photoautotrophic metabolism is crucial to quantifying global impacts of genetic perturbations on metabolic pathways and can guide further rounds of plant metabolic engineering.

5.3 METHODS

5.3.1 PLANT GROWTH

Wild-type *Arabidopsis thaliana* ecotype Col-0 plants were grown at 200 μmol m^{-2} s^{-1} light intensity and under an enriched (800 ppm) concentration of CO_2. After acclimation for 9 days , plants were subjected to isotopic labeling as previously described in Section 4.3.1 and [183]. In addition to the high-CO_2 acclimated plants, three transgenic lines containing a bacterial carbonic anhydrase (BCA) from *Neisseria gonorrhoeae* were also evaluated under ambient CO_2 (330 ppm). These transgenic lines were generated by the Sayre lab at Los Alamos National Laboratory. Physiological parameters, such as chlorophyll, RuBisCO, and starch were quantified as previously described [183].

5.3.2 $^{13}CO_2$ LABELING OF WILD-TYPE AND TRANSGENIC *ARABIDOPSIS* ROSETTES

Isotopic labeling experiments were performed on four-week old wild-type plants acclimated to high CO_2 (HC) and the three transgenic lines with overexpressed BCA (BCA-P1, BCA-P5, BCA-P6). The *Arabidopsis* rosettes were labeled using customized individual plant chambers with a reduced headspace volume of approximately 100 mL. $^{13}CO_2$ was introduced to each plant chamber at a flow rate of 2 L/min. For the plants labeled under the HC condition, ten samples were collected over a 15-minute interval at the following time points: 0.5, 1, 1.5, 2, 2.5, 3, 5 7, 10, and 15 minutes followed by immediate quenching with liquid nitrogen. For the three transgenic lines studied, eight samples were collected over a 15-minute interval at the following time points: 0.5, 1, 1.5, 2, 4, 6, 10, and 15 minutes with immediate quenching via liquid nitrogen.

5.3.3 LC-MS/MS AND GC-MS OF METABOLITE LABELING AND CONCENTRATION

Methods to extract metabolites were done as previously described in Section 4.3.3 and [183]. The final parameters used for isotopomer measurements are listed in the Appendix (Section 5.7).

5.3.4 ISOTOPICALLY NONSTATIONARY ^{13}C METABOLIC FLUX ANALYSIS

INST-MFA was used to estimate intracellular metabolic fluxes. The isotopomer model previously used to describe photosynthetic central carbon metabolism in *Arabidopsis* [183] was used for quantifying fluxes in the HC and BCA plants. The publicly available software package Isotopomer Network Compartmental Analysis (INCA) [24], was used to perform the least-squares parameter regression, as well as statistical and sensitivity analysis of the optimal solution for the four different studies.

5.3.5 SIMULATION STUDIES TO IDENTIFY KEY INDICATORS OF PHOTORESPIRATORY FLUX

INCA was used to perform simulation studies in the HC plants to identify isotope labeling measurements that are most sensitive to the photorespiration flux. Next, the best-fit model from the wild-type *Arabidopsis* leaf model at low CO_2 conditions (LC) [183] was used to perform further simulation studies. The net assimilation, starch, and sucrose fluxes were all fixed to their best-fit values, while the oxygenation flux was varied from 0 to 80 μmol gFW^{-1} hr^{-1} (the best fit oxygenation flux for the LC model was at 39 ± 4 μmol

gFW^{-1} hr^{-1}). INCA was used to simulate the expected isotope labeling trajectories of measurable metabolites for each selected value of the oxygenation flux.

5.4 RESULTS

5.4.1 PLANT DEVELOPMENT OF HC AND BCA PLANTS

Relative to wild-type plants grown at low CO_2 conditions (LC), the four-week-old HC and BCA plants did not display apparent differences in rosette development (Figure 5.1). However, the HC plants did have less RuBiscCO content and total chlorophyll on a fresh weight basis than observed in the LC plants. The three BCA lines had comparable levels of RuBisCO content and total chlorophyll when compared to the LC plants (Figure 5.2). Starch production rate increased more than three-fold in the HC plants, and the BCA plants also showed significantly increased starch production in the P5 and P6 lines (Figure 5.2). The starch production rate in the BCA lines had an inverse correlation with the measured BCA gene expression level (Figure 5.3).

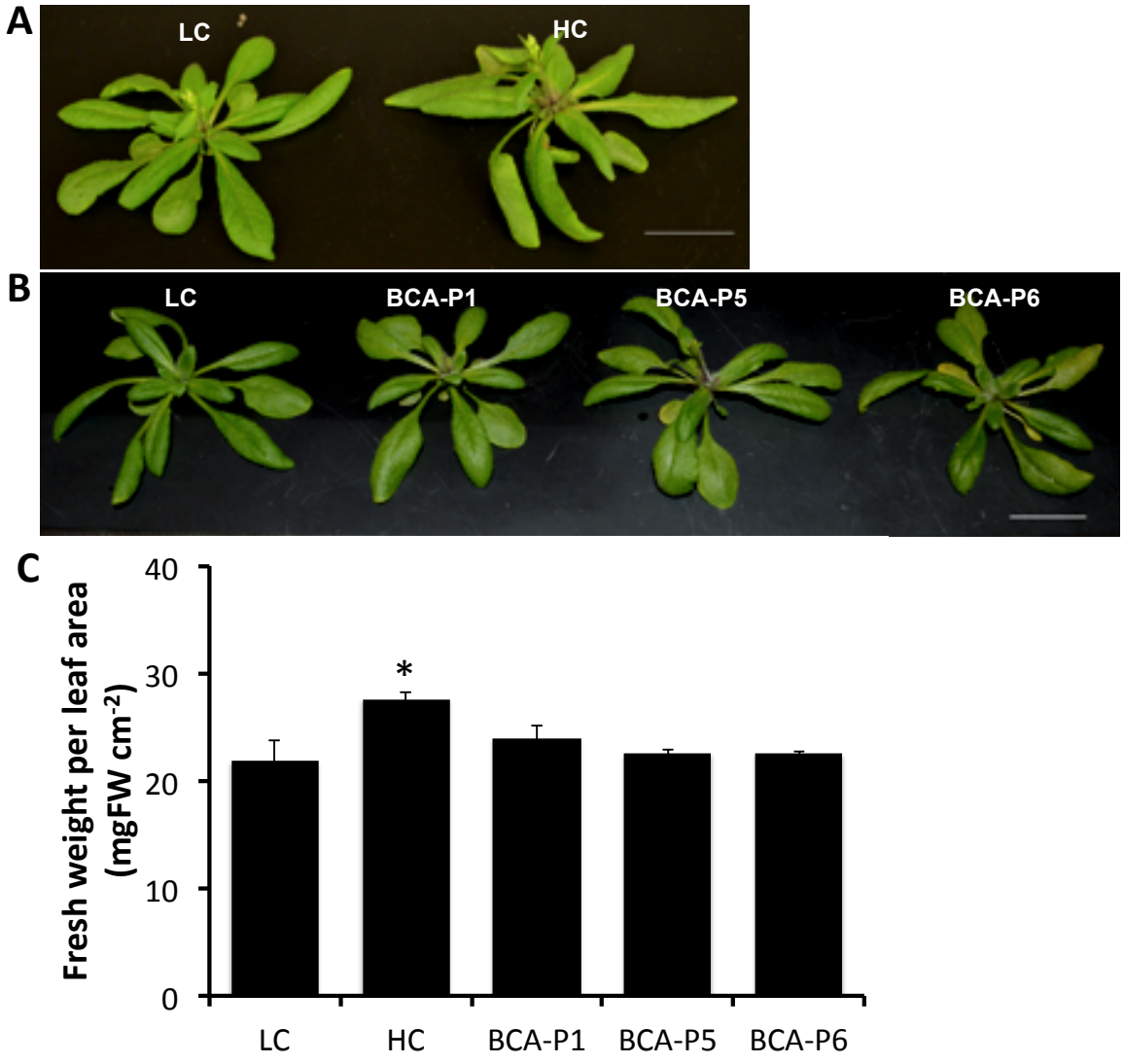

Figure 5.1. Four-week old wild-type and BCA plants (bar=2cm) grown at normal light (200 µmol m^{-2} s^{-1}).

(A) WT *Arabidopsis* rosettes grown under ambient/low CO_2 (LC; 330 ppm) and high CO_2 conditions (HC; 800 ppm). (B) WT and transgenic BCA plants grown at ambient CO_2 conditions (330 ppm). (C) Whole rosette fresh weight per leaf area. Data ± SEM, n≥6; *p<0.05 versus LC.

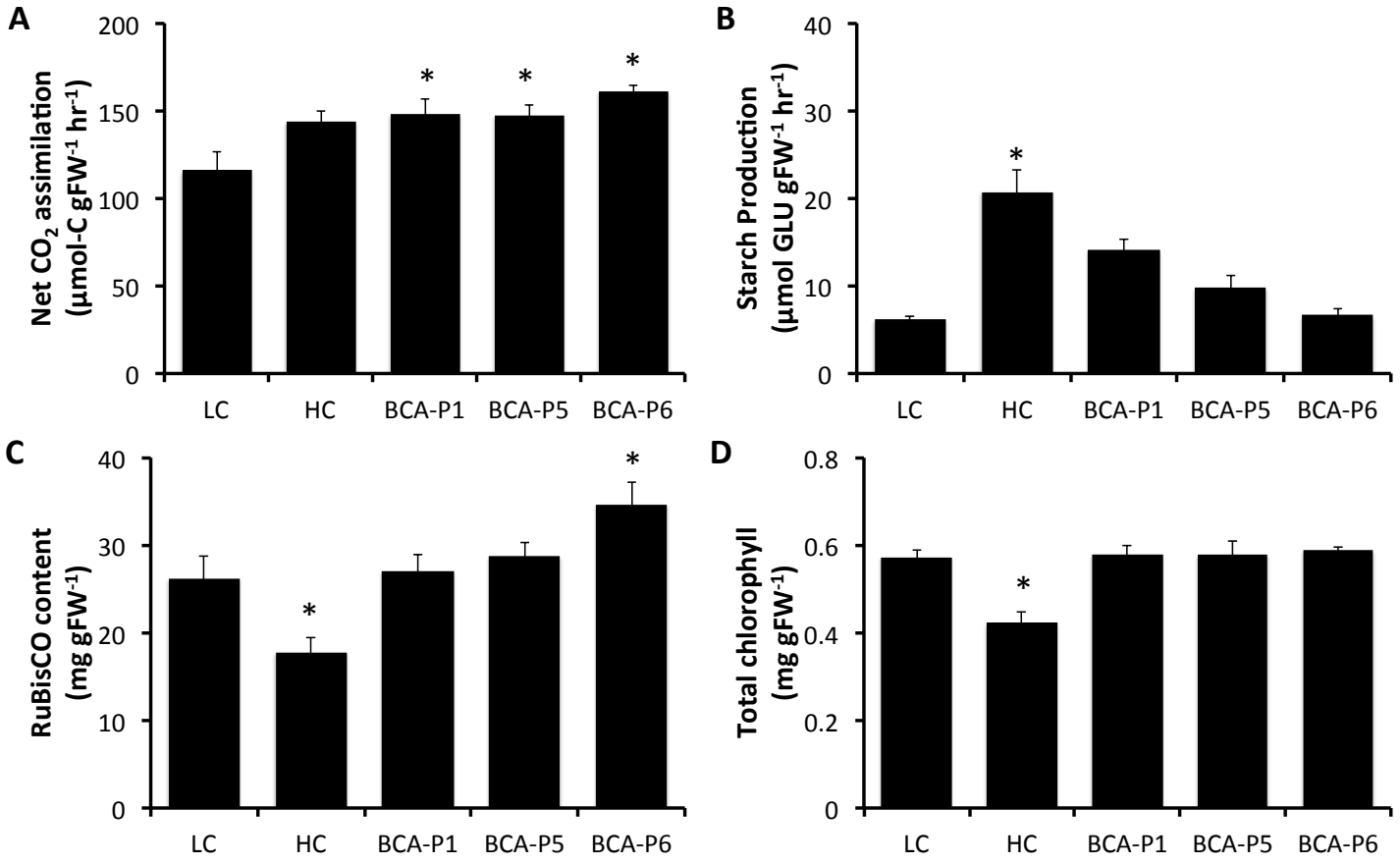

Figure 5.2. Measured physiological parameters of wild-type (LC and HC) and BCA plants.

(A) Net CO_2 assimilation. (B) Starch production rate. (C) RuBisCO content. (D) Total chlorophyll content. Data ± SEM, n≥3; *p<0.05 versus LC.

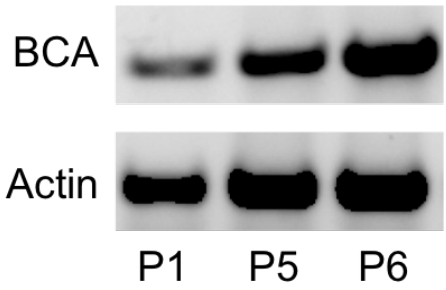

Figure 5.3. RT-PCR of BCA expression.

5.4.2 ^{13}C LABELING OF HC AND BCA PLANTS

^{13}C labeling experiments were carried out on the HC and BCA lines. These labeling experiments were compared to the results of a previous study [183] performed on wild-type rosettes at low CO_2 conditions (LC; study labeled as "LL" in Chapter 4). Similar to the LC plants, intermediates involved in the CBB cycle, photorespiration, and sugar synthesis became enriched at a faster rate than organic and amino acids. These intermediates are highlighted in the metabolic network shown in Figure 5.4. The average percent enrichment curves for selected intermediates in the CBB cycle, photorespiration, and starch/sucrose production are shown in Figure 5.5. In general, CBB cycle intermediates were more enriched in the HC and BCA plants than in the LC plants, which is consistent with the measured net photosynthetic rates in these plants. However, F6P, G6P, and G1P showed less enrichment at later time points in the HC condition than in LC. Comparing between the three BCA lines, the level of enrichment in most of the intermediates showed an inverse correlation with BCA expression.

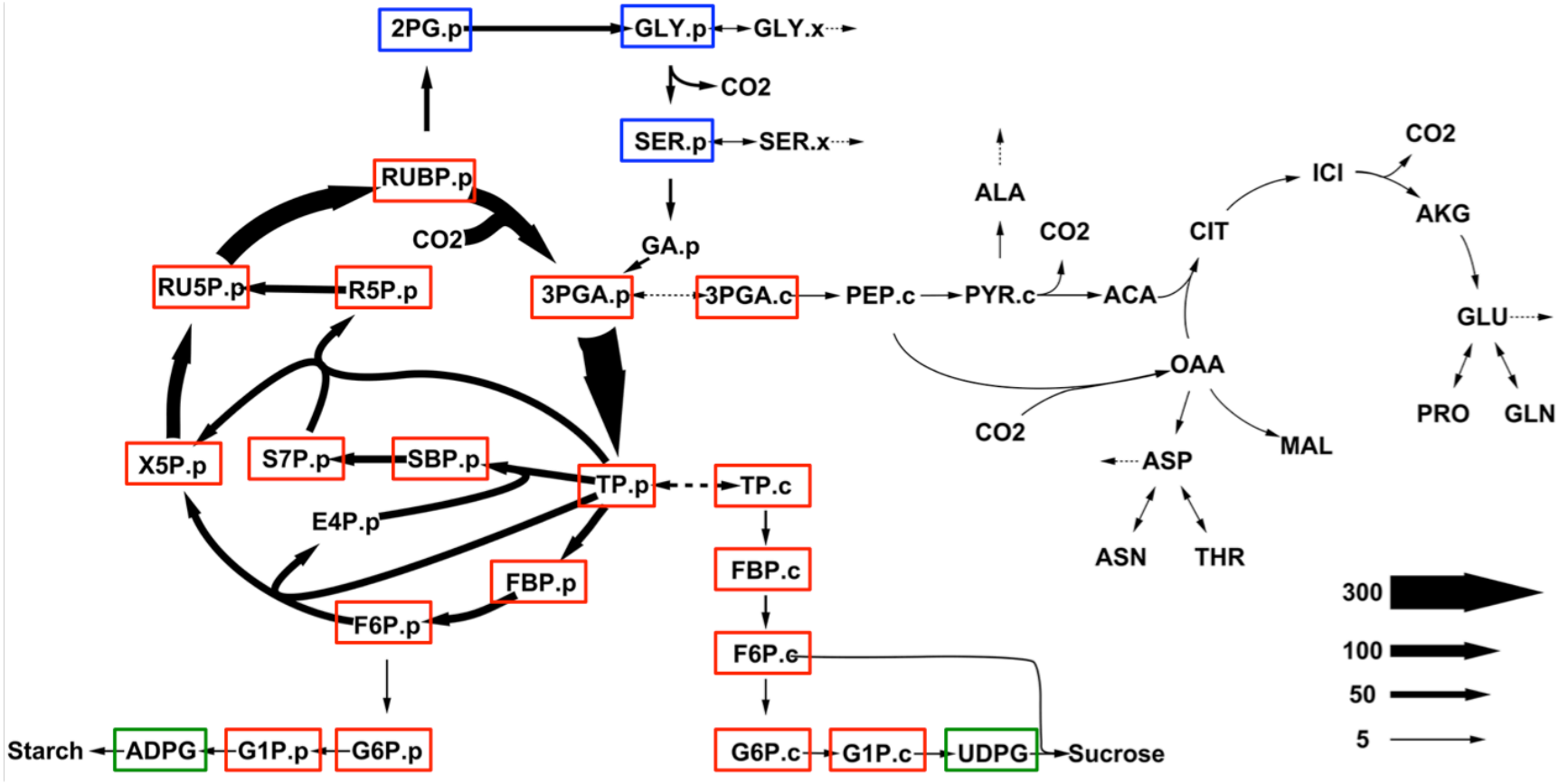

Figure 5.4. Central metabolic network used for flux estimation in *Arabidopsis thaliana* leaves.

Absolute fluxes (µmol metabolite gFW^{-1} hr^{-1}) presented are representative of the LC condition. Measured metabolites in the Calvin cycle (red box), photorespiratory (blue box), and sink precursor (green box) are highlighted on the metabolic network map.

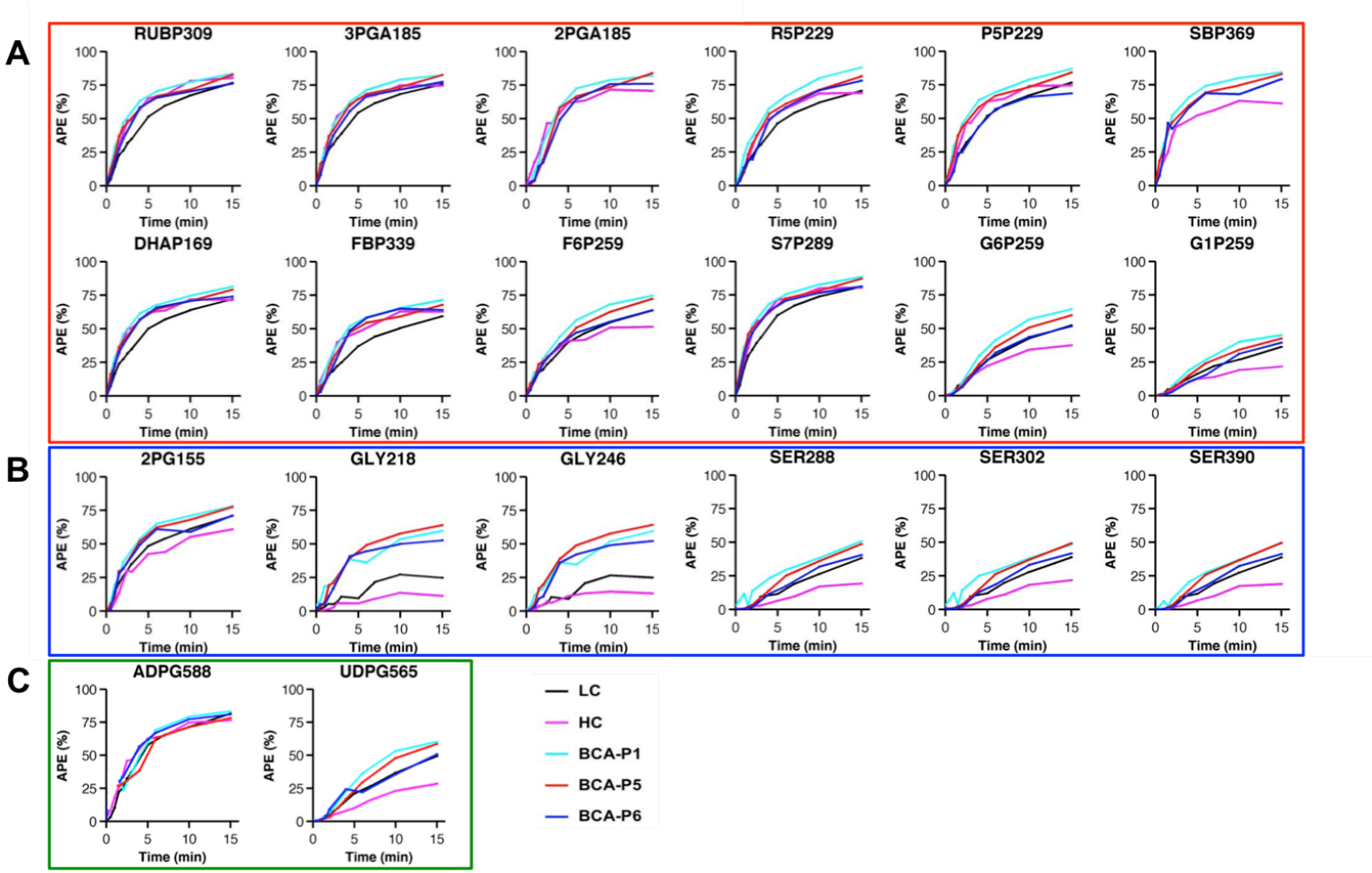

Figure 5.5. Experimentally measured ^{13}C enrichments of intermediates in the LC, HC, and BCA plants.

(A) Calvin cycle intermediates. (B) Photorespiratory pathway intermediates. (C) Starch and sucrose synthesis precursors. 13C enrichment data are shown with correction for natural isotope abundance.

ADPG, which is the precursor to starch production, did not show appreciable differences in labeling across all lines studied, which is reasonable given that the ADPG pool is usually much smaller than other Calvin cycle intermediates. As mentioned before, starch production was enhanced in all lines, most significantly in the HC line, and may reflect a greater degree of feedback inhibition in these plants. Sucrose production was inversely related to starch production because the two major fates of carbon are internetal storage as starch or export as sucrose to feed the other, non-photosynthetic portions of the plant. While there was increased enrichment in the sucrose precursor UDPG in the BCA lines, there was noticeably less enrichment in the HC plants, indicative of reduced flux to sucrose.

Additionally, there was a striking difference in the labeling of the photorespiratory intermediates in both the HC and BCA plants in comparison to LC plants. The labeling profiles of these photorespiratory intermediates were all less enriched under HC conditions than LC conditions, pointing to decreased oxygenation in response to the increase in CO_2 concentration in the HC plants' environment. However, for the BCA lines grown at ambient CO_2 concentrations, the increased labeling of photorespiratory intermediates indicates either oxygenation. In particular, 2PG, glycine, and serine were all more rapidly labeled in the BCA lines.

5.4.3 INST-MFA OF HC AND BCA PLANTS

The measured mass isotopomer distributions (MIDs), net CO_2 assimilation rate, starch production rate, and steady-state levels of sucrose and amino acids in vascular exudate were used to construct comprehensive flux maps of photosynthetic metabolism in the HC and BCA plants using the *Arabidopsis* reaction network established in [183]. To ensure the final solution was the global optimum, flux estimation was repeated 50 times starting from random initial values. The fits of the HC and BCA flux maps were all statistically accepted based on a chi-square test of the sum-of-squared residuals (SSR), which were assessed at the 95% confidence level and are reported in Table 5.1. Photosynthetic parameters of interest are also reported in Table 5.1. A full listing of the optimal parameter estimates including net fluxes, exchange fluxes, subcellular fluxes, dilution fluxes, and pool sizes can be found in the Appendix.

Table 5.1. Comparison of model goodness-of-fit and estimated photosynthetic parameters.

The SSR (sum of squared residuals) of each model was statistically accepted based a chi-square test at the 95% confidence level and the indicated DOF (degrees of freedom) [16]. NetA (net CO_2 assimilation) is shown normalized to fresh weight (μmol metabolite gFW^{-1} hr^{-1}). Abbreviations: netA=net CO_2 assimilation, Vpr=photorespiratory CO_2 release, Vc=carboxylation flux, Vo=oxygenation flux, AGP=starch synthesis flux, SPS=sucrose synthesis flux.

	LC	HC	BCA-P1	BCA-P5	BCA-P6
DOF	1139	1157	897	864	891
SSR	1002	824	741	937	599
netA	115.3 ± 10.9	144.0 ± 5.9	149.5 ± 9.0	147.6 ± 6.2	161.1 ± 3.2
Vpr/netA (%)	16.7	0.9	17.0	17.6	15.5
Vc:Vo Ratio	3.5:1	56.5:1	3.4:1	3.3:1	3.7:1
Sucrose:Starch Ratio	1.9:1	0.2:1	0.8:1	1.5:1	2.9:1

The flux analysis results confirm an overall increase in net photosynthetic assimilation for the HC and BCA plants, based on estimated absolute fluxes (μmol metabolite gFW^{-1} hr^{-1}). Our previous *Arabidopsis* INST-MFA study comparing low-light and high-light acclimated conditions indicated an increase in photorespiration as light intensity increased. However, when light intensity was held constant and CO_2 concentration increased (HC), INST-MFA results indicated that photorespiration decreased dramatically (Figure 5.6). The carboxylation to oxygenation flux ratio (Vc:Vo) increased

from 3.5:1 in LC plants to 43:1 in HC plants. The change in this ratio reflected the drop in oxygenation flux, resulting in the photorespiratory flux accounting for only 1.2% of netA in the HC study. The BCA lines, on the other hand, had Vc:Vo ratios that were more similar to the LC study. While there was an increase in carboxylation, there was also an unexpected increase in oxygenation in the three BCA lines, resulting in photorespiratory fluxes that were 15.4, 18.0, and 14.3% of net assimilation in BCA-P1, P5, and P6, respectively.

The estimated starch and sucrose production fluxes displayed similar trends when compared at both an absolute and relative flux basis (Figure 5.6). HC plants had a dramatic three-fold increase in starch production, leading to a decreased sucrose:starch ratio from 1.9:1 to 0.2:1 in the comparison between LC and HC. The BCA lines also showed varying levels of sucrose:starch production ratios, with BCA-P1 having the lowest ratio, BCA-P5 having the next highest ratio, and finally BCA-P6 having the highest ratio among the three lines. Interestingly, these ratios showed a correlation with the amount of BCA expressed in each of the three lines (Figure 5.3).

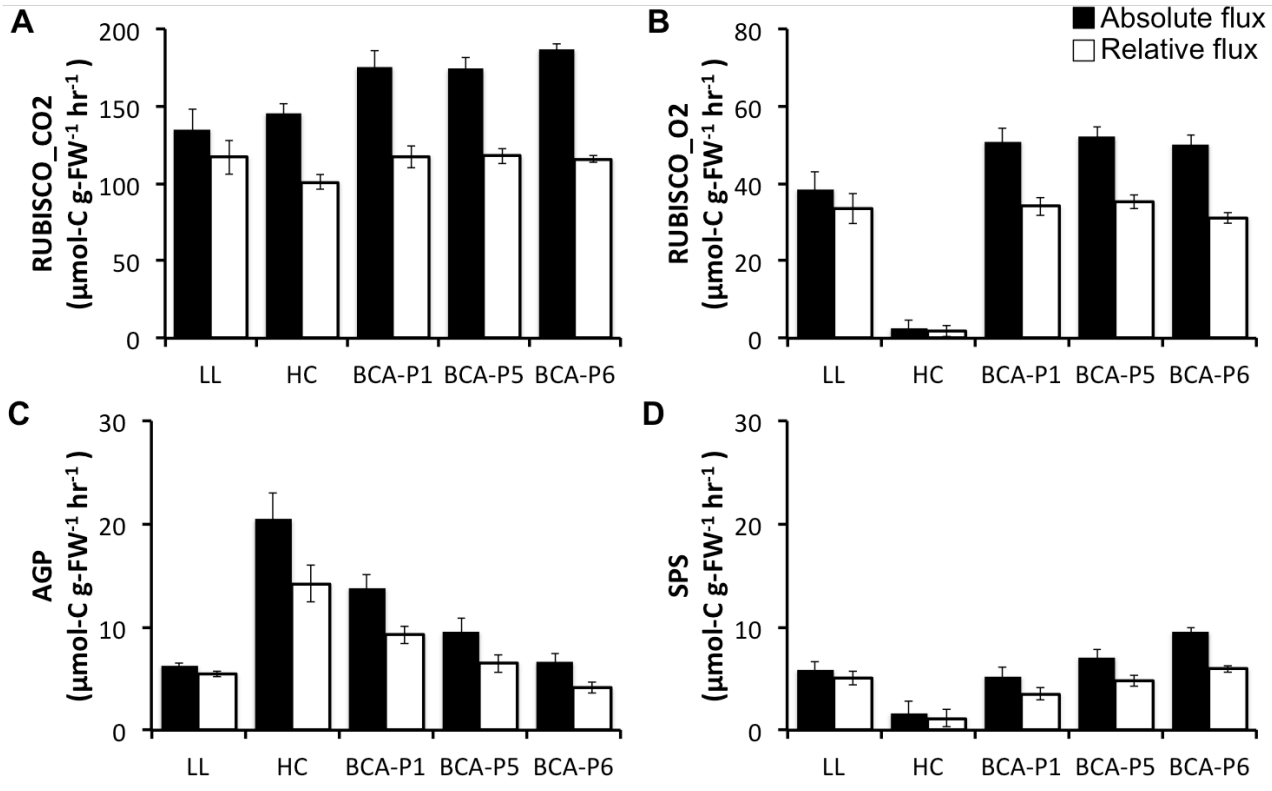

Figure 5.6. Estimated carbon assimilatory fluxes of wild-type and transgenic *Arabidopsis* leaves.

Absolute fluxes (µmol metabolite gFW^{-1} hr^{-1}; black boxes) and relative fluxes (normalized to a net CO_2 uptake rate of 100; white boxes) are shown for (A) RuBisCO carboxylation flux (B) RuBisCO oxygenation flux (C) starch synthesis flux and (D) sucrose synthesis flux. Flux values shown are the medians of the 95% confidence intervals. The estimated standard errors are calculated as (UB95-LB95)/3.92 where UB95 and LB95 are the upper and lower bounds of each confidence interval, respectively, and 3.92 is the number of standard errors that span the 95% confidence interval of a normally distributed random variable

5.4.4 DETERMINING KEY INDICATORS OF PHOTORESPIRATORY FLUX

The INST-MFA results showed a significant difference in photorespiration in the HC study when compared to the LC study. To verify our model and determine the measurements that contributed most significantly to the estimated photorespiratory flux, we tested the sensitivity of our model by removing all of the labeling measurements and activating different combinations of measurements associated with the photorespiratory pathway starting from the best-fit HC model. We examined the effect of activating these different combinations of measurements on the confidence interval of the estimated oxygenation flux. In order to ensure no bias was coming from the measurement errors, we simulated data from the best-fit HC flux map and set all the simulated measurement errors to 0.005. We saw that the inclusion of the RUBP MID had the largest effect on the precision of the estimated oxygenation flux value (**F**igure 5.7).

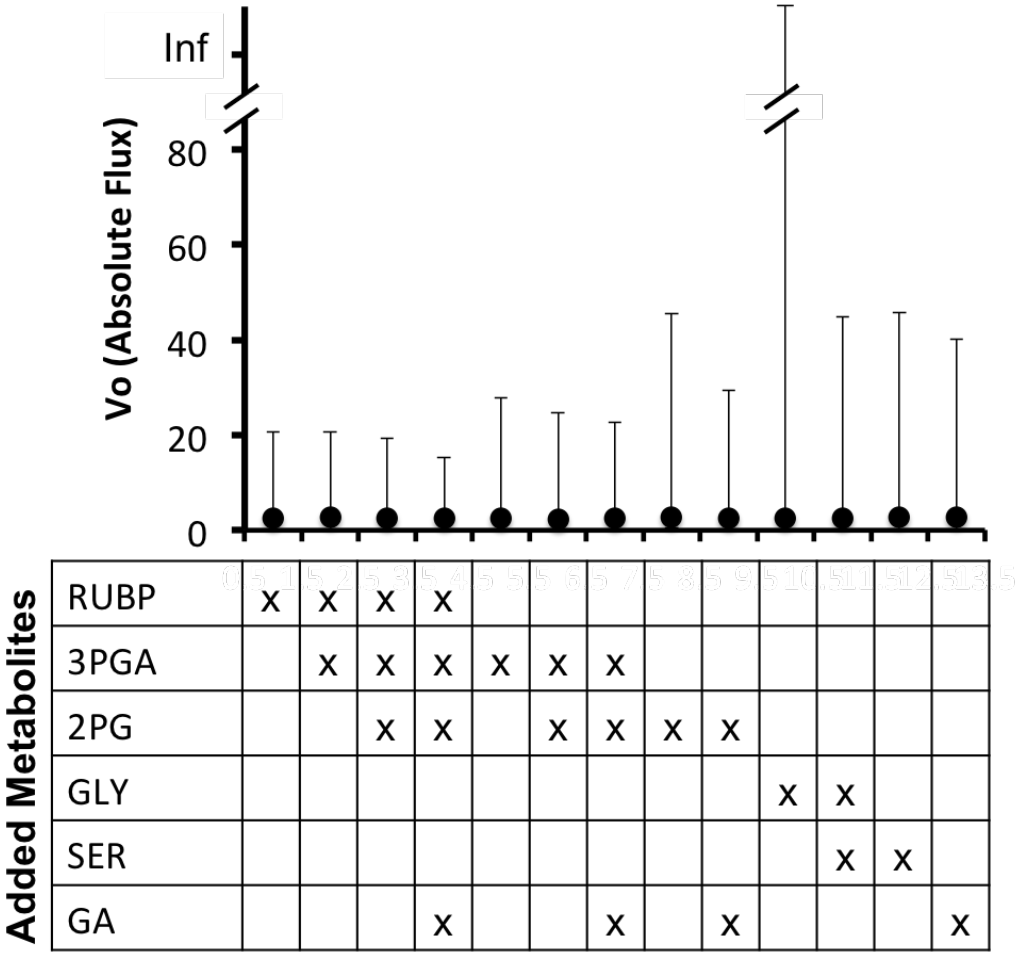

Figure 5.7. Effects of simulated metabolite measurements on the precision of oxygenation flux estimates.

Estimated oxygenation flux values are shown with 95% confidence intervals for each simulation study using various combinations of Calvin cycle and photorespiratory metabolites activated in the model.

5.4.5 POSITIONAL ISOTOPOMER DESCRIPTION OF RUBP LABELING

Taking a further look at RUBP, we examined the experimentally measured and estimated individual mass isotopomers of RUBP across all five labeling studies (Figure 5.8). We observed that M2 mass isotopomer abundances at earlier time points and M4 mass isotopomer abundances at later time points were substantially reduced in HC plants. We also observed that the LC plants had initially slower enrichment of M3 and M5 mass isotopomers, and maintained the lowest M5 enrichment of all plants even after 15 minutes of labeling. To determine if these differences in individual RUBP mass isotopomers provide representative signatures of carboxylation and/or oxygenation rates, we used the best-fit LC model to perform simulation studies that examined the effect of varying oxygenation flux on RUBP labeling.

Oxygenation flux was varied from 0 to 80 μmol gFW^{-1} hr^{-1} while holding netA, starch, sucrose, and TCA fluxes fixed. In order to maintain overall mass balance, fluxes associated with carboxylation were allowed to vary as oxygenation was changed. Figure 5.9 shows the trajectories of individual RUBP mass isotopomers that were simulated for a range of different oxygenation values. Even though there were no noticeable differences in M0 abundance for the different oxygenation rates, M2, M4, and M5 mass isotopomers were sensitive to variations in oxygenation. And while MS measurements can only describe MIDs and not positional enrichment information like NMR [15], we were able to use the best-fit LC flux model to simulate positional ^{13}C enrichment information for each individual carbon atom of RUBP, 3PGA, and 2PG (Figure 5.10). The positional enrichment plots for RUBP showed equivalent labeling in C1 and C2, as well as in C4

and C5. The C3 carbon in RUBP showed the most enrichment. Similarly, 3PGA showed similar labeling in C2 and C3, with C1 being the most enriched. Finally, 2PG showed equivalent chances of labeling between its two carbon atoms. Figure 5.11 shows the simulated positional enrichments of RUBP in response to variations in oxygenation. As oxygenation increased, enrichments at all five carbon atoms decreased, which is consistent with less labeled CO2 entering the CBB cycle. The positional simulation shows that C1 and C2 (carbons 1 and 2) have equal chances of being labeled, as well as C4 and C5. However, C3 shows the fastest and highest labeling in comparison to the other four atoms of RUBP. The labeling signatures that arise at these individual carbon atoms can then be related back to the mass isotopomer distributions, which determine the estimated fluxes from INST-MFA.

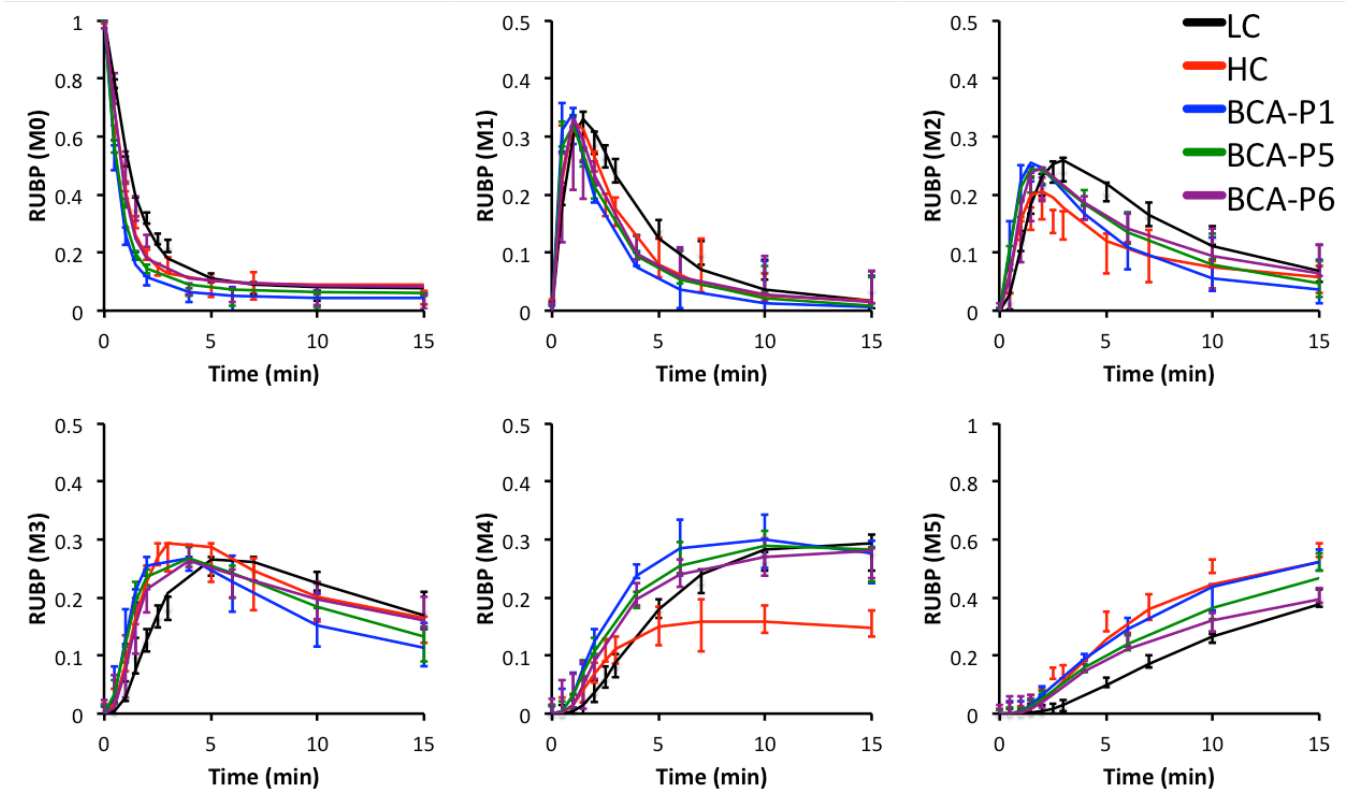

Figure 5.8. ^{13}C labeling trajectories of RUBP.

The experimentally measured mass isotopomer abundances (data points) and INST-MFA model fits (solid lines) are shown for RUBP in each of the five studies. Raw mass isotopomer data are shown with correction for natural abundance.

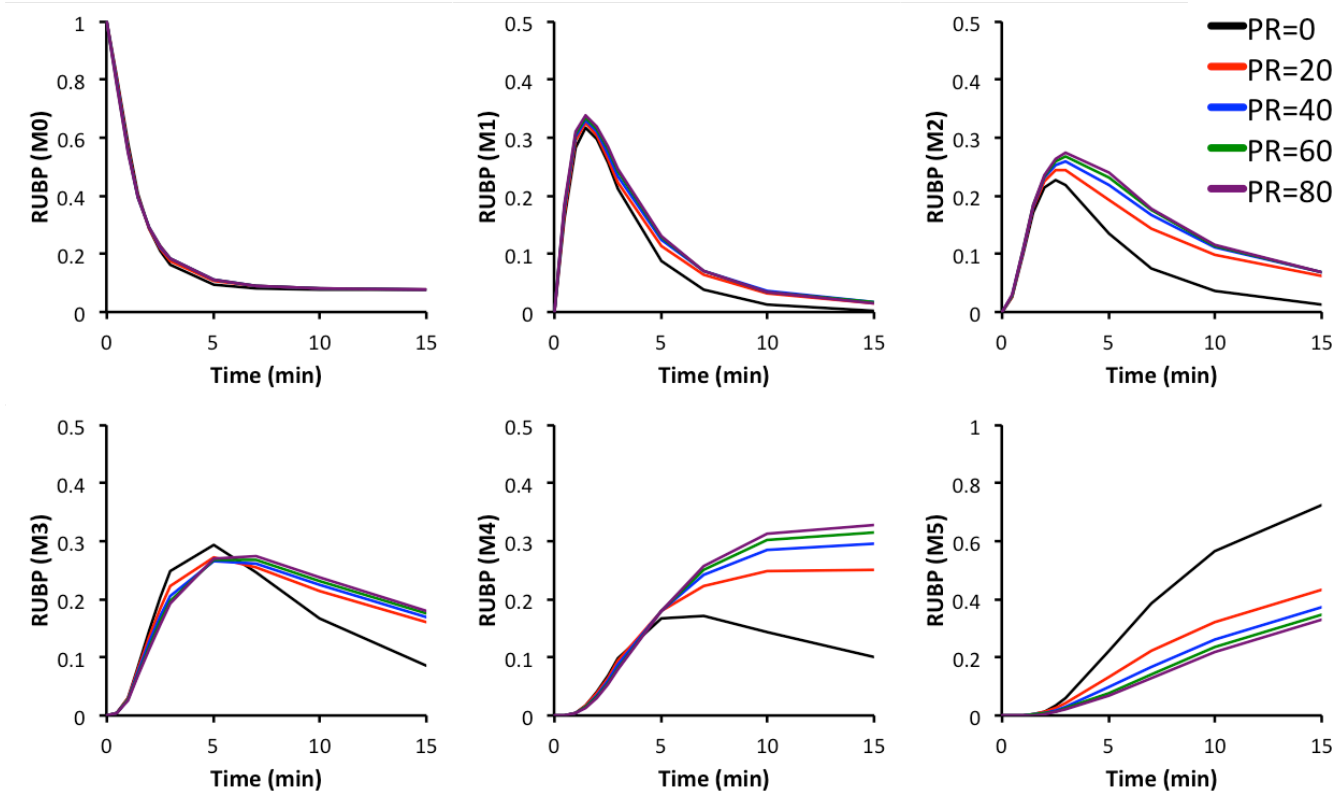

Figure 5.9. Simulated mass isotopomer distributions (MIDs) of RUBP for varying levels of photorespiration (PR).

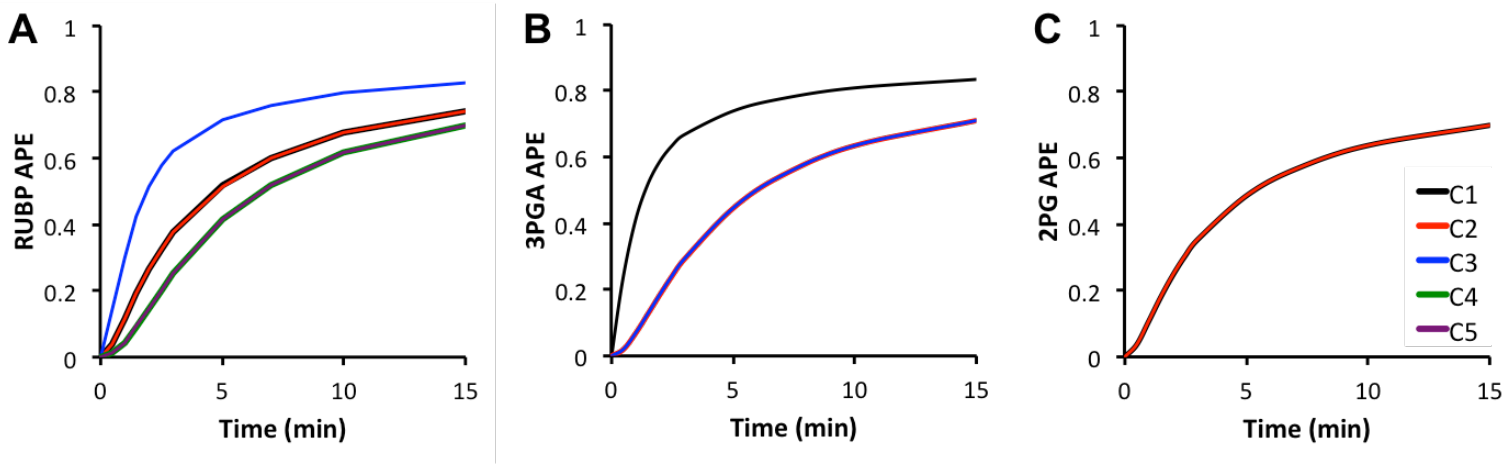

Figure 5.10. Simulated positional isotopomer distributions of (A) RUBP (B) 3PGA and (C) 2PG using the best-fit LC flux model.

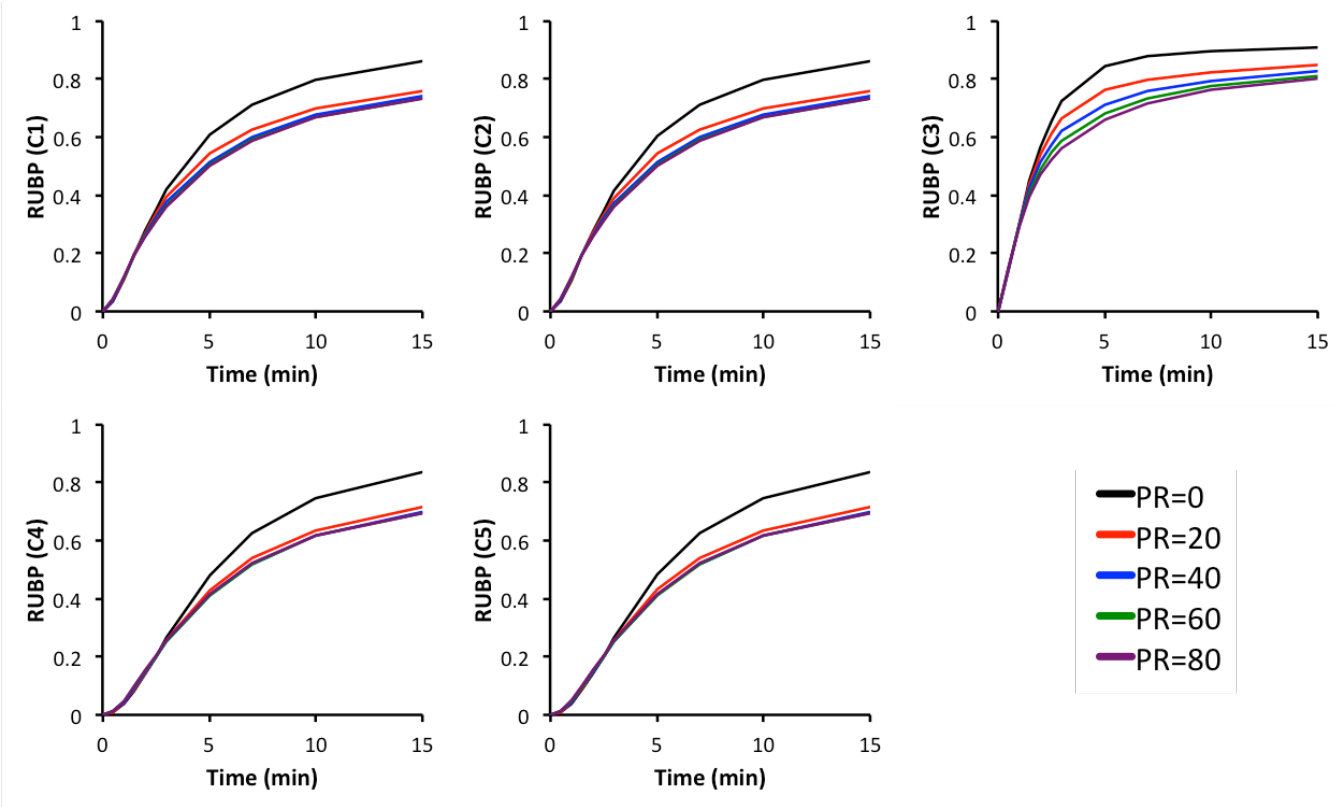

Figure 5.11. Simulated positional isotopomer distributions of RUBP for varying levels of photorespiration (PR).

5.5 DISCUSSION

5.5.1 RESPONSE OF PHOTOSYNTHETIC FLUXES UNDER A HIGH CO_2 ENVIRONMENT

Our CCM hypothesis is predicated on the limited amount of CO_2 that is immediately available to the active site of RuBisCO. As a control, we subjected wild-type plants to increased CO_2 conditions for comparison with transgenic BCA lines that were hypothesized to increase CO_2 levels near the active site of RuBisCO. As expected, artificially enhancing atmospheric CO_2 concentration resulted in more efficient carbon use with less photorespiration. In general, increasing atmospheric CO_2 levels enhances C3 photosynthesis and inhibits photorespiration because increased delivery of CO_2 to RuBisCO accelerates the carboxylation reaction while suppressing the competing oxygenation reaction [184,185]. This suppression in oxygenation reduces the CO_2 loss and energy costs associated with photorespiration. A study by Florian et al. [186] investigated the effects of increasing CO_2 levels on wild-type *Arabidopsis* rosettes to 900 ppm under non-acclimated conditions and also obtained similar oxygenation flux results of 3% Vpr/netA, which were calculated using Sharkey's equation [141]. The labeling of the CBB cycle and photorespiratory pathway intermediates reflected the change in Vc:Vo flux ratio. On a relative flux basis, this dramatic decrease in photorespiration led to a reduced flux through the CBB cycle since RUBP was not diverted toward oxygenation as in the case of LC plants. This was also reflected in the decrease in RuBisCO content in the HC plants [187].

The HC plants also produced more biomass, although the exact mechanism of how biomass increased is currently unclear. There was a measured three-fold increase in starch production, matching the estimated starch production flux. However, unlike the high-light studies in [183], the rate of sucrose production flux was reduced, implying that sucrose export during the day may not account for the increased biomass production and may instead have been feedback inhibited. The increase in CO_2 could have unmasked a bottleneck in the export of sucrose, which affects the triose translocator balancing the amount of carbon and phosphate between the plastid and cytosol. Generally, the triose translocator moves triose from the plastid to the cytosol in exchange for phosphate that is moved from the cytosol to the plastid [188]. Without the phosphate from the triose translocator, the accumulation of starch provides an alternative way to get the needed phosphate to fuel the CBB cycle.

While the labeling rate of ADPG was similar in both the LC and HC plants, UDPG labeling was reduced in the HC study. ADPG and UDGP are the precursors to starch and sucrose, respectively. This is in agreement with the reduced sucrose production rate in HC plants. This could also be indicative of bigger pool sizes of intermediates in the (cytosolic) sucrose synthesis pathway as a result of increased CO_2 concentration. The flux analysis results show that the estimated 95% confidence interval upper bounds for the cytosolic hexose phosphates and UDPG pool sizes were increased in the HC plants (Table 5A.5). Since the labeling measurements reflect a mixture of compartmentalized pools, we have built reactions into our model to account for the different compartmental contributions of metabolites located in both the plastid and cytosol. The hexose

phosphates F6P, G6P, and G1P showed increased cytosolic contributions in the HC plants, which was consistent with the observed decrease in the enrichment of these intermediates. This decrease in enrichment could also indicate bigger inactive pools, matching the reduced carboxylation machinery as shown by decreased RuBisCO content. While the estimated dilution flux values did not reflect this, the overlap in the confidence intervals in the estimated fluxes leaves this particular hypothesis inconclusive. Further analyses of measured compartmentalized pool sizes acquired by additional techniques, such as non-aqueous fractionation [189,190], could help probe this hypothesis further.

Since both high light and high carbon perturbations lead to increased biomass, it is clear that plants have different mechanisms to enhance growth dependent upon which resources are limiting. Unraveling this complexity at the systems level is a problem well-suited for MFA, and further labeling studies will have important implications for improving crop yield.

5.5.2 A CLOSER LOOK AT LABELING OF RUBP

To assess the validity of our model and the significantly lower photorespiratory flux calculated in our HC labeling study, we performed simulation studies on the best-fit HC flux model to determine which measurements were most responsible for the estimated photosrespiratory flux. Using the best-fit model from the HC study, we found that inclusion of the RUBP measurement had the largest effect on the precision of the oxygenation flux value. While adding other measurements involved with the first steps of

carboxylation or oxygenation, such as 3PGA or 2PG, respectively, helped to make the confidence interval tighter, having only 3PGA or 2PG alone increased the confidence interval of the flux relative to RUBP alone. This is reasonable since the labeling of 3PGA and 2PG both come directly from RUBP (Figure 5.12).

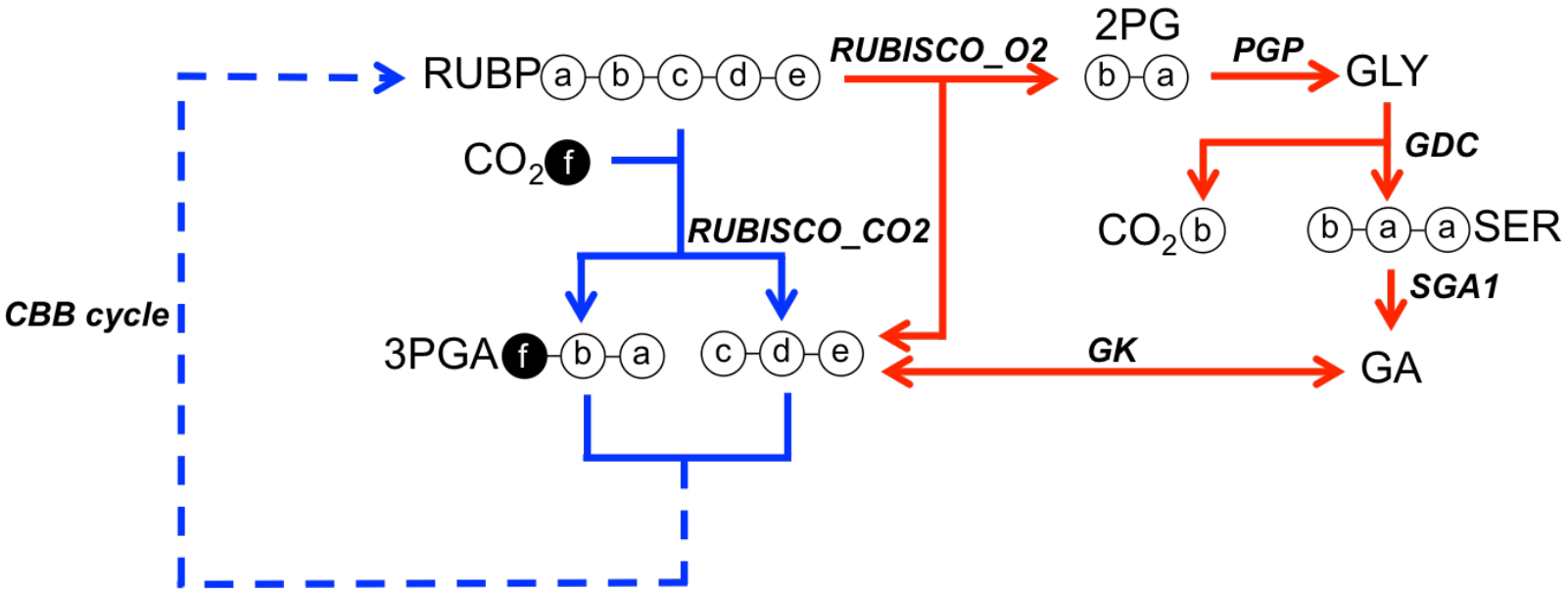

Figure 5.12. Isotope labeling in carboxylation and oxygenation pathways.

A schematic diagram of either RuBisCO carboxylation (blue) or oxygenation (red), showing the fate of the RUBP carbon atoms.

When the experimentally measured mass isotopomers of RUBP were plotted against one another in the five different studies, we found that M2 and M4 accumulated more slowly in HC plants while M3 and M5 lagged behind in LC plants. Since it was difficult to completely discern the combined contributions of carboxylation and oxygenation to these experimentally derived RUBP MIDs, we simulated measurements while varying oxygenation linearly from values of 0 to 80 μmol gFW^{-1} hr^{-1} and holding netA, starch, sucrose, and TCA fluxes constant. The simulated M0 mass isotopomers of RUBP were unchanged at different photorespiratory conditions. However, the higher mass isotopomers of RUBP were sensitive to variations in photorespiration flux. In particular, the differences in M2, M4, and M5 abundances appear to directly reflect the oxygenation flux. This makes the use of INST-MFA advantageous when determining intermediary fluxes from labeling data, in contrast to kinetic flux profiling (KFP), which uses only the washout kinetics of measured M0 mass isotopomers and requires measured pool size data to estimate fluxes [12,88].

This begs the question of how the M2 and M4 mass isotopomers of RUBP arise in these $^{13}CO_2$ labeling experiments. It is not trivial to trace out the expected patterns of isotope incorporation in individual metabolites because of the complex atom rearrangements that occur within the *Arabidopsis* metabolic network. The triose phosphate node alone has two potential routes for ^{13}C entry and 5 potential routes for labeling to exit. To address the underlying mechanism of the decreased labeling of M2 and M4 in low oxygenation situations, we examined the positional labeling of RUBP to see which carbons were most quickly labeled from oxygenation versus carboxylation (Figure 5.12). When

carboxylation occurs, two molecules of 3PGA are formed, with one of the 3PGA molecules coming directly from the last three carbons on RUBP and the other 3PGA molecule from the incorporated CO_2 and the first two carbons of RUBP. However, when oxygenation takes place, one 3PGA and one 2PG molecules are formed without CO_2 incorporation.

It was confirmed from simulating positional labeling of RUBP that the first two carbons (C1 and C2) label symmetrically, as well as the last two carbons (C4 and C5). C3 labels the fastest, which is consistent with the atom rearrangements that occur when CO_2 is incorporated through carboxylation and then goes through CBB cycle to regenerate more RUBP. This is because when carboxylation occurs, 3PGA is made up of either the last three carbons on RUBP or the first two carbons from RUBP with the fixed CO_2 incorporated in the first carbon position. This makes carboxylation have the effect of making C1 of 3PGA more enriched than the symmetrically labeled C2 and C3 carbons. On the other hand, since the carbons from 2PG come directly from the first two carbons on RUBP, it is expected that C1 and C2 on 2PG label up symmetrically as well, which is confirmed by simulating its positional labeling (Figure 5.10). When photorespiration occurs, the carbons from 2PG become the backbone of serine and are eventually recycled to form 3PGA. Therefore, photorespiration produces similar enrichments on all three carbons of 3PGA. As a result, M2 and M4 mass isotopomers of RUBP are more likely. On the other hand, M5 is less likely due to oxygenation competing against $^{13}CO_2$ incorporation by carboxylation.

Finally, we used our simulated M4 and M5 enrichments of RUBP to plot the M4/M5 ratio over time (Figure 5.13). Qualitatively speaking, the experimentally measured MIDs of RUBP in the five different labeling studies matched the expected order of M4/M5 ratios based on the model-estimated oxygenation values. The oxygenation flux was directly correlated with increasing M4/M5 ratios (Figure 5.13). This type of labeling signature of photorespiration could potentially serve as a screening tool for future transgenic lines to quickly determine low or high photorespiration rates without carrying out comprehensive metabolic flux analysis.

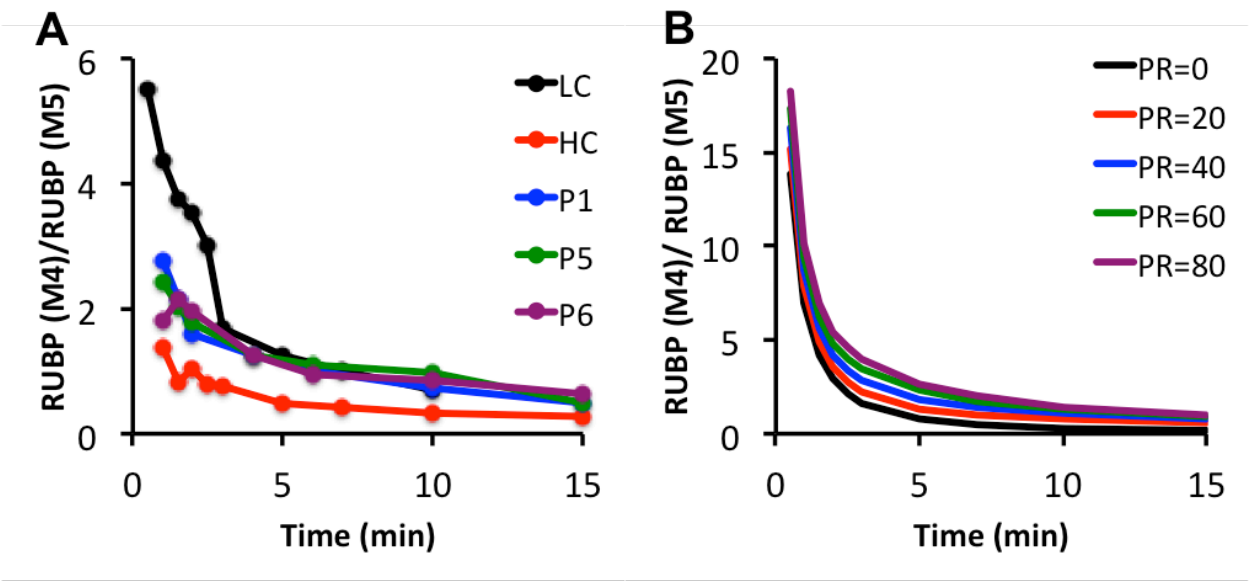

Figure 5.13. Mass isotopomer ratios of RUBP M4/M5.

Ratios are shown for (A) experimentally measured data and (B) computationally simulated data with varying photorespiration levels. Raw mass isotopomer data use in panel A are shown with correction for natural abundance.

5.5.3 RESPONSE OF PHOTOSYNTHETIC FLUXES TO OVEREXPRESSION OF A BACTERIAL CARBON ANHYDRASE

Similar to the HC plants, the BCA transgenic plants were capable of enhanced biomass, net CO_2 assimilation, and carboxylation rates. The enhanced labeling of the CBB cycle intermediates in the BCA plants supports the measured increase in netA, as well as the increase in absolute carboxylation flux. However, Vc:Vo ratios in the BCA plants were also at similar values to the LC plants and did not have the same expected increase observed under HC conditions. This points to a distinct mechanism of increased biomass in the BCA plants that is different from the HC plants, although the exact mechanism is still under investigation.

Unlike the HC plants, the labeling of photorespiratory intermediates in the BCA lines actually increased relative to LC plants. The rapid increase in labeling of glycine in the BCA lines might have been considered a consequence of small 2PG pool sizes. However, concentrations of photorespiratory intermediates (2PG, glycine, and serine) were found to be either comparable to those in the LC plants or slightly higher. And the labeling in serine was more variable as were glycine pool sizes such that insights prior to modeling could not be established. On the other hand, when estimated photorespiratory pool sizes from flux analysis were examined, it was noted that the 2PG and serine pool sizes in the BCA plants increased, while glycine pool sizes were estimated to decrease (Table 5A.5) in comparison to the LC plants. While these measured and estimated pool sizes may show conflicting results, it should be noted that most of the 95% confidence intervals for these model-estimated pool sizes exhibited overlap between the LC and BCA plants, thus

making direct comparisons complicated. Another possible explanation for the simultaneous increases in photorespiratory and carboxylation fluxes is that this reflects the growing recognition that photorespiration is important to metabolism for redistribution of reducing equivalents and production of some metabolites. Therefore, this pathway may function as more than a wasteful mechanism for detoxifying the cell of phosphoglycolate [191].

While the three BCA lines all had similar estimated carboxylation and oxygenation rates at both an absolute and relative flux scale, the starch production flux showed an inverse correlation with sucrose production, with BCA-P1 showing high starch accumulation and BCA-P6 showing similar levels to that of the LC plants. This difference in estimated starch production among the three lines also inversely correlated with BCA expression levels. It appears that the line with the most BCA overexpression, BCA-P6, was capable of overcoming the feedback inhibition that limited sucrose export in the HC plants and to an extent, the BCA-P1 and BCA-P5 plants. It is possible that the transgenic lines that must adjust developmentally to the perturbation from the time of germination have an adaptive strategy that balances carbon to nitrogen (C:N) and results in improved growth without dramatically altering Vc:Vo or reducing the flux through photorespiration. While the RuBisCO content in the HC plants was decreased, the RuBisCO content in the BCA lines were similar to the LC plants. Since RuBisCO can account for up to approximately 50% of leaf soluble protein and 25% of leaf nitrogen, this increase in carboxylation associated with unchanged levels of RuBisCO suggests that these transgenic lines have adapted a better strategy to maintain an optimal C:N ratio.

One other possible hypothesis for differences between the BCA and HC plants is that the overexpression of carbonic anhydrase leads to a change in pH in the chloroplast stroma, where the enzymes of the CBB cycle are located. An increase in BCA overexpression can increase the CO_2 levels in the stroma, which can decrease the pH, contributing to the activation of certain Calvin cycle enzymes, such as RuBisCO, FBPase, SBPase, and PRK.

A full understanding of how photosynthetic efficiency can be increased via a fully reconstituted functional CCM complex in C3 plants is underway. The addition of the two bicarbonate transporters to the transgenic BCA plant lines could potentially improve photosynthetic efficiency even more, thus providing an important basis for engineering increased crop yield in the future. Further investigation of these proposed transgenic lines using ^{13}C flux analysis can help confirm the photosynthetic fluxes associated with source and sink metabolism, as well as point out unexpected impacts on intermediary metabolism.

5.6 ACKNOWLEDGEMENTS

This work was supported by the following grants: NSF (EF-1105249), GAANN (P200A090323), DOE (DE-AC05-06OR23100) and the USDA-ARS. I am very thankful for Dick Sayre and Sowmya Subramanian at Los Alamos National Laboratory for creating the transgenic BCA lines and for Doug Allen and Fangfang Ma for growing and performing the ^{13}C labeling experiments on the HC and BCA lines.

5.7 APPENDIX: SUPPLEMENTAL TABLES

Table 5A.1. Net fluxes determined by INST-MFA.

Values are absolute fluxes (μmol metabolites gFW^{-1} hr^{-1}) based on the measured net CO_2 uptake rate. Estimated flux values and 95% confidence bounds are shown (SEM; LC, n=6; HC, n=5; BCA-P1, BCA-P5, BCA-P6, n=3).

	LC			HC			BCA-P1			BCA-P5			BCA-P6		
Reaction	**Value**	LB95	UB95	**Value**	LB95	UB95	**Value**	LB95	UB95	**Value**	LB95	UB95	**Value**	LB95	UB95
Calvin cycle															
RUBP.p + CO2 → 3PGA.p + 3PGA.p	**135.1**	110.3	160.4	**145.4**	133.5	159.4	**175.2**	154.4	196.1	**174.1**	159.8	188.4	**186.8**	178.9	194.3
TP.p + E4P.p → SBP	**57.9**	47.1	69.0	**49.3**	45.1	54.9	**75.4**	66.3	84.5	**75.4**	69.1	81.6	**79.0**	75.3	82.6
SBP → S7P.p	**57.9**	47.1	69.0	**49.3**	45.1	54.9	**75.4**	66.3	84.5	**75.4**	69.1	81.6	**79.0**	75.3	82.6
TP.p + EC2 ↔ X5P.p	**115.8**	94.3	138.1	**98.7**	90.2	109.8	**150.8**	132.6	169.1	**150.8**	138.2	163.3	**158.0**	150.7	165.1
S7P.p ↔ R5P.p + EC2	**57.9**	47.1	69.0	**49.3**	45.1	54.9	**75.4**	66.3	84.5	**75.4**	69.1	81.6	**79.0**	75.3	82.6
F6P.p ↔ E4P.p + EC2	**57.9**	47.1	69.0	**49.3**	45.1	54.9	**75.4**	66.3	84.5	**75.4**	69.1	81.6	**79.0**	75.3	82.6
X5P.p ↔ RU5P.p	**115.8**	94.3	138.1	**98.7**	90.2	109.8	**150.8**	132.6	169.1	**150.8**	138.2	163.3	**158.0**	150.7	165.1
R5P.p ↔ RU5P.p	**57.9**	47.1	69.0	**49.3**	45.1	54.9	**75.4**	66.3	84.5	**75.4**	69.1	81.6	**79.0**	75.3	82.6
RU5P.p → RUBP.p	**173.7**	141.4	207.1	**148.0**	135.3	164.7	**226.2**	198.9	253.6	**226.2**	207.3	244.9	**236.9**	226.0	247.7
Photorespiration															
RUBP.p → 3PGA.p + 2PG.p	**38.6**	30.6	47.8	**2.6**	0.0	8.3	**50.9**	44.2	57.9	**52.1**	47.0	57.2	**50.2**	45.7	54.4
2PG.p → GLY.p	**38.6**	30.6	47.8	**2.6**	0.0	8.3	**50.9**	44.2	57.9	**52.1**	47.0	57.2	**50.2**	45.7	54.4
GLY.p ↔ GLY.x + GLYout	**0.1**	0.0	0.1	**0.0**	0.0	0.0	**0.0**	0.0	0.0	**0.0**	0.0	0.1	**0.1**	0.1	0.1

Table 5A.1. Continued

GLY.p + GLY.p → SER.p + CO2	**19.3**	15.2	23.9	**1.3**	0.0	4.1	**25.5**	22.1	28.9	**26.0**	23.6	28.5	**25.0**	22.9	27.2
SER.p ↔ SER.x + SERout	**0.2**	0.1	0.3	**0.0**	0.0	0.1	**0.1**	0.1	0.1	**0.1**	0.1	0.2	**0.2**	0.2	0.2
SER.p → GA.p	**19.1**	15.1	23.6	**1.2**	0.0	4.1	**25.3**	22.0	28.8	**25.9**	23.4	28.4	**24.9**	22.6	27.0
GA.p ↔ 3PGA.p	**19.1**	15.1	23.6	**1.2**	0.0	4.1	**25.3**	22.0	28.8	**25.9**	23.4	28.4	**24.9**	22.6	27.0
Starch Synthesis															
3PGA.p → TP.p	**325.4**	265.4	387.2	**294.2**	268.8	325.7	**425.5**	374.9	476.0	**424.4**	388.9	459.6	**446.2**	425.6	465.7
TP.p + TP.p ↔ FBP.p	**64.2**	53.4	75.3	**69.8**	62.4	77.9	**89.2**	79.9	98.6	**85.0**	78.1	91.8	**85.6**	81.3	89.5
FBP.p ↔ F6P.p	**64.2**	53.4	75.3	**69.8**	62.4	77.9	**89.2**	79.9	98.6	**85.0**	78.1	91.8	**85.6**	81.3	89.5
F6P.p ↔ G6P.p	**6.3**	5.7	6.8	**20.5**	14.8	24.8	**13.8**	11.4	16.2	**9.6**	7.0	12.1	**6.6**	5.0	8.2
G6P.p ↔ G1P.p	**6.3**	5.7	6.8	**20.5**	14.8	24.8	**13.8**	11.4	16.2	**9.6**	7.0	12.1	**6.6**	5.0	8.2
G1P.p → ADPG	**6.3**	5.7	6.8	**20.5**	14.8	24.8	**13.8**	11.4	16.2	**9.6**	7.0	12.1	**6.6**	5.0	8.2
Sucrose Synthesis															
TP.c + TP.c ↔ FBP.c	**11.7**	8.4	14.9	**3.3**	0.0	9.2	**10.5**	6.9	14.0	**14.1**	11.1	17.2	**19.1**	17.2	20.9
FBP.c ↔ F6P.c	**11.7**	8.4	14.9	**3.3**	0.0	9.2	**10.5**	6.9	14.0	**14.1**	11.1	17.2	**19.1**	17.2	20.9
F6P.c ↔ G6P.c	**5.8**	4.2	7.5	**1.7**	0.0	4.6	**5.2**	3.5	7.0	**7.1**	5.6	8.6	**9.5**	8.6	10.5
G6P.c ↔ G1P.c	**5.8**	4.2	7.5	**1.7**	0.0	4.6	**5.2**	3.5	7.0	**7.1**	5.6	8.6	**9.5**	8.6	10.5
G1P.c ↔ UDPG	**5.8**	4.2	7.5	**1.7**	0.0	4.6	**5.2**	3.5	7.0	**7.1**	5.6	8.6	**9.5**	8.6	10.5
F6P.c + UDPG → S6P	**5.8**	4.2	7.5	**1.7**	0.0	4.6	**5.2**	3.5	7.0	**7.1**	5.6	8.6	**9.5**	8.6	10.5
TCA cycle															
3PGA.c ↔ PEP.c	**2.5**	1.8	3.2	**0.4**	0.0	1.1	**1.3**	0.9	1.7	**1.7**	1.4	2.1	**2.3**	2.1	2.6
PEP.c → PYR.c	**1.1**	0.8	1.4	**0.2**	0.0	0.6	**0.6**	0.4	0.9	**0.9**	0.7	1.1	**1.2**	1.1	1.3
PYR.c + dummy → ACA + CO2	**0.9**	0.7	1.2	**0.2**	0.0	0.4	**0.5**	0.3	0.6	**0.6**	0.5	0.8	**0.9**	0.8	1.0
OAA + ACA → CIT	**0.9**	0.7	1.2	**0.2**	0.0	0.4	**0.5**	0.3	0.6	**0.6**	0.5	0.8	**0.9**	0.8	1.0
CIT ↔ ICI	**0.9**	0.7	1.2	**0.2**	0.0	0.4	**0.5**	0.3	0.6	**0.6**	0.5	0.8	**0.9**	0.8	1.0
ICI + dummy → AKG + CO2	**0.9**	0.7	1.2	**0.2**	0.0	0.4	**0.5**	0.3	0.6	**0.6**	0.5	0.8	**0.9**	0.8	1.0
MAL ↔ OAA	**0.0**	0.0	0.0	**0.0**	0.0	0.0	**0.0**	0.0	0.0	**0.0**	0.0	0.0	**0.0**	0.0	0.0

Table 5A.1. Continued

Anaplerotic															
PEP.c + CO2 → OAA + dummy	**1.4**	1.0	1.7	**0.2**	0.0	0.6	**0.6**	0.4	0.9	**0.9**	0.7	1.1	**1.2**	1.1	1.3
Amino Acids															
PYR.c → ALA.c	**0.2**	0.1	0.2	**0.1**	0.0	0.1	**0.2**	0.1	0.2	**0.2**	0.2	0.3	**0.3**	0.3	0.3
OAA → ASP	**0.4**	0.3	0.5	**0.1**	0.0	0.1	**0.2**	0.1	0.2	**0.2**	0.2	0.3	**0.3**	0.3	0.3
AKG → GLU	**0.9**	0.7	1.2	**0.2**	0.0	0.4	**0.5**	0.3	0.6	**0.6**	0.5	0.8	**0.9**	0.8	1.0
GLU ↔ PRO	**0.0**	0.0	0.0	**0.0**	0.0	0.0	**0.0**	0.0	0.0	**0.0**	0.0	0.0	**0.0**	0.0	0.0
GLU ↔ GLN	**0.0**	0.0	0.0	**0.0**	0.0	0.0	**0.0**	0.0	0.0	**0.0**	0.0	0.0	**0.0**	0.0	0.0
ASP ↔ THR	**0.0**	0.0	0.0	**0.0**	0.0	0.0	**0.0**	0.0	0.0	**0.0**	0.0	0.0	**0.0**	0.0	0.0
ASP ↔ ASN	**0.0**	0.0	0.0	**0.0**	0.0	0.0	**0.0**	0.0	0.0	**0.0**	0.0	0.0	**0.0**	0.0	0.0
S6P + α(GLU) + β(ASP) + γ(ALA.c) + δ(GLYout) + ε(SERout) → Sink	**5.8**	4.2	7.5	**1.7**	0.0	4.6	**5.2**	3.5	7.0	**7.1**	5.6	8.6	**9.5**	8.6	10.5
Transporters															
3PGA.p ↔ 3PGA.c	**2.5**	1.8	3.2	**68.1**	45.0	89.9	**63.2**	0.0	69.9	**56.5**	0.0	60.8	**47.0**	38.0	55.9
TP.p ↔ TP.c	**23.3**	16.9	29.9	**23.6**	0.8	47.6	**36.1**	28.8	100.0	**43.5**	39.3	100.0	**52.9**	43.0	62.2

Note: α, β, γ, δ, and ε are measured ratios of output fluxes in amino acids and sucrose

Table 5A.2. Exchange fluxes determined by INST-MFA.

Values are scaled according to the transformation $V_{exch} = 100 \times V_{exch}/(V_{exch} + V_{ref})$ where V_{ref} is the net CO_2 uptake flux. The exchange flux is the minimum of the forward and backward fluxes of a reversible reaction. Estimated flux values and 95% confidence bounds are shown.

	LL			HC			BCA-P1			BCA-P5			BCA-P6		
Reaction	**Value**	LB95	UB95	**Value**	LB95	UB95	**Value**	LB95	UB95	**Value**	LB95	UB95	**Value**	LB95	UB95
Calvin cycle															
TP.p + EC2 ↔ X5P.p	**-**	0.0	100.0	**-**	0.0	100.0	**32.4**	0.0	100.0	**-**	0.0	100.0	**-**	0.0	100.0
S7P.p ↔ R5P.p + EC2	**20.5**	14.8	26.4	**-**	0.0	100.0	**9.6**	0.0	100.0	**-**	0.0	100.0	**-**	0.0	100.0
F6P.p ↔ E4P.p + EC2	**0.0**	0.0	2.8	**0.0**	0.0	7.0	**0.0**	0.0	26.2	**0.0**	0.0	4.5	**0.0**	0.0	9.6
X5P.p ↔ RU5P.p	**49.5**	0.0	70.2	**0.8**	0.0	8.4	**0.0**	0.0	9.7	**0.0**	0.0	12.7	**0.0**	0.0	5.2
R5P.p ↔ RU5P.p	**59.8**	44.3	75.4	**0.0**	0.0	17.0	**0.0**	0.0	47.7	**0.0**	0.0	44.6	**0.0**	0.0	37.3
Photorespiration															
GLY.p ↔ GLY.x + GLYout	**3.9**	2.1	5.8	**0.3**	0.0	1.6	**3.2**	2.2	4.4	**2.4**	1.3	3.5	**4.3**	2.7	6.1
SER.p ↔ SER.x + SERout	**3.3**	0.8	6.3	**0.0**	0.0	4.1	**2.7**	1.6	3.9	**2.4**	0.9	3.8	**2.8**	0.7	5.1
GA.p ↔ 3PGA.p	**19.4**	14.1	26.2	**2.5**	0.0	7.6	**4.1**	2.9	5.0	**1.9**	1.3	2.6	**1.9**	0.9	3.6
Starch Synthesis															
TP.p + TP.p ↔ FBP.p	**-**	0.0	100.0	**0.0**	0.0	5.2	**55.3**	5.3	89.8	**12.4**	0.0	37.8	**0.0**	0.0	17.2
FBP.p ↔ F6P.p	**-**	0.0	100.0	**100.0**	89.4	100.0	**100.0**	93.0	100.0	**-**	0.0	100.0	**-**	65.3	100.0
F6P.p ↔ G6P.p	**1.4**	0.0	13.4	**6.7**	0.0	16.8	**0.0**	0.0	2.0	**0.0**	0.0	1.0	**0.0**	0.0	1.6
G6P.p ↔ G1P.p	**99.9**	9.8	100.0	**-**	0.0	100.0	**-**	0.0	100.0	**-**	0.0	100.0	**-**	0.0	100.0

Table 5A.2. Continued

Sucrose Synthesis															
TP.c + TP.c ↔ FBP.c	**23.5**	11.7	37.7	**17.3**	10.2	33.3	**2.0**	1.0	4.4	**3.2**	2.2	5.0	**1.3**	0.0	3.2
FBP.c ↔ F6P.c	**15.7**	9.1	40.0	**9.4**	5.0	16.9	**3.4**	1.3	8.4	**2.3**	0.0	5.8	**4.2**	0.0	19.4
F6P.c ↔ G6P.c	**67.6**	20.2	100.0	**100.0**	15.8	100.0	**-**	0.0	100.0	**-**	15.4	100.0	**10.9**	3.3	55.0
G6P.c ↔ G1P.c	**99.8**	40.4	100.0	**22.8**	9.5	100.0	**-**	0.0	100.0	**-**	0.0	100.0	**-**	16.9	100.0
G1P.c ↔ UDPG	**71.6**	42.1	100.0	**91.2**	11.9	100.0	**-**	0.0	100.0	**-**	0.0	100.0	**-**	22.8	100.0
TCA cycle															
3PGA.c ↔ PEP.c	**-**	0.0	100.0	**-**	0.0	100.0	**-**	0.0	100.0	**-**	0.7	100.0	**-**	0.0	100.0
CIT ↔ ICI	**-**	0.0	100.0	**-**	0.0	100.0	**-**	0.0	100.0	**-**	0.0	100.0	**26.6**	5.1	88.5
MAL ↔ OAA	**0.0**	0.0	0.7	**0.0**	0.0	0.5	**0.0**	0.0	10.5	**0.0**	0.0	4.5	**3.5**	0.0	17.7
Amino Acids															
GLU ↔ PRO	**-**	0.0	100.0	**-**	0.0	100.0	**-**	0.0	100.0	**-**	0.0	100.0	**-**	0.0	100.0
GLU ↔ GLN	**-**	0.0	100.0	**-**	0.0	100.0	**-**	0.0	100.0	**-**	0.0	100.0	**-**	0.0	100.0
ASP ↔ THR	**0.0**	0.0	0.2	**0.0**	0.0	0.1	**0.0**	0.0	0.9	**0.0**	0.0	1.2	**0.0**	0.0	5.6
ASP ↔ ASN	**0.0**	0.0	0.2	**-**	0.0	100.0	**0.0**	0.0	0.9	**0.1**	0.0	8.0	**0.1**	0.0	10.4
Transporters															
3PGA.p ↔ 3PGA.c	**-**	0.0	100.0	**0.0**	0.0	6.6	**0.0**	0.0	3.0	**0.0**	0.0	3.2	**0.0**	0.0	2.5
TP.p ↔ TP.c	**23.6**	9.0	36.2	**38.6**	21.5	51.4	**0.0**	0.0	8.8	**0.0**	0.0	5.7	**0.0**	0.0	15.7

Table 5A.3. Subcellular contribution parameters determined by INST-MFA.

The estimated lower and upper 95% confidence bounds of subcellular contributions of metabolites spatially separated in the plastid and cytosol are shown below as percentages of the contribution towards total labeling.

	LL		HC		BCA-P1		BCA-P5		BCA-P6	
Subcellular Compartmentation, %	LB95	UB95	LB95	UB95	LB95	UB95	LB95	UB95	LB95	UB95
3PGA.p	0.0	93.6	45.0	89.9	0.0	69.9	0.0	60.8	38.0	55.9
3PGA.c	0.0	94.5	0.8	47.6	28.8	100.0	39.3	100.0	43.0	62.2
DHAP.p	6.5	62.9	0.0	49.4	0.0	69.9	0.0	25.9	0.0	41.4
DHAP.c	27.6	88.0	46.9	100.0	26.5	100.0	70.7	100.0	52.2	97.9
F6P.p	29.8	56.3	32.6	50.4	31.7	48.5	35.8	47.3	16.6	38.1
F6P.c	27.6	55.2	30.2	66.2	43.8	64.7	45.1	59.1	42.2	66.9
FBP.p	0.0	27.7	0.0	47.1	5.6	42.9	12.8	30.4	0.0	21.3
FBP.c	56.3	87.1	47.5	100.0	50.7	90.1	59.7	80.2	70.5	95.0
G1P.p	0.0	15.7	7.9	13.8	3.4	30.2	6.3	23.3	0.0	10.3
G1P.c	31.5	51.8	24.8	71.3	24.1	56.4	30.2	52.4	25.6	69.0
G6P.p	5.8	27.2	0.0	23.9	0.0	47.3	14.1	32.1	0.0	22.9
G6P.c	49.1	72.9	55.9	100.0	35.5	82.5	50.8	73.9	49.4	73.1
RU5P.p	0.0	65.1	62.7	90.4	0.0	98.6	37.6	86.3	0.0	24.9
X5P.p	28.0	94.2	0.0	26.2	0.0	99.5	8.8	58.2	61.5	90.3
R5P.p	80.8	83.8	73.7	80.1	84.2	88.6	0.0	100.0	77.7	88.5
GA.p	68.3	78.6	75.7	100.0	96.8	100.0	81.8	95.4	96.1	100.0
SER.p	52.6	67.1	30.9	100.0	64.9	77.9	72.3	83.3	75.0	92.1
GLY.p	33.3	40.4	10.7	15.6	64.8	74.8	77.4	82.8	71.7	84.3
RUBP.p	91.1	94.0	89.9	93.6	93.9	97.3	92.6	95.5	90.0	94.0
S7P.p	97.2	99.8	92.8	97.1	96.6	99.8	96.6	99.3	95.0	99.7
2PG.p	85.4	88.8	65.4	71.5	84.7	91.4	88.9	93.8	84.7	90.4
ADPG.p	94.0	96.3	85.6	93.7	90.3	100.0	90.8	100.0	92.0	100.0
PEP.c	87.6	90.9	79.6	85.2	85.8	96.6	85.3	90.0	89.5	93.9

Table 5A.3 .Continued

UDPG.c	67.4	78.6	64.7	100.0	76.2	94.2	80.5	94.3	60.8	92.3
ALA.c	28.5	34.4	29.4	60.5	9.2	100.0	12.9	100.0	11.5	100.0
SBP.p			79.2	84.3	91.1	97.3	91.5	95.3	84.8	93.6

Table 5A.4. Dilution parameters determined by INST-MFA.

Dilution parameters represent the percentage of the total sampled pool that is metabolically active, which is equivalent to the 1-G parameter introduced by Kelleher and Masterson [131]. Median parameter estimates and 95% confidence bounds are shown.

	LC			HC			BCA-P1			BCA-P5			BCA-P6		
Dilution Parameters, %	**Value**	LB95	UB95	**Value**	LB95	UB95	**Value**	LB95	UB95	**Value**	LB95	UB95	**Value**	LB95	UB95
3PGA	**7.1**	5.5	8.6	**8.3**	5.5	10.6	**0.6**	0.0	2.7	**0.0**	0.0	0.6	**0.1**	0.0	2.9
DHAP	**7.5**	4.2	10.2	**0.0**	0.0	6.5	**1.4**	0.0	4.5	**2.6**	0.0	5.1	**5.4**	2.1	8.5
FGP	**14.8**	11.4	17.7	**8.9**	0.0	25.1	**5.1**	0.0	11.3	**6.4**	0.8	10.8	**18.9**	8.7	25.5
FBP	**16.5**	12.9	19.6	**1.1**	0.0	11.0	**5.3**	0.4	9.6	**8.9**	3.5	13.6	**6.9**	1.1	11.7
G1P	**50.2**	45.9	54.2	**43.6**	20.8	67.8	**43.0**	37.0	48.0	**43.9**	38.8	48.5	**53.7**	31.8	68.8
G6P	**22.1**	17.7	25.8	**8.7**	0.0	34.3	**15.0**	8.0	20.5	**14.6**	8.4	19.7	**26.5**	11.1	34.5
RU5P	**7.2**	5.8	8.5	**11.4**	9.2	13.5	**3.7**	0.5	6.8	**4.4**	2.8	6.0	**13.8**	9.8	17.7
R5P	**17.7**	16.2	19.2	**23.2**	19.9	26.3	**13.6**	11.5	15.8	**-**	0.0	100.0	**17.0**	11.5	22.3
GA	**27.0**	21.4	31.7	**17.0**	0.0	24.3	**0.0**	0.0	3.2	**11.7**	4.6	18.2	**0.0**	0.0	3.9
SER	**40.7**	32.9	47.4	**59.7**	0.0	69.1	**28.6**	22.1	35.1	**22.4**	16.7	27.7	**17.3**	7.9	25.0
GLY	**63.2**	59.6	66.7	**87.0**	84.4	89.3	**30.3**	25.2	35.2	**20.0**	17.2	22.6	**22.3**	15.7	28.3
RUBP	**7.5**	6.0	8.9	**8.4**	6.4	10.1	**4.3**	2.7	6.1	**6.0**	4.5	7.4	**8.0**	6.0	10.0
S7P	**1.5**	0.2	2.8	**5.3**	2.9	7.2	**1.9**	0.2	3.4	**2.1**	0.7	3.4	**2.7**	0.3	5.0
2PG	**13.0**	11.2	14.6	**31.5**	28.5	34.6	**12.1**	8.6	15.3	**8.7**	6.2	11.1	**12.6**	9.6	15.3
ADPG	**4.9**	3.7	6.0	**10.5**	6.3	14.4	**0.6**	0.0	9.7	**1.5**	0.0	9.2	**2.7**	0.0	8.0
PEP	**10.8**	9.1	12.4	**17.8**	14.8	20.4	**9.0**	3.4	14.2	**12.4**	10.0	14.7	**8.4**	6.1	10.5
UDPG	**27.6**	21.4	32.6	**0.0**	0.0	35.3	**16.4**	5.8	23.8	**13.7**	5.7	19.5	**27.3**	7.7	39.2
ALA	**68.8**	65.6	71.5	**61.0**	39.5	70.6	**50.1**	0.0	90.8	**75.8**	0.0	87.1	**77.0**	0.0	88.5
SBP				**18.2**	15.7	20.8	**5.9**	2.7	8.9	**6.7**	4.7	8.5	**10.9**	6.4	15.2

Table 5A.5. Pool sizes determined by INST-MFA.

Identifiable pool sizes are those with both nonzero lower and finite upper bounds on their 95% confidence interval. Bounded pool sizes are those with a finite upper bound but with zero lower bound. 95% confidence bounds are shown. Pool sizes units in nmol/gFW.

	LL		HC		BCA-P1		BCA-P5		BCA-P6	
Pool	LB95	UB95	LB95	UB95	LB95	UB95	LB95	UB95	LB95	UB95
2PG.p	0.0	13.4	0.1	62.7	83.2	348.5	285.6	458.1	126.7	366.9
3PGA.c	0.0	83.0	0.0	72.8	0.0	102.5	0.0	44.0	0.0	114.1
3PGA.p	0.0	81.8	0.0	65.1	0.0	132.2	0.0	84.2	0.0	388.0
ACA	0.0	Inf	0.0	Inf	0.0	Inf	0.0	Inf	0.0	Inf
ADPG.p	0.0	14.9	0.0	52.6	0.0	418.7	0.0	40.3	0.0	169.5
AKG	0.0	Inf	0.0	Inf	0.0	Inf	0.0	Inf	0.0	Inf
ALA.c	10.5	20.1	0.0	20.5	0.0	293.0	0.0	1.7	0.0	8.0
ASN	0.0	Inf	0.0	181.2	0.0	Inf	0.0	Inf	0.0	Inf
ASP	304.8	687.5	0.0	3.4	0.0	322.0	9.9	864.1	34.7	2189.8
CIT	0.0	Inf	0.0	Inf	0.0	19816.6	0.0	Inf	0.0	11745.7
CO2	1141.5	1745.2	456.9	771.3	423.6	796.9	453.5	716.0	1139.7	1698.5
F6P.c	0.0	1906.4	0.0	1701.1	0.0	906.9	0.0	1218.5	0.0	222.1
F6P.p	0.0	54.9	0.0	36.9	0.0	94.5	0.0	48.7	0.0	246.5
FBP.c	0.0	43.2	18.7	335.8	73.5	316.1	295.8	572.2	243.2	483.6
FBP.p	0.0	55.7	0.0	39.3	0.0	101.3	0.0	49.0	0.0	247.1
G1P.c	0.0	933.0	0.0	4227.4	0.0	420.0	0.0	378.4	0.0	1327.8
G1P.p	0.0	158.5	0.0	151.1	0.0	231.1	0.0	152.7	0.0	76.6
G6P.c	0.0	911.1	0.0	1702.2	0.0	1025.2	0.0	1301.4	0.0	1946.0
G6P.p	0.0	159.4	136.9	400.1	0.0	636.3	0.0	430.3	0.0	173.7
GA.p	0.0	66.9	0.0	48.3	0.0	203.6	0.0	75.5	0.0	411.6
GLN	0.0	Inf	0.0	Inf	0.0	Inf	0.0	Inf	0.0	Inf

Table 5A.5. Continued

GLU	0.0	Inf	0.0	Inf	0.0	Inf	0.0	Inf	0.0	Inf
GLY.p	568.5	1013.1	0.0	44.0	220.5	680.8	151.3	327.8	319.4	751.0
ICI	0.0	Inf	0.0	Inf	0.0	Inf	0.0	Inf	2337.1	Inf
MAL	0.0	2925.3	0.0	Inf	0.0	Inf	0.0	Inf	0.0	Inf
OAA	0.0	11.3	0.0	817.5	83.8	2626.0	40.8	3465.5	0.0	277.3
PEP.c	0.0	73.1	0.0	74.0	0.0	79.8	0.0	77.3	0.0	117.4
PRO	0.0	Inf	0.0	Inf	0.0	Inf	0.0	Inf	0.0	Inf
PYR.c	0.0	1.0	0.0	2.9	0.0	1313.3	107.7	1543.7	107.2	2425.8
R5P.p	809.6	1245.9	0.0	26.0	0.0	363.0	0.0	87.4	0.0	113.2
RU5P.p	0.0	36.3	0.0	25.9	0.0	279.0	0.0	84.7	0.0	114.2
RUBP.p	0.0	19.2	0.0	21.6	0.0	74.4	0.0	76.1	0.0	89.8
S7P.p	0.0	36.8	0.0	9.4	0.0	46.1	0.0	18.0	0.0	23.6
SBP.p			238.2	384.7	109.5	288.3	162.5	264.0	154.5	355.5
SER.p	399.7	891.2	0.5	1279.1	811.0	1362.1	1732.2	2307.5	2257.4	3425.5
THR	0.0	Inf	0.0	Inf	0.0	Inf	0.0	Inf	0.0	Inf
TP.c	0.0	72.3	0.0	186.6	0.0	276.3	0.0	34.4	15.1	199.0
TP.p	0.0	88.2	0.0	66.3	0.0	201.4	0.0	101.2	0.0	491.5
UDPG.c	0.0	1956.3	1228.7	5723.1	0.0	661.8	0.0	1056.7	0.0	1946.1
X5P.p	0.0	35.3	554.9	817.9	311.9	762.4	620.5	819.1	499.6	803.5

6. CONCLUSIONS AND FUTURE WORK

6.1 CONCLUSIONS

The work presented in this dissertation further advances the application of the relatively young flux analysis tool, isotopically nonstationary metabolic flux analysis (INST-MFA), to photoautotrophic systems. These cyanobacterial and plant systems have attracted a lot of interest in recent years as hosts for the production of renewable fuels and chemicals. As such, it is important to gain a better *in vivo* understanding of the metabolic state of these systems, especially ones with altered capabilities due to either environmental or genetic perturbations. Our contributions show how INST-MFA provides a way for us peek inside the black box of host cell metabolism and generate rational strain engineering targets to characterize non-model host organisms, as well as identify and subsequently eliminate wasteful byproduct pathways or metabolic bottlenecks.

Shortly after the dynamic theory of metabolic isotopomer labeling systems was established over a decade ago [192], the experimental concept of isotopically nonstationary labeling experiments was proposed and since then, there have only been a few fully quantitative applications of INST-MFA to diverse biological systems [6,20,46,193–199], with only one application to a fully photoautotrophic cyanobacterial system [6]. Our work, along with the existing literature reviewed in Chapter 2, validates the usefulness of INST-MFA as an effective tool for subsequent strain engineering in photoautotrophic systems.

In Chapter 3, we investigated the photoautotrophic metabolism of wild-type *Synechococcus elongatus* PCC 7942 and a derivative strain engineered to produce isobutyraldehyde heterologously. Using INST-MFA, we elucidated a bottleneck at the pyruvate node and identified a potential pyruvate kinase (PK) bypass pathway. This led to the generation of six overexpression strains that all had significantly improved isobutyraldehyde production rates, with the double overexpression strain of malate dehydrogenase (MDH) and malic enzyme (ME) showing the most improved productivity by 68% compared to the parental isobutyraldehyde strain.

Chapter 4 builds on the metabolic network developed in the previous chapter for a cyanobacterial system and describes a more complex system in *Arabidopsis thaliana* leaves with compartmentalized fluxes. INST-MFA was employed for the first time to a terrestrial plant system *in planta* to generate metabolic flux maps for *Arabidopsis* leaves at two different light intensities. The resulting comprehensive flux maps showed increases in carbon partitioning towards sucrose and away from starch as light intensity was increased. Additionally, flux analysis revealed that despite a doubling in the carboxylation rate, the photorespiratory flux increased from 17 to 28% of net CO_2 assimilation when grown under high light conditions. This study highlights the potential for INST-MFA to describe emergent flux phenotypes in response to environmental and genetic perturbations that cannot be obtained by other complementary approaches.

Finally, in Chapter 5 we used the same *Arabidopsis* metabolic network and further applied the INST-MFA methodology to leaves exposed to both environmental and genetic perturbations. The metabolic response of wild-type *Arabidopsis* leaves exposed to high CO2 conditions was examined, as well as the responses of three transgenic lines engineered with a bacterial carbonic anhydrase (BCA) at ambient CO2 condtions. The BCA plants were engineered as a first step towards a fully recapitulated algal carbon concentrating mechanism in a C3 plant to increase photosynthetic efficiency. Flux analysis revealed that the plants grown under high CO2 had higher carboxylation flux and had lowered oxygenation flux, as expected. Additionally, there was a dramatic increase towards starch production in the high CO2 conditions. Furthermore, the BCA plants had an inverse correlation with starch production and BCA expression and although these plants had increased carboxylation flux, there was also an unexpected increase in absolute oxygenation flux. Finally, simulation studies pointed to the labeling patterns of the metabolite RUBP as a key indicator of photorespiratory flux and will be useful for screening purposes in future transgenic lines. Overall, these flux analysis results will assist further rounds of plant metabolic engineering and will ultimately lead to improve photosynthetic efficiency of C3 plants.

6.2 RECOMMENDATION FOR FUTURE WORK

Although the studies detailed in this dissertation are complete, there is room for more work to be accomplished. While Chapter 3 details the work surrounding one full turn through the metabolic engineering cycle leading to significant increases in isobutyraldehyde productivity in cyanobacteria, INST-MFA should be applied again to

the top performing strains (IBA/PYK^{ox} and IBA/MoM^{ox}) to verify the anticipated redistribution of fluxes surrounding the pyruvate node. Since pyruvate serves as a major branch node in central carbon metabolism, increasing flux towards pyruvate may have also inadvertently increased flux towards other alternate carbon sinks, such as amino acid biosynthesis, TCA cycle, and lipid biosytneshis pathways, thereby limiting isobutyraldehdye production. This can potentially identify knockdown or deletion targets for further strain engineering so that increases in carbon product formation can be directly solely towards isobutyraldehyde.

Furthermore, the work in Chapter 5 pointed to an unexpected increase in absolute oxygenation flux in the transgenic BCA plants. Although this is outside the scope of expertise in our lab, further work should be done by our collaborators to determine why overexpression of bacterial carbonic anhydrase led to this unexpected increase in oxygenation flux, even though carboxylation flux was successfully increased. Our preliminary hypothesis is that overexpression of BCA led to changes in pH in the plant leaves, which increased activity of key enzymes in the Calvin cycle. Additionally, our collaborators have been working on generating transgenic plants expressing genes involved with an algal carbon concentrating mechanism – INST-MFA should be performed on these transgenic plants to assess the alterations in carbon partitioning, as well as to identify any unexpected metabolic flux redistributions.

LIST OF REFERENCES

1. Nozzi NE, Oliver JWK, Atsumi S: **Cyanobacteria as a Platform for Biofuel Production**. *Front. Bioeng. Biotechnol.* 2013, **1**:1–6.

2. Wilson SA, Roberts SC: **Metabolic engineering approaches for production of biochemicals in food and medicinal plants**. *Curr. Opin. Biotechnol.* 2014, **26**:174–182.

3. Sauer U: **Metabolic networks in motion: 13C-based flux analysis.** *Mol. Syst. Biol.* 2006, **2**:62.

4. Wiechert W, Nöh K: **Isotopically non-stationary metabolic flux analysis: Complex yet highly informative**. *Curr. Opin. Biotechnol.* 2013, **24**:979–986.

5. Shastri AA, Morgan JA: **A transient isotopic labeling methodology for 13C metabolic flux analysis of photoautotrophic microorganisms.** *Phytochemistry* 2007, **68**:2302–12.

6. Young JD, Shastri AA, Stephanopoulos G, Morgan JA: **Mapping photoautotrophic metabolism with isotopically nonstationary (13)C flux analysis.** *Metab. Eng.* 2011, **13**:656–665.

7. Yang C: **Metabolic Flux Analysis in Synechocystis Using Isotope Distribution from 13C-Labeled Glucose**. *Metab. Eng.* 2002, **4**:202–216.

8. Schwender J: **Metabolic flux analysis as a tool in metabolic engineering of plants.** *Curr. Opin. Biotechnol.* 2008, **19**:131–7.

9. Berg I a, Kockelkorn D, Ramos-Vera WH, Say RF, Zarzycki J, Hügler M, Alber BE, Fuchs G: **Autotrophic carbon fixation in archaea.**. *Nat. Rev. Microbiol.* 2010, **8**:447–60.

10. Overmann J, Garcia-Pichel F: *The prokaryotes: A handbook on the biology of bacteria*. 2006.

11. Stephanopoulos G: **Metabolic fluxes and metabolic engineering.** *Metab. Eng.* 1999, **1**:1–11.

12. Yuan J, Bennett BD, Rabinowitz JD: **Kinetic flux profiling for quantitation of cellular metabolic fluxes.** *Nat. Protoc.* 2008, **3**:1328–40.

13. Wiechert W: **13C Metabolic Flux Analysis**. *Metab. Eng.* 2001, **3**:195–206.

14. Sauer U: **Metabolic networks in motion: 13C-based flux analysis**. *Mol Syst Biol* 2006, **2**:62.

15. Young JD, Allen DK, Morgan JA: **Isotopomer Measurement Techniques in Metabolic Flux Analysis II: Mass Spectrometry**. In *Plant Metabolism: Methods and Protocols, Methods in Molecular Biology*. . 2014:85–108.

16. Jazmin LJ, Young JD: **Isotopically nonstationary 13C metabolic flux analysis**. *Methods Mol. Biol.* 2013, **985**:367–390.

17. Nöh K, Wahl A, Wiechert W: **Computational tools for isotopically instationary 13C labeling experiments under metabolic steady state conditions.** *Metab. Eng.* 2006, **8**:554–77.

18. Wiechert W, Nöh K: **From Stationary to Instationary Metabolic Flux Analysis**. In *Advances in Biochemical Engineering/ Biotechnology*. . 2005:145–172.

19. Toya Y, Shimizu H: **Flux analysis and metabolomics for systematic metabolic engineering of microorganisms.** *Biotechnol. Adv.* 2013, **31**:818–26.

20. Young JD, Walther JL, Antoniewicz MR, Yoo H: **An Elementary Metabolite Unit (EMU) Based Method of Isotopically Nonstationary Flux Analysis**. *Biotechnology* 2008, **99**:686–699.

21. Antoniewicz MR, Kelleher JK, Stephanopoulos G: **Elementary metabolite units (EMU): a novel framework for modeling isotopic distributions.** *Metab. Eng.* 2007, **9**:68–86.

22. Schwarz D, Orf I, Kopka J, Hagemann M: **Recent Applications of Metabolomics Toward Cyanobacteria** . *Metabolites* 2013, **3**:72–100.

23. Jazmin LJ, O'Grady JP, Ma F, Allen DK, Morgan JA, Young JD: **Isotopically nonstationary MFA (INST-MFA) of autotrophic metabolism**. *Methods Mol. Biol.* 2014, **1090**:181–210.

24. Young JD: **INCA : A computational platform for isotopically nonstationary metabolic flux analysis**. *Bioinformatics* 2014, **30**:1333–35.

25. Zamboni N, Fendt S-M, Rühl M, Sauer U: **(13)C-based metabolic flux analysis.** *Nat. Protoc.* 2009, **4**:878–92.

26. Schmidt K, Carlsen M, Nielsen J, Villadsen J: **Modeling isotopomer distributions in biochemical networks using isotopomer mapping matrices.** *Biotechnol. Bioeng.* 1997, **55**:831–40.

27. Wiechert W, Siefke C, de Graaf a a, Marx a: **Bidirectional reaction steps in metabolic networks: II. Flux estimation and statistical analysis.** *Biotechnol. Bioeng.* 1997, **55**:118–35.

28. Foster L V.: **Rank and null space calculations using matrix decomposition without column interchanges** *Linear Algebra Appl.* 1986, **74**:47–71.

29. Dulmage AL, Mendelsohn NS: **Coverings of bipartite graphs**. *Canad J Math* 1958, **10**:517–534.

30. Pothen A, Fan CJ: **Computing the block triangular form of a sparse matrix**. *T Math Soft* 1990, **16**:303–324.

31. Noh K, Wiechert W: **Experimental Design Principles for Isotopically Instationary C Labeling Experiments**. *Biotech* 2005, **94**:234–51.

32. Gill PE, Murray W, M.H. W: *Practical Optimization*. Academic Press; 1981.

33. Madsen K, Nielsen HB, Tigleff O: **Methods for non-linear least squares problems**. 2004.

34. Antoniewicz MR, Kelleher JK, Stephanopoulos G: **Determination of confidence intervals of metabolic fluxes estimated from stable isotope measurements.** *Metab. Eng.* 2006, **8**:324–37.

35. Conover WJ: *Practical Nonparameteric Statistics*. Wiley; 1999.

36. Rohn H, Hartmann A, Junker A, Junker BH, Schreiber F: **FluxMap: a VANTED Add-on for the visual exploration of flux distributions in biological networks**. *BMC Syst. Biol.* 2012, **6**:33.

37. König M, Holzhütter H-G: **Fluxviz - cytoscape plug-in for visualization of flux distributions in networks.** *Genome Inform.* 2010, **24**:96–103.

38. Hoppe A, Hoffmann S, Gerasch A, Gille C, Holzhütter H-G: **FASIMU: flexible software for flux-balance computation series in large metabolic networks.** *BMC Bioinformatics* 2011, **12**:28.

39. Droste P, Miebach S, Niedenführ S, Wiechert W, Nöh K: **Visualizing multi-omics data in metabolic networks with the software Omix: a case study.** *Biosystems.* 2011, **105**:154–61.

40. Paley SM, Karp PD: **The Pathway Tools cellular overview diagram and Omics Viewer.** *Nucleic Acids Res.* 2006, **34**:3771–8.

41. Matthews L, Gopinath G, Gillespie M, Caudy M, Croft D, de Bono B, Garapati P, Hemish J, Hermjakob H, Jassal B, et al.: **Reactome knowledgebase of human biological pathways and processes.** *Nucleic Acids Res.* 2009, **37**:D619–22.

42. Kono N, Arakawa K, Ogawa R, Kido N, Oshita K, Ikegami K, Tamaki S, Tomita M: **Pathway projector: web-based zoomable pathway browser using KEGG atlas and Google Maps API.** *PLoS One* 2009, **4**:e7710.

43. Lee SY, Lee D-Y, Hong SH, Kim TY, Yun H, Oh Y-G, Park S: **MetaFluxNet, a program package for metabolic pathway construction and analysis, and its use in large-scale metabolic flux analysis of Escherichia coli.** *Genome Inform.* 2003, **14**:23–33.

44. Rocha I, Maia P, Evangelista P, Vilaça P, Soares S, Pinto JP, Nielsen J, Patil KR, Ferreira EC, Rocha M: **OptFlux: an open-source software platform for in silico metabolic engineering.** *BMC Syst. Biol.* 2010, **4**:45.

45. King Z a., Dräger A, Ebrahim A, Sonnenschein N, Lewis NE, Palsson BO: **Escher: A Web Application for Building, Sharing, and Embedding Data-Rich Visualizations of Biological Pathways**. *PLOS Comput. Biol.* 2015, **11**.

46. Schaub J, Mauch K, Reuss M: **Metabolic flux analysis in Escherichia coli by integrating isotopic dynamic and isotopic stationary 13C labeling data.**. *Biotechnol. Bioeng.* 2008, **99**:1170–85.

47. Sauer U: **High-throughput phenomics: experimental methods for mapping fluxomes.** *Curr. Opin. Biotechnol.* 2004, **15**:58–63.

48. Keasling JD: **Manufacturing Molecules Through Metabolic Engineering**. *Science (80).* 2010, **330**:1355–1358.

49. McAtee AG, Jazmin LJ, Young JD: **Application of isotope labeling experiments and 13C flux analysis to enable rational pathway engineering**. *Curr. Opin. Biotechnol.* 2015, **36**:50–56.

50. Oliver JWK, Atsumi S: **Metabolic design for cyanobacterial chemical synthesis.**. *Photosynth. Res.* 2014, **120**:249–61.

51. Adebiyi AO, Jazmin LJ, Young JD: **(13)C flux analysis of cyanobacterial metabolism.** *Photosynth. Res.* 2014.

52. Berla BM, Saha R, Immethun CM, Maranas CD, Moon TS, Pakrasi HB: **Synthetic biology of cyanobacteria: unique challenges and opportunities** . *Front. Microbiol.* 2013, **4**:1–14.

53. Yang C, Hua Q, Shimizu K: **Integration of the information from gene expression and metabolic fluxes for the analysis of the regulatory mechanisms in Synechocystis.** *Appl. Microbiol. Biotechnol.* 2002, **58**:813–22.

54. Yang C, Hua Q, Shimizu K: **Metabolic Flux Analysis in Synechocystis Using Isotope Distribution from 13C-Labeled Glucose**. *Metab. Eng.* 2002, **4**:202–216.

55. Yang C, Hua Q, Shimizu K: **Quantitative analysis of intracellular metabolic fluxes using GC-MS and two-dimensional NMR spectroscopy.** . *J. Biosci. Bioeng.* 2002, **93**:78–87.

56. Nakajima T, Kajihata S, Yoshikawa K, Matsuda F, Furusawa C, Hirasawa T, Shimizu H: **Integrated Metabolic Flux and Omics Analysis of Synechocystis sp. PCC 6803 under Mixotrophic and Photoheterotrophic Conditions.** *Plant Cell Physiol.* 2014, **55**:1605–1612.

57. You L, Berla B, He L, Pakrasi HB, Tang YJ: **13C-MFA delineates the photomixotrophic metabolism of Synechocystis sp. PCC 6803 under light- and carbon-sufficient conditions.** *Biotechnol. J.* 2014, **9**:684–92.

58. Zhang S, Bryant D a: **The tricarboxylic acid cycle in cyanobacteria.** *Science* 2011, **334**:1551–3.

59. Feng X, Bandyopadhyay A, Berla B, Page L, Wu B, Pakrasi HB, Tang YJ: **Mixotrophic and photoheterotrophic metabolism in Cyanothece sp. ATCC 51142 under continuous light.** *Microbiology* 2010, **156**:2566–74.

60. Alagesan S, Gaudana SB, Sinha A, Wangikar PP: **Metabolic flux analysis of Cyanothece sp. ATCC 51142 under mixotrophic conditions**. *Photosynth. Res.* 2013, **118**:191–198.

61. Huege J, Goetze J, Schwarz D, Bauwe H, Hagemann M, Kopka J: **Modulation of the major paths of carbon in photorespiratory mutants of synechocystis.** *PLoS One* 2011, **6**:e16278.

62. Badger MR, Price GD: **CO2 concentrating mechanisms in cyanobacteria: Molecular components, their diversity and evolution**. *J. Exp. Bot.* 2003, **54**:609–622.

63. DellaPenna D: **Plant metabolic engineering.** *Plant Physiol.* 2001, **125**:160–163.

64. Libourel IGL, Shachar-Hill Y: **Metabolic flux analysis in plants: from intelligent design to rational engineering.** *Annu. Rev. Plant Biol.* 2008, **59**:625–50.

65. Dieuaide-Noubhani M, Raffard G, Canioni P, Pradet a, Raymond P: **Quantification of compartmented metabolic fluxes in maize root tips using isotope distribution from 13C- or 14C-labeled glucose.**. *J. Biol. Chem.* 1995, **270**:13147–59.

66. Glucose C, Raymond P, Rolin D, Alonso AP, Dieuaide-noubhani M, Segalen V: **A New Substrate Cycle in Plants . Evidence for a High Glucose-Phosphate-to-Glucose Turnover from in Vivo Steady-State and Pulse-Labeling Experiments with**. *Society* 2005, **138**:2220–2232.

67. Alonso AP, Raymond P, Rolin D, Dieuaide-Noubhani M: **Substrate cycles in the central metabolism of maize root tips under hypoxia**. *Phytochemistry* 2007, **68**:2222–2231.

68. Alonso AP, Raymond P, Hernould M, Rondeau-Mouro C, de Graaf A, Chourey P, Lahaye M, Shachar-Hill Y, Rolin D, Dieuaide-Noubhani M: **A metabolic flux analysis to study the role of sucrose synthase in the regulation of the carbon partitioning in central metabolism in maize root tips.** *Metab. Eng.* 2007, **9**:419–32.

69. Rontein D, Dieuaide-Noubhani M, Dufourc EJ, Raymond P, Rolin D: **The metabolic architecture of plant cells. Stability of central metabolism and flexibility of anabolic pathways during the growth cycle of tomato cells.** *J. Biol. Chem.* 2002, **277**:43948–60.

70. Schwender J, Ohlrogge JB: **Probing in Vivo Metabolism by Stable Isotope Labeling of Storage Lipids and Proteins in Developing Brassica napus Embryos1**. *Plant Physiol.* 2002, **130**:347–361.

71. Schwender J, Ohlrogge JB, Shachar-Hill Y: **A flux model of glycolysis and the oxidative pentosephosphate pathway in developing Brassica napus embryos.** *J. Biol. Chem.* 2003, **278**:29442–53.

72. Goffman F, Ohlrogge JB: **Rubisco without the Calvin cycle improves the carbon efficiency of developing green seeds**. *Nature* 2004, **432**:779–782.

73. Schwender J, Shachar-Hill Y, Ohlrogge JB: **Mitochondrial metabolism in developing embryos of Brassica napus.** *J. Biol. Chem.* 2006, **281**:34040–7.

74. Junker BH, Lonien J, Heady LE, Rogers A, Schwender J: **Parallel determination of enzyme activities and in vivo fluxes in Brassica napus embryos grown on organic or inorganic nitrogen source.** *Phytochemistry* 2007, **68**:2232–42.

75. Allen DK, Goldford J, Gierse JK, Mandy D, Diepenbrock C, Libourel IGL: **Quantification of peptide m / z distributions from 13C-labeled cultures with high-resolution mass spectrometry**. *Anal. Chem.* 2014, **86**:1894–1901.

76. Allen DK, Shachar-Hill Y, Ohlrogge JB: **Compartment-specific labeling information in 13C metabolic flux analysis of plants.** *Phytochemistry* 2007, **68**:2197–210.

77. Allen DK, Young JD: **Carbon and nitrogen provisions alter the metabolic flux in developing soybean embryos.** *Plant Physiol.* 2013, **161**:1458–75.

78. Sriram G, Fulton DB, Iyer V V, Peterson JM, Zhou R, Westgate ME, Spalding MH, Shanks J V: **Quantification of Compartmented Metabolic Fluxes in Developing Soybean Embryos by Employing Biosynthetically Directed Fractional 13 C Labeling , Two-Dimensional [13 C , 1 H] Nuclear Magnetic Resonance , and Comprehensive Isotopomer Balancing 1 [w]**. *Society* 2004, **136**:3043–3057.

79. Alonso AP, Goffman FD, Ohlrogge JB, Shachar-Hill Y: **Carbon conversion efficiency and central metabolic fluxes in developing sunflower (Helianthus annuus L.) embryos.** *Plant J.* 2007, **52**:296–308.

80. Ettenhuber C, Spielbauer G, Margl L, Hannah LC, Gierl A, Bacher A, Genschel U, Eisenreich W: **Changes in flux pattern of the central carbohydrate metabolism during kernel development in maize**. *Phytochemistry* 2005, **66**:2632–2642.

81. Spielbauer G, Margl L, Hannah LC, Römisch W, Ettenhuber C, Bacher A, Gierl A, Eisenreich W, Genschel U: **Robustness of central carbohydrate metabolism in developing maize kernels.** *Phytochemistry* 2006, **67**:1460–75.

82. Sriram G, Fulton DB, Shanks J V.: **Flux quantification in central carbon metabolism of Catharanthus roseus hairy roots by 13C labeling and comprehensive bondomer balancing**. *Phytochemistry* 2007, **68**:2243–2257.

83. Masakapalli SK, Ritala A, Dong L, Van Der Krol AR, Oksman-Caldentey KM, Ratcliffe RG, Sweetlove LJ: **Metabolic flux phenotype of tobacco hairy roots engineered for increased geraniol production**. *Phytochemistry* 2014, **99**:73–85.

84. Ratcliffe RG, Shachar-Hill Y: **Measuring multiple fluxes through plant metabolic networks.** *Plant J.* 2006, **45**:490–511.

85. Fernie a R, Morgan J a: **Analysis of metabolic flux using dynamic labeling and metabolic modeling.** *Plant. Cell Environ.* 2013.

86. Szecowka M, Heise R, Tohge T, Nunes-Nesi A, Vosloh D, Huege J, Feil R, Lunn J, Nikoloski Z, Stitt M, et al.: **Metabolic fluxes in an illuminated Arabidopsis rosette.** *Plant Cell* 2013, **25**:694–714.

87. Sweetlove LJ, Obata T, Fernie AR: **Systems analysis of metabolic phenotypes: what have we learnt?** *Trends Plant Sci.* 2013.

88. Heise R, Arrivault S, Szecowka M, Tohge T, Nunes-Nesi A, Stitt M, Nikoloski Z, Fernie AR: **Flux profiling of photosynthetic carbon metabolism in intact plants.** *Nat. Protoc.* 2014, **9**:1803–24.

89. Hays SG, Ducat DC: **Engineering cyanobacteria as photosynthetic feedstock factories**. *Photosynth. Res.* 2014.

90. Camsund D, Lindblad P: **Engineered Transcriptional Systems for Cyanobacterial Biotechnology** *Front. Bioeng. Biotechnol.* 2014, **2**:1–9.

91. Markley AL, Begemann MB, Clarke RE, Gordon GC, Pfleger BF: **A synthetic biology toolbox for controlling gene expression in the cyanobacterium Synechococcus strain sp. PCC 7002**. 2015.

92. Varman a. M, Xiao Y, Pakrasi HB, Tang YJ: **Metabolic engineering of Synechocystis 6803 for isobutanol production** *Appl. Environ. Microbiol.* 2012.

93. Wang W, Liu X, Lu X: **Engineering cyanobacteria to improve photosynthetic production of alka(e)nes** *Biotechnol. Biofuels* 2013, **6**:69.

94. Atsumi S, Higashide W, Liao JC: **Direct photosynthetic recycling of carbon dioxide to isobutyraldehyde** *Nat. Biotechnol.* 2009, **27**:1177–80.

95. Peralta-Yahya PP, Zhang F, del Cardayre SB, Keasling JD: **Microbial engineering for the production of advanced biofuels**. *Nature* 2012, **488**:320–328.

96. Bustos SA, Golden SS: **Expression of the psbDII gene in Synechococcus sp. strain PCC 7942 requires sequences downstream of the transcription start site**. *J. Bacteriol.* 1991, **173**:7525–7533.

97. Murphy T a, Young JD: **ETA: Robust software for determination of cell specific rates from extracellular time courses.** . *Biotechnol. Bioeng.* 2013, **xxx**:1–11.

98. Folch J, Lees M, Stanley GH.: **A simple method for the isolation and purification of total lipides from animal tissues**. *J. Biol. Chem.* 1957, **226**:497–509.

99. Antoniewicz MR, Kelleher JK, Stephanopoulos G: **Accurate assessment of amino acid mass isotopomer distributions for metabolic flux analysis.** *Anal. Chem.* 2007, **79**:7554–9.

100. Kaplan A, Reinhold L: **Concentrating mechanisms in photosynthetic microorganisms**. *Annu. Rev. Plant Physiol. Plant Mol. Biol.* 1999, **50**:539–570.

101. Knowles VL, Smith CS, Smith CR, Plaxton WC: **Structural and Regulatory Properties of Pyruvate Kinase from the Cyanobacterium Synechococcus PCC 6301**. *J. Biol. Chem.* 2001, **276**:20966–20972.

102. Bricker TM, Zhang S, Laborde SM, Mayer PR, Frankel LK, Moroney J V.: **The malic enzyme is required for optimal photoautotrophic growth of Synechocystis sp. strain PCC 6803 under continuous light but not under a diurnal light regimen**. *J. Bacteriol.* 2004, **186**:8144–8148.

103. Shuvalov VA, Vasmel H, Amesz J, Duysens LNM: **Picosecond spectroscopy of the charge separation in reaction centers of Chloroflexus aurantiacus with selective excitation of the primary electron donor**. *Biochim. Biophys. Acta - Bioenerg.* 1986, **851**:361–368.

104. Adebiyi AO: **Metabolic engineering of cyanobacteria for increased product formation**. 2015, **126:**19-32..

105. Schwarz D, Nodop A, Hüge J, Purfürst S, Forchhammer K, Michel K-P, Bauwe H, Kopka J, Hagemann M: **Metabolic and transcriptomic phenotyping of inorganic carbon acclimation in the Cyanobacterium Synechococcus elongatus PCC 7942.** . *Plant Physiol.* 2011, **155**:1640–55.

106. Raines CA: **Increasing photosynthetic carbon assimilation in C3 plants to improve crop yield: current and future strategies.** *Plant Physiol.* 2011, **155**:36–42.

107. Eberhard S, Finazzi G, Wollman F-A: **The dynamics of photosynthesis.** *Annu. Rev. Genet.* 2008, **42**:463–515.

108. Paul MJ, Foyer CH: **Sink regulation of photosynthesis.** *J. Exp. Bot.* 2001, **52**:1383–1400.

109. Jänkänpää HJ, Mishra Y, Schröder WP, Jansson S: **Metabolic profiling reveals metabolic shifts in Arabidopsis plants grown under different light conditions.** *Plant. Cell Environ.* 2012, **35**:1824–36.

110. Griffin KL, Seemann JR: **Plants, CO2 and photosynthesis in the 21st century.** *Chem. Biol.* 1996, **3**:245–254.

111. Sage RF: **Variation in the k(cat) of Rubisco in C(3) and C(4) plants and some implications for photosynthetic performance at high and low temperature.** *J. Exp. Bot.* 2002, **53**:609–620.

112. Häusler RE, Hirsch H-J, Kreuzaler F, Peterhänsel C: **Overexpression of C(4)-cycle enzymes in transgenic C(3) plants: a biotechnological approach to improve C(3)-photosynthesis.** *J. Exp. Bot.* 2002, **53**:591–607.

113. Maurino VG, Peterhansel C: **Photorespiration: Current status and approaches for metabolic engineering**. *Curr. Opin. Plant Biol.* 2010, **13**:249–256.

114. Parry MAJ, Andralojc PJ, Scales JC, Salvucci ME, Carmo-Silva AE, Alonso H, Whitney SM: **Rubisco activity and regulation as targets for crop improvement**. *J. Exp. Bot.* 2013, **64**:717–730.

115. Miyagawa Y, Tamoi M, Shigeoka S: **Overexpression of a cyanobacterial fructose-1,6-/sedoheptulose-1,7-bisphosphatase in tobacco enhances photosynthesis and growth.** *Nat. Biotechnol.* 2001, **19**:965–969.

116. Henkes S, Sonnewald U, Badur R, Flachmann R, Stitt M: **A small decrease of plastid transketolase activity in antisense tobacco transformants has dramatic effects on photosynthesis and phenylpropanoid metabolism.** *Plant Cell* 2001, **13**:535–551.

117. Peterhanse C, Blume C, Offermann S: **Photorespiratory bypasses: How can they work?** *J. Exp. Bot.* 2013, **64**:709–715.

118. Zhu X-G, de Sturler E, Long SP: **Optimizing the distribution of resources between enzymes of carbon metabolism can dramatically increase photosynthetic rate: a numerical simulation using an evolutionary algorithm.** *Plant Physiol.* 2007, **145**:513–26.

119. Boyle NR, Morgan JA: **Flux balance analysis of primary metabolism in Chlamydomonas reinhardtii.** *BMC Syst. Biol.* 2009, **3**:4.

120. Poolman MG, Kundu S, Shaw R, Fell D: **Responses to Light Intensity in a Genome-Scale Model of Rice Metabolism.** *Plant Physiol.* 2013, **162**:1060–1072.

121. Grafahrend-Belau E, Junker A, Eschenroder A, Muller J, Schreiber F, Junker BH: **Multiscale metabolic modeling: dynamic flux balance analysis on a whole plant scale**. *Plant Physiol.* 2013, **163**:637–47.

122. Borisjuk L, Neuberger T, Schwender J, Heinzel N, Sunderhaus S, Fuchs J, Hay JO, Tschiersch H, Braun H-P, Denolf P, et al.: **Seed architecture shapes embryo metabolism in oilseed rape.** *Plant Cell* 2013, **25**:1625–40.

123. Lonien J, Schwender J: **Analysis of metabolic flux phenotypes for two Arabidopsis mutants with severe impairment in seed storage lipid synthesis.** *Plant Physiol.* 2009, **151**:1617–34.

124. Allen DK, Young JD: **Carbon and nitrogen provisions alter the metabolic flux in developing soybean embryos.** . *Plant Physiol.* 2013, **161**:1458–75.

125. Alonso AP, Val DL, Shachar-Hill Y: **Central metabolic fluxes in the endosperm of developing maize seeds and their implications for metabolic engineering**. *Metab. Eng.* 2011, **13**:96–107.

126. Mandy DE, Goldford JE, Yang H, Allen DK, Libourel IGL: **Metabolic flux analysis using ^{13}C peptide label measurements.** . *Plant J.* 2014, **77**:476–86.

127. Masakapalli SK, Kruger NJ, Ratcliffe RG: **The metabolic flux phenotype of heterotrophic Arabidopsis cells reveals a complex response to changes in nitrogen supply**. *Plant J.* 2013.

128. Arrivault S, Guenther M, Ivakov A, Feil R, Vosloh D, van Dongen JT, Sulpice R, Stitt M: **Use of reverse-phase liquid chromatography, linked to tandem mass spectrometry, to profile the Calvin cycle and other metabolic intermediates in Arabidopsis rosettes at different carbon dioxide concentrations.** *Plant J.* 2009, **59**:826–39.

129. Hasunuma T, Harada K, Miyazawa S-II, Kondo A, Fukusaki E, Miyake C: **Metabolic turnover analysis by a combination of in vivo 13C-labelling from 13CO2 and metabolic profiling with CE-MS/MS reveals rate-limiting steps of the C3 photosynthetic pathway in Nicotiana tabacum leaves.** *J. Exp. Bot.* 2010, **61**:1041–51.

130. Szecowka M, Heise R, Tohge T, Nunes-nesi A, Vosloh D, Huege J, Feil R, Lunn J, Nikoloski Z, Stitt M, et al.: **Metabolic fluxes in an illuminated Arabidopsis rosette**. *Plant Cell* 2013, **25**:694–714.

131. Kelleher JK, Masterson TM: **Model equations for condensation biosynthesis using stable isotopes and radioisotopes.** *Am. J. Physiol.* 1992, **262**:E118–E125.

132. Antoniewicz MR, Kraynie DF, Laffend LA, González-lergier J, Kelleher JK, Stephanopoulos G: **Metabolic flux analysis in a nonstationary system: Fed-batch fermentation of a high yielding strain of E. coli producing 1,3-propanediol**. *Metab. Eng.* 2007, **9**:277–292.

133. Stessman D, Miller A, Spalding M, Rodermel S: **Regulation of photosynthesis during Arabidopsis leaf development in continuous light.** *Photosynth. Res.* 2002, **72**:27–37.

134. Zeeman SC, Smith SM, Smith AM: **The diurnal metabolism of leaf starch.** *Biochem. J.* 2007, **401**:13–28.

135. Stitt M, Lunn J, Usadel B: **Arabidopsis and primary photosynthetic metabolism - more than the icing on the cake.** *Plant J.* 2010, **61**:1067–91.

136. Tcherkez G, Mahé A, Gauthier P, Mauve C, Gout E, Bligny R, Cornic G, Hodges M: **In folio respiratory fluxomics revealed by 13C isotopic labeling and H/D isotope effects highlight the noncyclic nature of the tricarboxylic acid "cycle" in illuminated leaves.** *Plant Physiol.* 2009, **151**:620–630.

137. Ainsworth EA, Bush DR: **Carbohydrate export from the leaf: a highly regulated process and target to enhance photosynthesis and productivity.** *Plant Physiol.* 2011, **155**:64–69.

138. Amiard V, Mueh KE, Demmig-Adams B, Ebbert V, Turgeon R, Adams WW: **Anatomical and photosynthetic acclimation to the light environment in species with differing mechanisms of phloem loading.** *Proc. Natl. Acad. Sci. U. S. A.* 2005, **102**:12968–12973.

139. Allen DK, Laclair RW, Ohlrogge JB, Shachar-Hill Y: **Isotope labelling of Rubisco subunits provides in vivo information on subcellular biosynthesis and exchange of amino acids between compartments.** *Plant. Cell Environ.* 2012, **35**:1232–44.

140. Huege J, Sulpice R, Gibon Y, Lisec J, Koehl K, Kopka J: **GC-EI-TOF-MS analysis of in vivo carbon-partitioning into soluble metabolite pools of higher plants by monitoring isotope dilution after 13CO2 labelling.** *Phytochemistry* 2007, **68**:2258–72.

141. Sharkey TD: **Estimating the Rate of Photorespiration in Leaves**. *Physiol. Plant.* 1988, **73**:146–152.

142. Busch FA: **Current methods for estimating the rate of photorespiration in leaves**. *Plant Biol.* 2013, **15**:648–655.

143. Timm S, Nunes-Nesi A, Pärnik T, Morgenthal K, Wienkoop S, Keerberg O, Weckwerth W, Kleczkowski LA, Fernie AR, Bauwe H: **A cytosolic pathway for the conversion of hydroxypyruvate to glycerate during photorespiration in Arabidopsis.** *Plant Cell* 2008, **20**:2848–2859.

144. Collakova E, Goyer A, Naponelli V, Krassovskaya I, Gregory JF, Hanson AD, Shachar-Hill Y: **Arabidopsis 10-formyl tetrahydrofolate deformylases are essential for photorespiration.** *Plant Cell* 2008, **20**:1818–1832.

145. Cegelski L, Schaefer J: **NMR determination of photorespiration in intact leaves using in vivo 13CO2 labeling**. *J. Magn. Reson.* 2006, **178**:1–10.

146. Pärnik T, Ivanova H, Keerberg O: **Photorespiratory and respiratory decarboxylations in leaves of C 3 plants under different CO2 concentrations and irradiances**. *Plant, Cell Environ.* 2007, **30**:1535–1544.

147. Evans JR: **Leaf anatomy enables more equal access to light and CO2 between chloroplasts**. *New Phytol.* 1999, **143**:93–104.

148. Terashima I, Hanba YT, Tholen D, Niinemets Ü: **Leaf functional anatomy in relation to photosynthesis.** *Plant Physiol.* 2011, **155**:108–116.

149. Hanba YT, Kogami H, Terashima I: **The effect of growth irradiance on leaf anatomy and photosynthesis in Acer species differing in light demand**. *Plant, Cell Environ.* 2002, **25**:1021–1030.

150. Foyer CH, Bloom AJ, Queval G, Noctor G: **Photorespiratory metabolism: genes, mutants, energetics, and redox signaling.** *Annu. Rev. Plant Biol.* 2009, **60**:455–484.

151. Kruger NJ, Ratcliffe RG: **Insights into plant metabolic networks from steady-state metabolic flux analysis.** *Biochimie* 2009, **91**:697–702.

152. Fell DA: **Enzymes, metabolites and fluxes**. *J. Exp. Bot.* 2005, **56**:267–272.

153. Athanasiou K, Dyson BC, Webster RE, Johnson GN: **Dynamic acclimation of photosynthesis increases plant fitness in changing environments.** . *Plant Physiol.* 2010, **152**:366–73.

154. Deeken R, Ache P, Kajahn I, Klinkenberg J, Bringmann G, Hedrich R: **Identification of Arabidopsis thaliana phloem RNAs provides a search criterion for phloem-based transcripts hidden in complex datasets of microarray experiments**. *Plant J.* 2008, **55**:746–759.

155. Wilkinson TL, Douglas AE: **Phloem amino acids and the host plant range of the polyphagous aphid, Aphis fabae**. *Entomol. Exp. Appl.* 2003, **106**:103–113.

156. Caputo C, Barneix AJ: **The Relationship between Sugar and Amino Acid Export to the Phloem in Young**. *Ann. Bot.* 1999, **84**:33–38.

157. Adams WW, Watson AM, Mueh KE, Amiard V, Turgeon R, Ebbert V, Logan BA, Combs AF, Demmig-Adams B: **Photosynthetic acclimation in the context of structural constraints to carbon export from leaves**. *Photosynth. Res.* 2007, **94**:455–466.

158. Timm S, Florian A, Arrivault S, Stitt M, Fernie AR, Bauwe H: **Glycine decarboxylase controls photosynthesis and plant growth**. *FEBS Lett.* 2012, **586**:3692–3697.

159. Laber LJ, Latzko E, Gibbs M: **Photosynthetic path of carbon dioxide in spinach and corn leaves**. *J. Biol. Chem.* 1974, **249**:3436–3441.

160. Bassham J a, Kirk M, Jensen RG: **Photosynthesis by isolated chloroplasts. I. Diffusion of labeled photosynthetic intermediates between isolated chloroplasts and suspending medium.** *Biochim. Biophys. Acta* 1968, **153**:211–218.

161. Heber U: **Energy coupling in chloroplasts**. *J. Bioenerg. Biomembr.* 1976, **8**:157–172.

162. Hitz WD, Stewart CR: **Oxygen and Carbon Dioxide Effects on the Pool Size of Some Photosynthetic and Photorespiratory Intermediates in Soybean (Glycine max [L.] Merr.).** *Plant Physiol.* 1980, **65**:442–446.

163. Taylor SE, Terry N: **Limiting Factors in Photosynthesis: V. Photochemical Energy Supply Colimits Photosynthesis at Low Values of Intercellular CO(2) Concentration.** *Plant Physiol.* 1984, **75**:82–86.

164. Eckardt NA, Snyder GW, Portis AR, Orgen WL: **Growth and photosynthesis under high and low irradiance of Arabidopsis thaliana antisense mutants with reduced ribulose-1,5-bisphosphate carboxylase/oxygenase activase content.** *Plant Physiol.* 1997, **113**:575–586.

165. Schleucher J, Vanderveer P, Markley JL, Sharkey TD: **Intramolecular deuterium distributions reveal disequilibrium of chloroplast phosphoglucose isomerase**. *Plant, Cell Environ.* 1999, **22**:525–533.

166. Dietz KJ: **A possible rate-limiting function of chloroplast hexosemonophosphate isomerase in starch synthesis of leaves**. *Biochim. Biophys. Acta* 1985, **839**:240–248.

167. Boyes DC, Zayed AM, Ascenzi R, McCaskill AJ, Hoffman NE, Davis KR, Görlach J: **Growth stage-based phenotypic analysis of Arabidopsis: a model for high throughput functional genomics in plants.** *Plant Cell* 2001, **13**:1499–1510.

168. Pracharoenwattana I, Zhou W, Keech O, Francisco PB, Udomchalothorn T, Tschoep H, Stitt M, Gibon Y, Smith SM: **Arabidopsis has a cytosolic fumarase required for the massive allocation of photosynthate into fumaric acid and for rapid plant growth on high nitrogen.** . *Plant J.* 2010, **62**:785–95.

169. Araujo WL, Tohge T, Osorio S, Lohse M, Balbo I, Krahnert I, Sienkiewicz-Porzucek A, Usadel B, Nunes-Nesi A, Fernie AR: **Antisense Inhibition of the 2-Oxoglutarate Dehydrogenase Complex in Tomato Demonstrates Its Importance for Plant Respiration and during Leaf Senescence and Fruit Maturation**. *Plant Cell* 2012, **24**:2328–2351.

170. Spreitzer RJ, Salvucci ME: **Rubisco: structure, regulatory interactions, and possibilities for a better enzyme.** . *Annu. Rev. Plant Biol.* 2002, **53**:449–75.

171. Bauwe H, Hagemann M, Fernie AR: **Photorespiration: players, partners and origin**. *Trends Plant Sci.* 2010, **15**:330–336.

172. McGrath JM, Long SP: **Can the cyanobacterial carbon-concentrating mechanism increase photosynthesis in crop species? A theoretical analysis.** . *Plant Physiol.* 2014, **164**:2247–61.

173. Price GD, Pengelly JJL, Forster B, Du J, Whitney SM, Von Caemmerer S, Badger MR, Howitt SM, Evans JR: **The cyanobacterial CCM as a source of genes for improving photosynthetic CO2 fixation in crop species**. *J. Exp. Bot.* 2013, **64**:753–768.

174. Raven JA: **Inorganic carbon acquisition by eukaryotic algae: four current questions.** *Photosynth. Res.* 2010, **106**:123–134.

175. Muhaidat R, Sage RF, Dengler NG: **Diversity of Kranz anatomy and biochemistry in C4 eudicots**. *Am. J. Bot.* 2007, **94**:362–381.

176. Christin PA, Besnard G, Samaritani E, Duvall MR, Hodkinson TR, Savolainen V, Salamin N: **Oligocene CO2 Decline Promoted C4 Photosynthesis in Grasses**. *Curr. Biol.* 2008, **18**:37–43.

177. Sage TL, Sage RF: **The functional anatomy of rice leaves: Implications for refixation of photorespiratory CO2 and efforts to engineer C4 photosynthesis into rice**. *Plant Cell Physiol.* 2009, **50**:756–772.

178. Zhu XG, Shan L, Wang Y, Quick WP: **C4 Rice - an Ideal Arena for Systems Biology Research**. *J. Integr. Plant Biol.* 2010, **52**:762–770.

179. Furbank RT, Von Caemmerer S, Sheehy J, Edwards G: **C4 rice: A challenge for plant phenomics**. *Funct. Plant Biol.* 2009, **36**:845–856.

180. Weber APM, von Caemmerer S: **Plastid transport and metabolism of C3 and C4 plants-comparative analysis and possible biotechnological exploitation**. *Curr. Opin. Plant Biol.* 2010, **13**:257–265.

181. Lin MT, Occhialini A, Andralojc PJ, Parry M a J, Hanson MR: **A faster Rubisco with potential to increase photosynthesis in crops** . *Nature* 2014, **513**:547–550.

182. Giordano M, Beardall J, Raven J a: **CO2 concentrating mechanisms in algae: mechanisms, environmental modulation, and evolution.** . *Annu. Rev. Plant Biol.* 2005, **56**:99–131.

183. Ma F, Jazmin LJ, Young JD, Allen DK: **Isotopically nonstationary 13 C flux analysis of changes in Arabidopsis thaliana leaf metabolism due to high light acclimation**. *Proc. Natl. Acad. Sci.* 2014, **111**:16967–16972.

184. Long SP, Ainsworth EA, Rogers A, Ort DR: **Rising atmospheric carbon dioxide: plants FACE the future.** *Annu. Rev. Plant Biol.* 2004, **55**:591–628.

185. Leakey ADB, Xu F, Gillespie KM, McGrath JM, Ainsworth EA, Ort DR: **Genomic basis for stimulated respiration by plants growing under elevated carbon dioxide.** *Proc. Natl. Acad. Sci. U. S. A.* 2009, **106**:3597–3602.

186. Florian A, Timm S, Nikoloski Z, Tohge T, Bauwe H, Araújo WL, Fernie AR: **Analysis of metabolic alterations in Arabidopsis following changes in the carbon dioxide and oxygen partial pressures.** . *J. Integr. Plant Biol.* 2014.

187. Galmés J, Aranjuelo I, Medrano H, Flexas J: **Variation in Rubisco content and activity under variable climatic factors**. *Photosynth. Res.* 2013, **117**:73–90.

188. Tuncel A, Okita TW: **Improving starch yield in cereals by over-expression of ADPglucose pyrophosphorylase: Expectations and unanticipated outcomes**. *Plant Sci.* 2013, **211**:52–60.

189. Geigenberger P, Tiessen A, Meurer J: **Use of Non-aqueous Fractionationa and Metabolomics to Study Chloroplast Function in Arabidopsis** . 2011, **775**.

190. Jazmin LJ, Grady JPO, Ma F, Allen DK, Morgan JA, Young JD, O'Grady JP, Ma F, Allen DK, Morgan JA, et al.: **Isotopically Nonstationary MFA (INST-MFA) of Autotrophic Metabolism**. *Methods Mol. Biol.* 2014, **1090**:181–210.

191. Peterhansel C, Horst I, Niessen M, Blume C, Kebeish R, Kürkcüoglu S, Kreuzaler F: **Photorespiration**. In *The Arabidopsis Book*. . 2010:1–24.

192. Wiechert W, Wurzel M: **Metabolic isotopomer labeling systems part I: Global dynamic behavior**. *Math. Biosci.* 2001, **169**:173–205.

193. Amaral AI, Teixeira AP, Håkonsen BI, Sonnewald U, Alves PM: **A comprehensive metabolic profile of cultured astrocytes using isotopic transient metabolic flux analysis and 13C-labeled glucose**. *Front. Neuroenergetics* 2011, **3**:1–17.

194. Nöh K, Grönke K, Luo B, Takors R, Oldiges M, Wiechert W: **Metabolic flux analysis at ultra short time scale: isotopically non-stationary 13C labeling experiments.** . *J. Biotechnol.* 2007, **129**:249–67.

195. Maier K, Hofmann U, Reuss M, Mauch K: **Identification of metabolic fluxes in hepatic cells from transient 13C-labeling experiments: Part II. Flux estimation.** . *Biotechnol. Bioeng.* 2008, **100**:355–70.

196. Ahn WS, Antoniewicz MR: **Metabolic flux analysis of CHO cells at growth and non-growth phases using isotopic tracers and mass spectrometry.** . *Metab. Eng.* 2011, **13**:598–609.

197. Murphy TA, Dang C V., Young JD: **Isotopically nonstationary 13C flux analysis of Myc-induced metabolic reporgramming in B-cells**. *Metab. Eng.* 2013, **15**:206–217.

198. Zhao Z, ten Pierick A, de Jonge L, Heijnen JJ, Wahl SA: **Substrate cycles in Penicillium chrysogenum quantified by isotopic non-stationary flux analysis**. *Microb. Cell Fact.* 2012, **11**:140.

199. Jordà J, Suarez C, Carnicer M, ten Pierick A, Heijnen JJ, van Gulik W, Ferrer P, Albiol J, Wahl A: **Glucose-methanol co-utilization in Pichia pastoris studied by metabolomics and instationary ^{13}C flux analysis.** *BMC Syst. Biol.* 2013, **7**:17.

APPENDIX OF DETAILED PROTOCOLS

BG11 Media Recipe for cyanobacteria growth

A. Introduction

This protocol describes the BG11 recipe used for culturing cyanobacteria.

B. Required Materials

	Stock	Add to 1L Medium
1) $NaNO_3$	150 g/L	10 mL
2) $K_2HPO_4•3H_2O$	40 g/L	1 mL
3) $MgSO_4•7H_2O$	75 g/L	1 mL
4) $CaCl_2•2H_2O$	36 g/L	1 mL
5) $FeNH_4$•Citrate	12 g/L	1 mL
6) Na_2EDTA (pH8.0)	1 g/L	1 mL
7) Na_2CO_3	20 g/L	1 mL
8) A_5 (see below)	---	1 mL

H_3BO_3	2.86 g/L
$MnCl_2•4H_2O$	1.81 g/L
$ZnSO_4•7H_2O$	0.222 g/L
$Na_2MoO_4•2H_2O$	0.391 g/L
$CuSO_4•5H_2O$	0.079 g/L
$Co(NO_3)_2•6H_2O$	0.0494 g/L

9a) Bacto Agar (for Agar only)		15 g/L
9) NaS_2O_3 (for Agar only)	1M	1mL
10) Antibiotics		

Antibiotic	Stock (mg/mL)	Final Concentration (μg/mL)	Added from Stock (mL/L BG11)
Km	50	10	0.2
Spec	40	40	1
Cb	10	5	0.05

C. Protocol

Liquid BG11 Media

1. For liquid BG11 media, add steps B.1-8 in a 2L flask with 983mL DI H2O and autoclave on liquid cycle. Allow to cool before proceeding and add the appropriate amount of antibiotics as necessary.
2. For modified BG11 media with an added 50mM NaHCO3, remove 50 mL of media from 1L of BG11. In a separate beaker, add 4.2g of NaHCO3 and mix with a stir bar until fully dissolved. Filter sterilize the NaHCO3 solution back into the meida.

BG11 agar plates

3. For BG11 agar plates, add steps B.1-9a in a 2L flask with 983 DI H2O and autoclave on liquid cycle. Allow to cool before proceeding.
4. Once cool to touch, add stepB10 and the appropriate amount of antibiotics.
5. Pour approximately 25mL to each sterile petri dish. Allow agar to solidify in the hood with open or cracked lids to prevent condensation on top of the lid. When cool, place lid back onto the plate and store in a cold room.

Cyanobacterial optical cell density assay

A. Introduction

This protocol describes how the optical density each culture is measured.

B. Required Materials and Equipment

- BG11 media
- 96-well clear bottom plate
- μQuant Spectrophotometer

C. Protocol

1. Remove 350uL of culture and mix with 350uL of BG11 media in a microcentrifuge tube.
2. Pipette out 200 uL of the diluted culture into 3 wells for technical replicates.
3. Measure absorbance (OD) at 750nm and 730nm using the plate reader.
4. Calculate cell density using the following equation:
   Cell density (mg/mL) =0.684 * (OD750 – 0.045); The value of 0.045 is used as a blank BG11 media value for correction.
5. Cell growth may be calculated by correlating the optical cell density measured at given time points during the exponential growth phase.

Cyanobacterial aldehyde production assay

A. Introduction

This protocol describes how aldehyde production is quantified in a closed system cyanobacterial culture.

B. Protocol

1. Grow enough culture to reseed 3- 125mL erlenmeyer flasks with 75mL of modified BG11 media (with 50mM $NaHCO_3$ added) and appropriate amount of antibiotics to achieve a final starting OD750 of 0.4.
2. Set the water bath to 30°C and shaking speed of 120 rpm. Bubble flasks with air.
3. Give all the cell cultures a dark pulse for 12 hours (t=-12) to synchronize circadian rhythm by wrapping the flasks with aluminum foil and then placing back in the water bath.
4. At t=0, remove the foil from the flasks and add 75uL of IPTG (1M stock concentration) to each flask to induce aldehyde production and turn the lights on to 150 uE.
5. At t=6, stop bubbling and remove 1.5mL for growth and aldehyde quantification. Add a rubber stopper to each flask. Store samples in fridge until ready for processing.
6. At t=30, chill cultures in flask in fridge for 10-15 minutes to condense all aldehyde in the headspace back into the liquid culture. Remove 1.5mL for growth and aldehyde quantification. Store samples in fridge until ready for processing.
7. For all samples taken for aldehyde quantification, spin down 1mL of culture in a microcentrifuge tube. Transfer the supernatant to a new microcentrigue tube and discard cell pellet.
8. To 450 uL of supernatant, add 5uL of 100 mM n-butyraldehyde (internal standard; final concentration 1mM nBA).
9. Transfer 200 uL into a 2mL GC amber vial fitted with a 250 uL polypropylene insert to run on the GC-FID.
10. Run samples on GC-FID using a calibration curve with known amounts of isobutyraldehyde and isovaleraldehyde for quantification.

GC-FID method for quantifying aldehyde production

A. Introduction

This protocol describes the parameters necessary for GC-FID analysis. It is best to inject sample as quickly as possible on GC-FID after aldehyde sample preparation.

B. GC-FID method parameters

Instrument: Shimadzu GC-2010
Column: DB-Wax (30m x 0.2 mm i.d. x 0.2um film thickness; Agilent J&W Scientific)
Injector temperature: 210°C
Detector temperature: 250°C
Injection volume: 0.5 uL
Carrier gas: Helium

Oven gradient:

	Rate (°C/min)	Temp (°C)	Hold time (min)	Run time (min)
Initial		30	8	8
Ramp	30	220	8	22.33

Cyanobacterial isotopically nonstationary 13C labeling experiment

A. Introduction

This protocol is used for the 13C labeling experiment of cyanobacterial cells in liquid culture.

B. Protocol

1. In a 1L flask, start with 500 mL of culture and modified BG11 media (with 50mM NaHCO3) at OD750=0.4 and appropriate amount of antibiotics.
2. Set the water bath to 30°C and shaking speed of 120 rpm. Bubble flask with air.
3. Give the flask a dark pulse for 12 hours (t=-12) to synchronize circadian rhythm by wrapping with aluminum foil and then placing back in the water bath.
4. At t=0, remove the foil from the flask and add 500uL of IPTG (1M stock concentration) to each flask to induce aldehyde production and turn the lights on to 150 uE.
5. At t=30, initiate labeling by adding 50mL of 13C Sodium Bicarbonate solution (Cambridge Isotope Laboratories, 97% isotopic purity) to achieve a final tracer concentration of 100mM in the culture.
6. At each time point, remove 20mL of cell culture using a syringe and luer-lock needle (12 gauge, 12", Sigma-Aldrich) and immediately add to 30mL of quench solution (0C PBS).
7. Pellet out cell by centrifugation (chillded to -5C or coler). Spin at 4000rpm fro 15 min.
8. Remove supernatant; collect supernatant sample for further analysis (to ensure intracellular metabolites have not leaked out).
9. Flash freeze cell pellet in liquid N2 and store in -80C freezer until ready for metabolite extraction.

Time points: t= 0, 30, 60, 120, 180, 300, 600, and 900 sec.

Metabolite extraction/ sample preparation

A. Introduction

This protocol describes the extraction of intracellular metabolites for subsequent derivatization and GC-MS analysis. Received starting sample should be cell pellet.

B. Required Materials and Equipment

- Pre-cooled chloroform (-20°C)
- Pre-cooled methanol (-20°C)
- Ice-cold water
- 10 mM Norvaline (internal standard)
- 15 mL falcon tube
- Refrigerated centrifuge

C. Extraction Protocol

1. Resuspend cells in 4 mL chloroform (-20°C)
2. Add 2 mL methanol (-20°C)
3. Add internal standard (6uL of Norvaline at 10mM)
4. Vortex tubes for 30 minutes in cold room or with ice stays
5. Add 1.5 mL iced-cold water
6. Vortex tubes for additional 5 minutes
7. Transfer to 15 mL centrifuge tube
8. Centrifuge at 5,000 rpm for 20 min at lowest temperature setting
9. Collect aqueous (upper) phase in a new 15 mL tube or two Eppendorf tubes (label the tubes)
10. Evaporate all extracts to dryness using aeration at room temperature. Store samples at -80°C

Modified MOX-TMS derivatization of metabolite extracts

A. Introduction

This protocol describes the derivatization of intracellular metabolites for subsequent GC/MS analysis.

B. Required Materials and Equipment

- MOX reagent (Pierce Biotechnology, product# 45950)
- TMS: BSTFA + 10% TMCS, 1 mL ampules (Pierce Biotechnology, product# 38840)
- 2 mL amber glass injection vial
- 150 uL insert for injection vial
- Evaporator (Pierce Reacti-Vap)
- Sonicator
- Heating block

C. MOX derivatization protocol

1. Dissolve dried sample in 50 uL MOX reagent
2. Place in sonication bath for 30 min at room temperature
3. Incubate for 90 min. at 40°C on a heating block

D. TMS derivatization protocol

4. Add 70 uL of BSTFA +10 % TMCS
5. Incubate for 30 min at 40°C on a heating block
6. Remove from heating block and incubate overnight at room temperature

E. Preparation for GC/MS

7. Centrifuge for 5 min at 14,000 rpm to remove solid debris
8. Transfer liquid to injection vial containing a 150 uL microvolume insert

GC-MS Method for analyzing TMS (or TBDMS) derivatized metabolites

A. Introduction

This protocol describes the parameters necessary for GC-MS analysis. It is best to inject sample as quickly as possible on GC-MS after derivatization.

B. GC-MS method parameters

GC parameters:
Instrument: Agilent 7890A
Column: DB-35MS (30m x 0.25 mm i.d. x 0.25mm; Agilent J&W Scientific)
Injection: 1 µL (splitless)
Inlet temperature: 270°C
He Flow: 1 mL/min
Purge Flow: 50 mL/min, activated 2 min after injection

MS parameters:
Instrument: Agilent 5975C inert XL EI/CI MSD with Triple-Axis Detector
Scan*:* 50-800 m/z
Use auto tune parameters for ionization voltages

Oven gradient:

	Rate (°C/min)	Temp (°C)	Hold time (min)	Run time (min)
Initial		80	5	5
Ramp	10	320	5	34